RECENT TRENDS IN ADJOINT SENSITIVITY ANALYSIS FOR TRANSMISSION-LINE MODELLING METHOD

RECENT TRENDS IN ADJOINT SENSITIVITY ANALYSIS FOR TRANSMISSION-LINE MODELLING METHOD

By

PAYAM ABOLGHASEM, B. A. Sc., B. Sc.

A Thesis

Submitted to the School of Graduate Studies in Partial Fulfillment

of the Requirement for the Degree Master of Applied Science

McMaster University

MASTER OF APPLIED SCIENCE (2006) McMaster University
(Electrical and Computer Engineering) Hamilton, Ontario

TITLE: **RECENT TRENDS IN ADJOINT SENSITIVITY ANALYSIS FOR TRANSMISSION-LINE MODELLING METHOD**

AUTHOR: PAYAM ABOLGHASEM
B. A. Sc. (Electrical Engineering), University of Ottawa
B. Sc. (Applied Physics), Azad University of Tehran

SUPERVISOR: Dr. Mohamed H. Bakr, Assistant Professor
Department of Electrical and Computer Engineering
B. Sc. (Cairo University)
M. A. Sc. (Cairo University)
Ph. D. (McMaster University)
P. Eng. (Ontario)

NUMBER OF PAGES: 102

ABASTRACT

This thesis addresses recent trends and developments of the adjoint-variable method (AVM) for microwave structures with the time-domain transmission-line modeling (TD-TLM) method.

Design sensitivity analysis of high-frequency (HF) structures is concerned with estimating the sensitivity of the response with respect to the design parameters. This information is essential at different stages of the design cycle such as the optimization, tolerance analysis, and yield analysis.

Traditional approaches of sensitivity calculations involve estimating the sensitivities thought finite-difference approximations. They suffer from formidable simulation time, as the full-wave analysis of practical HF structure requires extensive computational time. For a structure with N design parameters, at least N+1 system analyses are required to extract the design response and its sensitivities. The adjoint variable method, on the other hand, supplies the sensitivity information in a very efficient way. Using at most two system analysis, the algorithm provides the design responses and its sensitivities, regardless of the number of the design parameters.

In this thesis two contributions have been achieved which aims at enhancing the efficiency of the TLM-AVM framework. The first contribution is a reformulation of the AVM. This reformulation results in casting both the original and the adjoint systems in mathematically identical forms. It is shown that both systems can thus be modeled using a single TLM simulator with the only difference in the excitation. The second contribution focuses on generalizing the AVM algorithm by employing it for more advanced TLM nodes. The compatibility of the symmetrical condensed node (SCN) with the AVM algorithm has been verified in previous work for a general 3-D problem. Here, this is extended to include the hybrid symmetrical condensed node (HSCN), which is more efficient in terms of memory saving and simulation time. The new approaches are all illustrated through sensitivity estimation of different waveguide structures.

ACKNOWLEDMENTS

Among all who have contributed to my education at McMaster University, my greatest appreciation surely belongs to my supervisor, Dr. Mohamed H. Bakr who supported me through the Master program. It has been a pleasant journey learning from and working with him. His unwavering commitment to each of his students is appreciated more than he knows. I also wish to thank Dr. Natalia Nikolova and Dr. John W. Bandler for their supports as well as fostering the friendly atmosphere within the Computational Electromagnetic Group.

I would like to thank my colleagues Peter A. W. Basl and Mohamed Swillam for participating in discussions and for their helpful comments in different stages in my work.

This research would not have been possible without the financial support of the Department of the Electrical and Computer Engineering. I would like to thank for the generous teacher assistantship, research assistantship and the scholarship.

My acknowledgment will not be complete without mentioning the staff members of the ECE Department for their dedication and for their assistance during the past two years. My special thanks go to Cheryl Gies, Terry Greenlay, and Cosmin Coroiu.

Finally, I would like to express my deepest gratitude to my parents, my brother, and my wife for their unconditional love and emotional supports which has been the greatest motivation. Specially, I thank my mother, Fleur and my dear brother Pedram who were my first teachers and their encouragement inspired my passion for learning, as well as my wife Mahsa for her unfailing support and her boundless love.

CONTENTS

LIST OF FIGURES

Chapter 1

INTORDUCTION

1.1 Motivation

Sensitivity analysis of electromagnetic (EM) structures concerns with evaluating the sensitivities of the design response to the variations of the design parameters. This is essential in a wide range of EM problems including gradient-based optimization, tolerance analysis, as well as yield analysis. In an optimization problem, the design response is usually expressed as a real-valued scalar objective function (cost function) which denotes the global performance of the system. In other cases, network parameters such as the S-parameters may be considered as the system response. Typically, the design parameters describe the physical dimensions of the problem and the medium's properties characterized by the constitutive parameters.

Traditional approaches for estimating the design sensitivities mostly suffer from the extensive simulation time. Examples are the finite-difference approximations based on the forward/backward finite differences as well the more accurate approach of the central finite differences. For a problem with N design parameters, the formers require N additional system analyses for estimating the sensitivities, while $2N$ extra simulations are required in the later case. In practice, for problems with large N, it becomes apparent that the imposed plentiful simulation time makes them infeasible. Smarter techniques are; therefore, inevitable.

The adjoint variable method (AVM) offers a robust and efficient framework for estimating the design sensitivities. This is achieved by introducing an auxiliary system, referred to as the adjoint system. Regardless of the number of design parameters, the algorithm extracts the design response and its sensitivities using, at most two analyses of the original and the adjoint problems. AVM has a long history in other disciplines such as structural design [1], circuit theory [2]-[10], and control theory. Nevertheless, it has received small attention in analysis of the full-wave electromagnetic problems. The first appearance of the algorithm in this area was limited to the numerical techniques using the finite-element method [11]-[16]. It was then extended to other techniques such as the method of moments (MoM) [17]-[20], the finite-difference time-domain (FDTD) method [21]-[24], and the transmission-line modeling (TLM) method [25],[26].

This thesis specifically focuses on the recent enhancements of the AVM algorithm for the time-domain TLM. Since the initial proposal of the TLM-AVM framework, the algorithm has been well developed in different manners. In [27], the algorithm is extended to include problems with dispersive absorbing boundaries. Further development included the sensitivity estimations of the objective function with respect to dielectric discontinuities [28]. A novel technique has been recently proposed to cast the sensitivity estimations of the S-parameters within the time-domain framework [29]. In all these problems, the equations expressing the original and the adjoint systems have distinct mathematical form, which impedes the integration of the simulation of the two systems into a unique TLM simulator. In this work a novel approach has been illustrated which casts the mathematical form of the original and the adjoint simulation into an identical form with is implemented using a single engine [30].

Further improvement of the TLM-AVM framework has been achieved by illustrating the algorithm for more efficient 3-D TLM discretization elements. So far, the symmetrical condensed node (SCN) is utilized to show the AVM algorithm [31]. Although SCN is regarded as the most popular 3-D discretization node, in the standard form, it is not efficient in terms of dispersion properties, simulation time step and memory storage. The hybrid symmetrical condensed node (HSCN) is a good substitution which tackles the undesirable features of the standard SCN. The second major contribution of this thesis is devoted to illustrate the compatibility of the HSCN with the adjoint variable method.

1.2 Overview of the Thesis

The thesis can be divided into two major sections. The first section (chapters 1-3) provides comprehensive reviews of the methods and algorithms which have been employed throughout this work. The second section (chapters 4 and 5) contains the major contributions to the subject. To illustrate specific points, results are presented in each chapter, separately.

Chapter 2 reviews the underlying theory of the transmission-line modeling method. Both 2-D and 3-D techniques are discussed. The shunt scheme in 2-D and the symmetrical condensed node (SCN), as the most popular 3-D TLM node, are described in details. Mesh parameters, excitation for a particular field configuration, mesh output, and the scattering and connection properties are all presented. A short discussion is also devoted to handling different kinds of boundary conditions in TLM including single reflection and wide band absorbing boundaries and the wideband absorbing boundaries.

Chapter 3 is concerned with the theory of the adjoint-variable method for time-domain TLM. Main issues regarding the practical implementation of the algorithm is described, by emphasizing on the appropriate impulses storage on the original and the adjoint simulation for metallic and dielectric discontinuities. As a recent novel technique, the sensitivity analysis of complex-values S-parameters within time domain framework is discussed. The approach is illustrated though real-values objective functions as well as *S*-parameter sensitivities with respect to physical dimensions of waveguide discontinuities.

Chapter 4 proposes a novel formulation to improve the adjoint algorithm by reversing the time reference of the adjoint simulation. This results to expressing both the original and the adjoint simulations in an identical mathematical form, where the two simulations differ only in the excitation. A unique TLM engine is then utilized to run both analyses.

Chapter 5 describes the employment of the hybrid symmetrical condensed node (HSCN) within the AVM framework for the first time. A thorough discussion about the underlying theory of the HSCN is provided, where its advantages over the standard SCN are emphasized.

Finally, our achievements and results are concluded and summarized in Chapter 6, where possible directions for future researches are suggested.

REFERENCES

[1] E. J. Haug, K. K. Choi, and V. Komkov, *Design Sensitivity Analysis of Structural Systems*. Orlando, FL: Academic, 1986.

[2] S. W. Director and R. A. Rohrer, "The generalized adjoint network and network sensitivities," *IEEE Trans. Circuit Theory*, vol. CT-16, pp. 318–323, Aug. 1969.

[3] S. W. Director and R. A. Rohrer, "Automated network design-The frequency-domain case," *IEEE Trans. Circuit Theory*, vol. CT-16, pp. 330–337, Aug. 1969.

[4] B. D. H. Tellegen, "A general network theorem, with applications," *Philips Res. Rep.*, vol. 7, pp. 259–269, 1959.

[5] P. Penfield, Jr., R. Spence, and S. Duinker, "A generalized form of Tellegen's theorem," *IEEE Trans. Circuit Theory*, vol. CT-17, pp. 302–305, Aug. 1970.

[6] J. W. Bandler and R. E. Seviora, "Current trends in network optimization," *IEEE Trans. Microwave Theory Tech.*, vol. MTT-18, pp. 1159–1170, Dec. 1970.

[7] J.W. Bandler and R. E. Seviora, "Wave sensitivities of networks," *IEEE Trans. Microwave Theory Tech.*, vol. MTT-20, pp. 138–147, Feb. 1972.

[8] V. A. Monaco and P. Tiberio, "Computer-aided analysis of microwave circuits," *IEEE Trans. Microwave Theory Tech.*, vol. MTT-22, pp. 249–263, Mar. 1974.

[9] K. C. Gupta, R. Garg, and R. Chadha, *Computer-Aided Design of Microwave Circuits*. Dedham, MA: Artech House, 1981.

[10] J. W. Bandler and S. H. Chen, "Circuit optimization: The state of the art," *IEEE Trans. Microwave Theory Tech.*, vol. 36, pp. 424–442, Feb. 1988.

[11] P. Garcia and J. P. Webb, "Optimization of planar devices by the finite element method," *IEEE Trans. Microwave Theory Tech.*, vol. 38, pp. 48–53, Jan. 1990.

[12] H. Akel and J. P. Webb, "Design sensitivities for scattering-matrix calculation with tetrahedral edge elements," *IEEE Trans. Magn.*, vol. 36, pp. 1043–1046, July 2000.

[13] J. P. Webb, "Design sensitivities using high-order tetrahedral vector elements," *IEEE Trans. Magn.*, vol. 37, pp. 3600–3603, Sept. 2001.

[14] J. P. Webb, "Design sensitivity of frequency response in 3-D finite-element analysis of microwave devices," *IEEE Trans. Magn.*, vol. 38, pp. 1109–1112, Mar. 2002.

[15] M. M. Gavrilovic and J. P. Webb, "Accuracy control in the optimization of microwave devices by finite-element methods," *IEEE Trans. Microwave Theory Tech.*, vol. 50, pp. 1901–1911, Aug. 2002.

[16] Y. S. Chung, C. Cheon, I. H. Park, and S. Y. Hahn, "Optimal design method for microwave device using time domain method and design sensitivity analysis Part I: FETD case," *IEEE Trans. Magn.*, vol. 37, pp. 3289–3293, Sept. 2001.

[17] H. Lee and T. Itoh, "A systematic optimum design of waveguide-to-microstrip transition," *IEEE Trans. Microwave Theory Tech.*, vol. 45, pp. 803–809, May 1997.

[18] S. Amari, "Numerical cost of gradient computation within the method of moments and its reduction by means of a novel boundary-layer concept,"in *IEEE MTT-S Int. Microwave Symp. Dig.*, vol. 3, 2001, pp. 1945–1948.

[19] N. K. Georgieva, S. Glavic, M. H. Bakr, and J. W. Bandler, "Feasible adjoint sensitivity technique for EM design optimization," *IEEE Trans. Microwave Theory Tech.*, vol. 50, pp. 2751–2758, Dec. 2002.

[20] A. S. Soliman, M. H. Bakr, and N. K. Nikolova, "An adjoint variable method for sensitivity calculations of multiport devices," *IEEE Trans. Microwave Theory Tech.*, vol. 52, no. 2, pp. 589–599, Feb. 2004.

[21] Y.-S. Chung, C. Cheon, I. Park, and S. Hahn, "Optimal shape design of microwave device using FDTD and design sensitivity analysis," *IEEE Trans. Microwave Theory Tech.*, vol. 48, pp. 2289–2296, Dec. 2000.

[22] Y. S. Chung, C. Cheon, I. H. Park, and S. Y. Hahn, "Optimal design method for microwave device using time domain method and design sensitivity analysis-Part II: FDTD case," *IEEE Trans. Magn.*, vol. 37, pp. 3255–3259, Sept. 2001.

[23] G. Shen, H. W. W. Tam, N. K. Nikolova, and M. H. Bakr, "Adjoint sensitivity technique for FDTD methods on structured grids," in *Proc. IEEE/URSI Int. Antennas Propagation Symp.*, Columbus, OH, pp. 746–749, June 2003.

[24] Y. S. Rickard, N. K. Georgieva, and H. W. Tam, "Absorbing boundary conditions for adjoint problems in the design sensitivity analysis with the FDTD method," *IEEE Trans. Microwave Theory Tech.*, vol. 51, pp. 526–529, Feb. 2003.

[25] M. H. Bakr and N. K. Nikolova, "An adjoint variable method for frequency domain TLM problems with conducting boundaries," *IEEE Microwave Wireless Comp. Lett.*, vol. 13, pp. 408–410, Sept. 2003.

[26] M. H. Bakr and N. K. Nikolova, "An adjoint variable method for time domain TLM with fixed structured grids," in *IEEE MTT-S Int. Microwave Symp. Dig.*, vol. 2, Philadelphia, PA, pp. 1121–1124, June 2003.

[27] M.H. Bakr and N.K. Nikolova, "An adjoint variable method for time domain TLM with wideband Johns matrix boundaries," *IEEE Trans. Microwave Theory Tech.*, vol. 52, pp. 678-685, Feb. 2004.

[28] P.A.W. Basl, M.H. Bakr and N.K. Nikolova, "Efficient estimation of sensitivities in TLM with dielectric discontinuities," *Microwave and Wireless Components Letters*, vol 15, No. 2, pp. 89-91, Feb. 2005.

[29] M.H. Bakr and N.K. Nikolova, "Efficient Estimation of Adjoint-Variable *S*-Parameter Sensitivities with Time Domain TLM," *Int. J. of Numerical Modeling: Electronic Networks, Devices and Fields,* vol. 18, pp. 171-187, Mar. 2005.

[30] P. Abolghasem, M.H. Bakr, W. J. R. Hoefer, and P. M. So, "A transformed TLM formulation for adjoint-variable based sensitivity analysis," *Microwave and Wireless Components Letters*, vol. 15, No. 11, pp. 817-819, Nov. 2005.

[31] P.A.W. Basl, M.H. Bakr and N.K. Nikolova, "An AVM technique for 3-D TLM with symmetric condensed nodes," *Microwave and Wireless Components Letters*, vol 15, no. 10, pp. 618-620, Oct. 2005,.

[32] P.B. Johns, "A symmetrical condensed node for the TLM method," *IEEE Trans. Microwaves Theory Tech.*, vol. 35, no. 4, pp. 370-377, April 1987.

[33] C. Christopoulos, *The Transmission-Line Modeling Method TLM.* IEEE PRESS. 1995.

[34] W. J. Hoefer, "The discrete time domain green's function or Johns' matrix- a new powerful concept in transmission line modeling (TLM)," *Int. Journal of Numerical Modeling: Electronic Networks, Devices and Fields,* vol. 2, Dec.1989, pp. 215-225.

[35] E. G. Costache and W. J. Hoefer, " TLM modeling of dispersive wide-band absorbing boundaries with time domain diakoptics for S-parameter extraction," *IEEE Trans. Microwave Theory Tech.,* vol. 38, no. 4, April 1990, pp. 379- 385.

[36] R. A. Scaramuzza and A.J. Lowery, "Hybrid symmetrical condensed node for TLM method," *Electronics Lett.*, vol. 26, no. 23, Nov. 1990, pp. 1947-1949.

[37] P. Berini and K. Wu, "A pair of hybrid symmetrical condensed node," *IEEE Microwave and guided wave letters*, vol. 4, no. 7, July 1994, pp. 244-246.

Chapter 2

TRANSMISSION-LINE MODELLING (TLM) METHOD

This chapter reviews the time-domain transmission-line modeling (TD-TLM) method used for modelling two and three dimensional electromagnetic problems involving linear and isotropic materials.

2.1 Basic Formulation

The transmission-line modelling method is a powerful technique for solving electromagnetic field problems with the most general type. Initially proposed by P.B. Johns [1], the method was based on the realization of the Huygens's principle of wave propagation in a discretized space-time framework.

In TLM, the computational domain is discretized into a network of transmission-lines, referred to as "link-lines". The intersections of the link-lines then form the TLM nodes. In this work, 2-D shunt node [1] and the stub-loaded symmetrical condensed node [2] are used as the discretization elements in two and three dimensional problems, respectively. The structure of the nodes and the characteristic impedances of the link-lines are selected such that the voltages and currents on the link-lines provide the electric and magnetic field information at the node location. In fact, TLM inherits the advantage that at a certain simulation time all electromagnetic field components are collocated. This is in contrast with other approaches such as the finite-difference approximations where averaging techniques over space and time are required to obtain all the field components at one position. The TLM simulation is carried out by the consecutive execution of four major steps:

- Scattering the incident impulses
- Connecting the reflected impulses
- Applying boundary conditions
- Exciting the structure

Initially, the desired excitation is introduced into the simulation by injecting incident impulse voltages to designated link-lines of certain nodes. The excited voltages are partly reflected and partly transmitted at the nodes. These scattered impulses then form the incident impulses on the neighboring nodes in the next time step, where they get scattered and so on. The appropriate boundary conditions are applied if a link-line has an interface with an external boundary.

Assume the computational domain is discretized into N nodes. We denote the total number of associated link-lines by N_L. A single TLM simulation with non-dispersive boundary at the k^{th} time step is then expressed by

$$
{}_{k+1}\boldsymbol{V} = \boldsymbol{C}\boldsymbol{S}\,{}_{k}\boldsymbol{V} + {}_{k}\boldsymbol{V}^{s} \quad , \quad \boldsymbol{V}(0) = \boldsymbol{0} \tag{2.1}
$$

where

${}_{k}\boldsymbol{V} \in \mathbb{R}^{N_L \times 1}$ is the vector of incident impulses of all nodes at the k^{th} time step,

$\boldsymbol{S} \in \mathbb{R}^{N_L \times N_L}$ is the block diagonal system scattering matrix whose m^{th} block is the nodal scattering matrix of the m^{th} node,

$\boldsymbol{C} \in \mathbb{R}^{N_L \times N_L}$ is the system connection matrix specifying how the reflected impulses are connected to the neighboring nodes, and

${}_k\boldsymbol{V}^s$ is the excitation vector.

The initial condition, $\boldsymbol{V}(0) = \boldsymbol{0}$ ensures that at the beginning of the simulation the incident impulses on all link-lines are set to zero. In (2.1), the application of boundary conditions resides in the connection step. Later in this chapter a more general expression will be presented to deal with dispersive absorbing boundaries modeled by Johns' matrix [7,8].

2.2 Two Dimensional TLM Nodes

A major group of electromagnetic problems can be solved by two-dimensional models. Examples include propagation of TE and TM waves within waveguides. For a given problem an initial 2-D simulation, which is more efficient in simulation time and storage, usually provides considerable information. A full 3-D analysis may be required at the final stage.

Figure 2.1 shows the discretization of a section of the computational domain in 2-D TLM where the network of the transmission-lines forms a uniform Cartesian mesh. Regardless of node structure, the figure illustrates the propagation of unit impulse excitations at the end of the first and second iterations. Two common node topologies for analysis of 2-D problems are the "series" and the "shunt" configurations. The first suits modeling of TE wave propagation, while the second admits TM waves. The 2-D shunt

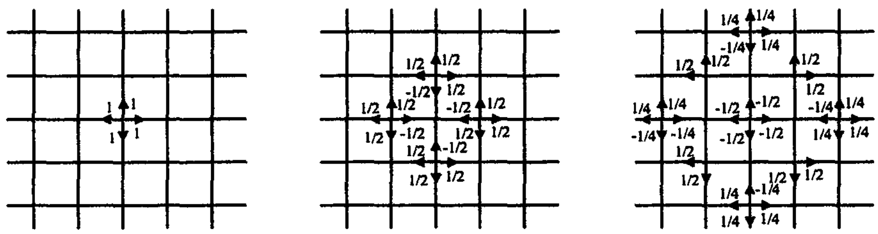

(a) (b) (c)

Figure 2.1: Schematic of 2D TLM mesh with uniform Cartesian link-lines: (a) unit impulse excitation, (b) scattered impulses at the first iteration, and (c) scattered impulses at the second iteration.

node has received more attention in the literature. This is mainly because the shunt scheme deals more easily with problems where the medium non-homogeneities are due to the relative permittivity. As in most problems, the permeability of the medium is constant, equal to that of the free space $\mu = \mu_0$, shunt scheme is used more widely. Hybrid schemes are also available for 2-D TLM problems. Such a technique is reported in [9], where the utilized node can model mediums where both ε_r and μ_r vary.

2.2.1 The Shunt TLM Node

In order to model the propagation of electromagnetic fields using transmission-lines a mapping between the parameters in the two models is required. Such a mapping for the shunt scheme can be obtained by applying both Kirchhoff's laws for circuit analysis and Maxwell's equations. The topology of the 2-D shunt node, and its equivalent lumped element network, used for modelling a lossless and homogenous medium is illustrated in Figure 2.2. The characteristic impedances of all link-lines are considered to be identical. This is done in order to avoid extra reflections at the interface of the adjacent nodes. Using Kirchhoff's voltage and current laws, we have

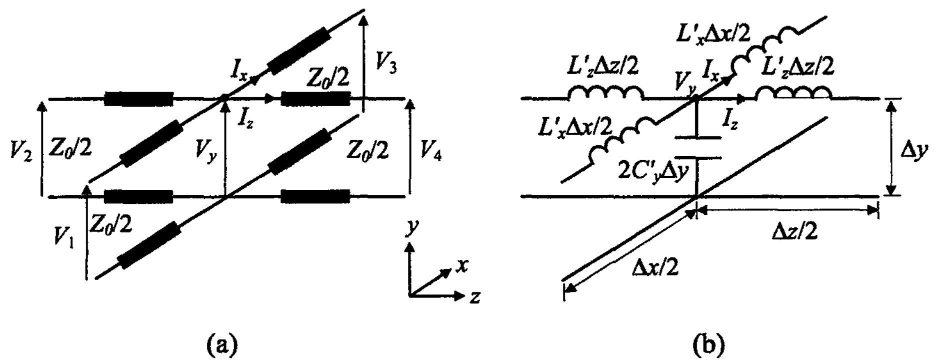

Figure 2.2: 2-D shunt node structure. (a) Transmission-line model where the characteristic impedances of the intersecting TLs are identical and equal to Z_0. (b) Lumped-element model where L'_ξ ($\xi = x, z$) is the inductance per unit length along the ξ-direction, and C'_y is the capacitance per unit length along the y-direction.

$$\frac{\partial V_y}{\partial x} = -L'_x \frac{\partial I_x}{\partial t} \tag{2.2}$$

$$\frac{\partial V_y}{\partial z} = -L'_z \frac{\partial I_z}{\partial t} \tag{2.3}$$

$$-\Delta x \frac{\partial I_x}{\partial x} - \Delta z \frac{\partial I_z}{\partial z} = 2C'_y \Delta y \frac{\partial V_y}{\partial t}. \tag{2.4}$$

Differentiating (2.2), (2.3) and (2.4) with respect to x, z and t, respectively, and combining them together, we get

$$\frac{\Delta x}{L'_x}\frac{\partial^2 V_y}{\partial x^2} + \frac{\Delta z}{L'_z}\frac{\partial^2 V_y}{\partial z^2} = 2C'_y \Delta y \frac{\partial^2 V_y}{\partial t^2}. \tag{2.5}$$

The mappings between the lumped-element values and the medium properties are thus given by [5]

$$L'_x = \mu_m \frac{\Delta y}{\Delta z} \quad , \quad L'_z = \mu_m \frac{\Delta y}{\Delta x} \quad , \quad C'_y = \varepsilon_m \frac{\Delta x \Delta z}{2(\Delta y)^2}, \tag{2.6}$$

where ε_m and μ_m are the medium permittivity and permeability, respectively. Inserting (2.6) in (2.5) gives

$$\frac{\partial^2}{\partial x^2}\left(\frac{V_y}{\Delta y}\right)+\frac{\partial^2}{\partial z^2}\left(\frac{V_y}{\Delta y}\right)=2\varepsilon_m\mu_m\frac{\partial^2}{\partial t^2}\left(\frac{V_y}{\Delta y}\right). \tag{2.7}$$

For TM$_y$ waves where the non-zero field components are E_y, H_x and H_z, Maxwell's equations are:

$$\begin{aligned}
\frac{\partial E_y}{\partial x} &= -\mu_m \frac{\partial H_z}{\partial t} \\
\frac{\partial E_y}{\partial z} &= \mu_m \frac{\partial H_x}{\partial t} \\
\frac{\partial H_x}{\partial z}-\frac{\partial H_z}{\partial x} &= \varepsilon_m \frac{\partial E_y}{\partial t}.
\end{aligned} \tag{2.8}$$

Accordingly, the wave equation of the E_y component, propagating in the xz-plane is

$$\frac{\partial^2 E_y}{\partial x^2}+\frac{\partial^2 E_y}{\partial z^2}=\mu_m\varepsilon_m\frac{\partial^2 E_y}{\partial t^2}. \tag{2.9}$$

Comparison between equations (2.2)-(2.9) suggests the following mappings between the parameters in the two models

$$\begin{aligned}
E_y &\leftrightarrow -\frac{V_y}{\Delta y} \\
H_x &\leftrightarrow -\frac{I_z}{\Delta x} \\
H_z &\leftrightarrow \frac{I_x}{\Delta z}.
\end{aligned} \tag{2.10}$$

2.2.1.1 Mesh Parameters

Assume a uniform 2-D shunt node where $\Delta l = \Delta x = \Delta y = \Delta z$. Using (2.6), the lumped-element values are related to the medium properties according to

$$\begin{aligned}
L' &= L'_x = L'_z = \mu_m \\
C' &= C'_y = \varepsilon_m/2.
\end{aligned} \tag{2.11}$$

Once the circuit elements are determined, they are replaced with transmission-lines to establish a two dimensional network. In order to satisfy the synchronization requirement, the propagation time, Δt on each link-line should be identical. Using (2.11) and from the transmission-line theory, the characteristic impedance, Z_0 and the propagation velocity, v_0 of the link-lines are obtained by

$$Z_0 = \sqrt{\frac{L'}{C'}} = \sqrt{2}\sqrt{\frac{\mu_m}{\varepsilon_m}}$$
$$v_0 = \frac{1}{\sqrt{L'C'}} = \sqrt{2}\frac{1}{\sqrt{\mu_m \varepsilon_m}}. \tag{2.12}$$

For the medium characterized by parameters (ε_m, μ_m), the characteristic impedance and the propagation velocity are, $Z_m = \sqrt{\mu_m / \varepsilon_m}$, and $v_m = 1/\sqrt{\mu_m \varepsilon_m}$, respectively. Expression (2.12) then implies

$$Z_0 = \sqrt{2} Z_m$$
$$v_0 = \sqrt{2} v_m. \tag{2.13}$$

The choice of parameters in (2.11) suits homogenous problems where the medium properties remain unchanged throughout the structure. To consider non-homogeneities, it is customary to define a host TLM mesh as a background medium, which is usually taken as free space, and introducing, whenever necessary, extra capacitances in the form of shunt stubs. To ensure synchronization, the length of the capacitive stub is taken to be equal to $\Delta l / 2$, with a propagation time $\Delta t / 2$. The characteristic impedance, Y_{os} of the stub is then determined to compensate for any deficiency in modeling the permittivity of the medium at the node location [5]

$$Y_{os} = \frac{4(\varepsilon_{r,m} - 1)}{Z_0} \tag{2.14}$$

where $\varepsilon_{r,m}$ is the relative permittivity of the medium at the node.

The existence of electric losses can easily be addressed in 2-D shunt scheme by introducing resistive loads in the form of matched stubs. Since the loss stub is matched, no incident impulses appear on it, and energy is simply removed from the node. For a medium with electric conductivity, $\sigma_{e,m}$ the characteristic admittance, G_{os} of the loss stub is [5]

$$G_{os} = \sigma_{e,m}\Delta l \tag{2.15}$$

2.2.1.2 Field Calculations in 2-D Shunt Node

The field calculations are easily carried out by using the Thevenin's equivalent model of the link-lines. Figure 2.3 illustrates the equivalent model of the 2-D shunt node when capacitive and electric loss stubs are included. Using Millman's theorem for parallel sources, the nodal voltage V_y is

$$V_y = \frac{2(V_1^i + V_2^i + V_3^i + V_4^i) + 2Z_0 Y_{os} V_s^i}{4 + Z_0 Y_{os} + Z_0 G_{os}}. \tag{2.16}$$

It is customary to normalize all characteristic impedances to Z_0. Expression (2.16) is then simplified to

$$V_y = \frac{2(V_1^i + V_2^i + V_3^i + V_4^i) + 2\hat{Y}_{os} V_{os}^i}{4 + \hat{Y}_{os} + \hat{G}_{os}}. \tag{2.17}$$

where $\hat{Y}_{os} = Z_0 Y_{os}$ and $\hat{G}_{os} = Z_0 G_{os}$.

Using Figure 2.2, the net currents in the x- and z-directions are

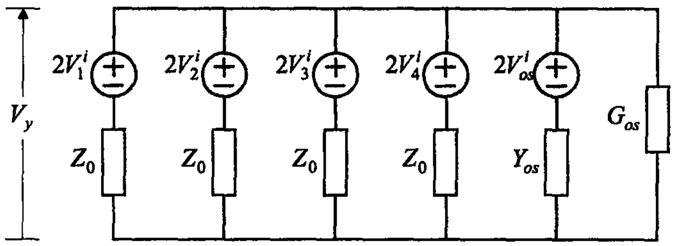

Figure 2.3: Thevenin's equivalent model of the 2-D shunt node with capacitive and lossy stubs.

$$I_x = \frac{V_1^i - V_3^i}{Z_0}$$
$$I_z = \frac{V_2^i - V_4^i}{Z_0}. \tag{2.18}$$

Using (2.17) and (2.18), and the mapping between the two models given in (2.10), the field values are evaluated as

$$E_y = -\frac{V_y}{\Delta l} = -\left[\frac{2(V_1^i + V_2^i + V_3^i + V_4^i) + 2\hat{Y}_{os}V_{os}^i}{(4 + \hat{Y}_{os} + \hat{G}_{os})\Delta l}\right]$$
$$H_x = -\frac{I_z}{\Delta l} = -\frac{V_1^i - V_3^i}{Z_0 \Delta l} \tag{2.20}$$
$$H_z = \frac{I_x}{\Delta l} = \frac{V_2^i - V_4^i}{Z_0 \Delta l}.$$

2.2.1.3 Field Excitations in 2-D Shunt Node

The excitation of a specific field is carried out by applying particular incident voltages on appropriate ports. As an example, to excite the node center with the field value, $E_y^{excitation}$ the following incident voltages can be applied on ports of the 2-D shunt node:

$$V_1^i = V_2^i = V_3^i = V_4^i = V_{os}^i = -E_y^{excitation}\Delta l. \tag{2.21}$$

Similarly, to excite $H_x^{excitation}$ one may set the incident impulses as

$$V_1^i = -V_3^i = -Z_0 \Delta l H_x^{excitation} / 2. \tag{2.22}$$

Finally, to excite $H_z^{excitation}$ the incident impulse can be set to

$$V_2^i = -V_4^i = Z_0 \Delta l H_z^{excitation} / 2. \tag{2.23}$$

2.2.1.4 Scattering Properties of 2-D Shunt Node

The scattering properties of the node are derived from the Thevenin's equivalent model in Figure 2.3 by evaluating the reflected impulses on each port. The reflected voltages are given by:

$$\begin{aligned}
{}_kV_1^r &= V_y - {}_kV_1^i = \frac{1}{\hat{Y}}\left[(2-\hat{Y})\,{}_kV_1^i + 2\,{}_kV_2^i + 2\,{}_kV_3^i + 2\,{}_kV_4^i + 2\hat{Y}_{os}V_{os}^i\right] \\
{}_kV_2^r &= V_y - {}_kV_2^i = \frac{1}{\hat{Y}}\left[2\,{}_kV_1^i + (2-\hat{Y})\,{}_kV_2^i + 2\,{}_kV_3^i + 2\,{}_kV_4^i + 2\hat{Y}_{os}V_{os}^i\right] \\
{}_kV_3^r &= V_y - {}_kV_3^i = \frac{1}{\hat{Y}}\left[2\,{}_kV_1^i + 2\,{}_kV_2^i + (2-\hat{Y})\,{}_kV_3^i + 2\,{}_kV_4^i + 2\hat{Y}_{os}V_{os}^i\right] \\
{}_kV_4^r &= V_y - {}_kV_4^i = \frac{1}{\hat{Y}}\left[2\,{}_kV_1^i + 2\,{}_kV_2^i + 2\,{}_kV_3^i + (2-\hat{Y})\,{}_kV_4^i + 2\hat{Y}_{os}V_{os}^i\right] \\
{}_kV_{os}^r &= V_y - {}_kV_{os}^i = \frac{1}{\hat{Y}}\left[2\,{}_kV_1^i + 2\,{}_kV_2^i + 2\,{}_kV_3^i + 2\,{}_kV_4^i + (2\hat{Y}_s - \hat{Y})V_{os}^i\right]
\end{aligned} \tag{2.24}$$

where $\hat{Y} = 4 + \hat{Y}_{os} + \hat{G}_{os}$.

2.2.1.5 Connection Properties of 2-D Shunt Node

The connection step at the k^{th} time step is carried out by simply exchanging the reflected impulses between the neighboring nodes to form the incident impulses at the $(k+1)^{st}$ time step. This is true only if the characteristic impedances of all link-lines are identical. For the case of variable or graded meshes, we must take into account the possibility of extra reflections at the nodes arms.

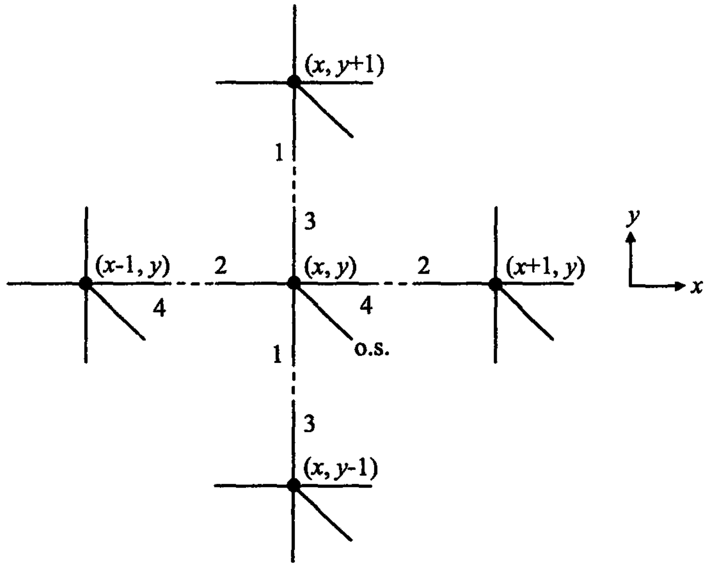

Figure 2.4: Connection in a mesh of 2-D shunt nodes.

Figure 2.4 illustrates the node located at the coordinate (x, y) with its neighboing nodes. The connection procedure is expressed by

$$\begin{aligned}
{}_{k+1}V_1^i(x,y) &= {}_kV_3^r(x,y-1) \\
{}_{k+1}V_2^i(x,y) &= {}_kV_4^r(x-1,y) \\
{}_{k+1}V_3^i(x,y) &= {}_kV_1^r(x,y+1) \\
{}_{k+1}V_4^i(x,y) &= {}_kV_2^r(x+1,y) \\
{}_{k+1}V_{os}^i(x,y) &= {}_kV_{os}^r(x,y).
\end{aligned} \tag{2.25}$$

The last expression in (2.25) relates the incident and reflected impulses on the capacitive stub. As this is modeled using an open-circuit stub with reflection coefficient $+1$, the reflected impulses at the k^{th} time step become incident at the $(k+1)^{st}$ time step. We note that in practical problems where different boundary conditions exist, the above algorithm should be modified to properly model these boundaries.

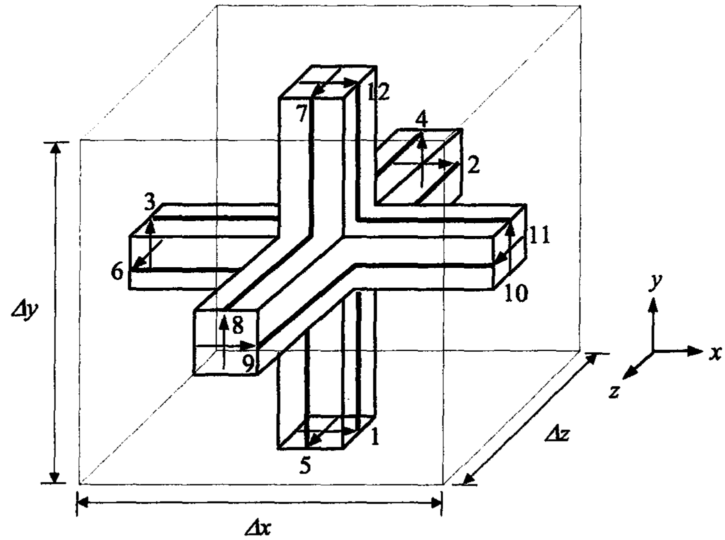

Figure 2.5: The symmetrical condensed node.

2.3 Three Dimensional TLM Nodes

The accurate analyses of many electromagnetic problems comprise 3-D modeling of the structure to obtain comprehensive information about the electromagnetic fields. In TLM, several topologies have been proposed as 3-D discretization elements. Among these is the symmetrical condensed node (SCN), initially proposed by Johns [2]. The SCN has received the greatest attention mainly because of its simplicity and the advantage of modelling all field components at the node center. The SCN has also become the basis of more advanced schemes including the hybrid and the generalized symmetrical condensed nodes [10]-[14].

The following section provides a review of the characteristics of the SCN including the mesh parameters, field calculations and excitations, and the scattering and connection properties.

2.3.1 The Symmetrical Condensed Node (SCN)

The symmetrical condensed node, in its basic form, is composed by the convergence of twelve transmission-lines, each with length $\Delta l/2$ and characteristic impedance Z_0. Figure 2.5 illustrates the node with adopted Johns convention for numbering the ports [2].

Each arm of the node is assumed to carry two orthogonal polarizations without any mutual coupling. It should be apparent that the node is only an abstraction for modeling the fields, and is not physically realizable.

The uniform node with $\Delta l = \Delta x = \Delta y = \Delta z$ can be used to model homogenous mediums where the material properties remain unchanged. In practical problems where non-homogeneities exist, a host TLM mesh is employed to model a background medium which is usually taken as free space, and deficiencies in modeling material properties are then compensated for by adding extra stubs at the node center.

To model a material with permittivity other than air, three open-circuit stubs for x, y and z polarizations are included (ports 13, 14 and 15, respectively). Similarly, three short-circuit stubs are added to model permeabilities other than that of the free space (ports 16, 17 and 18). To model electric and magnetic losses, six more stubs should be considered: three matched stubs in parallel with the capacitive stubs, (ports 19, 20 and 21), and three matched stubs in series with the inductive stubs (ports 22, 23 and 24).

A similar approach to the 2-D shunt scheme can be employed to establish the mappings between the circuit elements and the field components. The mappings used here are [5]

$$
\begin{aligned}
E_x &\leftrightarrow -\frac{V_x}{\Delta x} \quad , \quad E_y \leftrightarrow -\frac{V_y}{\Delta y} \quad , \quad E_z \leftrightarrow -\frac{V_z}{\Delta z} \\
H_x &\leftrightarrow \frac{I_x}{\Delta x} \quad , \quad H_y \leftrightarrow \frac{I_y}{\Delta y} \quad , \quad H_z \leftrightarrow \frac{I_z}{\Delta z}.
\end{aligned} \tag{2.26}
$$

2.3.1.1 Mesh Parameters

Consider a uniform block of free space with size Δl which is characterized by a single symmetrical condensed node. Each transmission-line of the twelve link-lines has a length of $\Delta l/2$, a propagation time $\Delta t/2$, and a characteristic impedance Z_0. The propagation velocity is equal to

$$
v_0 = \frac{\Delta l/2}{\Delta t/2} = \frac{\Delta l}{\Delta t}. \tag{2.27}
$$

From transmission-line theory, the associated capacitance and inductance of each link-line is $C_0 = \Delta t/(2Z_0)$ and $L_0 = Z_0 \Delta t/2$, respectively. The total capacitance and inductance for a given direction can then be obtained by taking into consideration the contribution of all four link-lines associated with a given direction. Therefore

$$
\begin{aligned}
C_{0x} &= \varepsilon_0 \frac{\Delta y \Delta z}{\Delta x} = \frac{2\Delta t}{Z_0} \\
C_{0y} &= \varepsilon_0 \frac{\Delta x \Delta z}{\Delta y} = \frac{2\Delta t}{Z_0} \\
C_{0z} &= \varepsilon_0 \frac{\Delta x \Delta y}{\Delta z} = \frac{2\Delta t}{Z_0}
\end{aligned}
$$

$$
\begin{aligned}
L_{0x} &= \mu_0 \frac{\Delta y \Delta z}{\Delta x} = 2Z_0 \Delta t \\
L_{0y} &= \mu_0 \frac{\Delta x \Delta z}{\Delta y} = 2Z_0 \Delta t \\
L_{0z} &= \mu_0 \frac{\Delta x \Delta y}{\Delta z} = 2Z_0 \Delta t.
\end{aligned} \tag{2.28}
$$

Consequently, the propagation velocity on the uniform mesh is derived as

$$v = \frac{\Delta l}{\sqrt{C_\xi L_\xi}} = \frac{1}{2}\frac{\Delta l}{\Delta t} = \frac{v_0}{2} \quad , \quad (\xi = x, y, z). \tag{2.29}$$

Expression (2.29) implies that the propagation velocity on the TLM mesh is half of the propagation velocity of impulses on each individual link-line. When the host network models free space, the simulation time step is

$$\Delta t = \frac{\Delta l}{2c} \tag{2.30}$$

where c is the speed of propagation in free space. Once the background network is characterized, the parameters of the extra stubs can be evaluated. We assume that the uniform block of Figure 2.5 is modeling a medium with permittivity ε. The required values of the total capacitances in each direction are

$$\begin{aligned} C_x &= \varepsilon \frac{\Delta y \Delta z}{\Delta x} \\ C_y &= \varepsilon \frac{\Delta x \Delta z}{\Delta y} \\ C_z &= \varepsilon \frac{\Delta x \Delta y}{\Delta z}. \end{aligned} \tag{2.31}$$

These capacitances are partly modeled by the background network, based on (2.28). The deficits should be compensated by adding open-circuit stubs with capacitances

$$\begin{aligned} C_x^s &= C_x - C_{0x} = \varepsilon \frac{\Delta y \Delta z}{\Delta x} - \frac{2\Delta t}{Z_0} \\ C_y^s &= C_y - C_{0y} = \varepsilon \frac{\Delta x \Delta z}{\Delta y} - \frac{2\Delta t}{Z_0} \\ C_z^s &= C_z - C_{0z} = \varepsilon \frac{\Delta x \Delta y}{\Delta z} - \frac{2\Delta t}{Z_0}. \end{aligned} \tag{2.32}$$

The associated characteristic admittances of the capacitive stubs are thus given by:

$$Y_x^s = \frac{2C_x^s}{\Delta t} = \frac{2\varepsilon \Delta y \Delta z}{\Delta x \Delta t} - \frac{4}{Z_0}$$
$$Y_y^s = \frac{2C_y^s}{\Delta t} = \frac{2\varepsilon \Delta x \Delta z}{\Delta y} - \frac{4}{Z_0} \tag{2.33}$$
$$Y_z^s = \frac{2C_z^s}{\Delta t} = \frac{2\varepsilon \Delta x \Delta y}{\Delta z} - \frac{4}{Z_0}.$$

It is customary to normalize all the impedances/admittances of the stubs to Z_0. Expressions (2.33) are simplified using $Z_0 = \sqrt{\mu_0/\varepsilon_0}$ and $v_0 = 1/\sqrt{\mu_0\varepsilon_0}$ to get

$$\hat{Y}_x^s = \frac{2\varepsilon_r}{v_0 \Delta t}\frac{\Delta y \Delta z}{\Delta x} - 4$$
$$\hat{Y}_y^s = \frac{2\varepsilon_r}{v_0 \Delta t}\frac{\Delta x \Delta z}{\Delta y} - 4 \tag{2.34}$$
$$\hat{Y}_z^s = \frac{2\varepsilon_r}{v_0 \Delta t}\frac{\Delta x \Delta y}{\Delta z} - 4.$$

A similar approach is employed to calculate the inductance deficit, and the normalized characteristic impedances of the required short-circuit stubs [5]

$$L_x^s = L_x - L_{0x} = \mu \frac{\Delta y \Delta z}{\Delta x} - 2\Delta t Z_0$$
$$L_y^s = L_y - L_{0y} = \mu \frac{\Delta x \Delta z}{\Delta y} - 2\Delta t Z_0\,, \tag{2.35}$$
$$L_z^s = L_z - L_{0z} = \mu \frac{\Delta x \Delta y}{\Delta z} - 2\Delta t Z_0$$

and

$$\hat{Z}_x^s = \frac{2\mu_r}{v_0 \Delta t}\frac{\Delta y \Delta z}{\Delta x} - 4$$
$$\hat{Z}_y^s = \frac{2\mu_r}{v_0 \Delta t}\frac{\Delta x \Delta z}{\Delta y} - 4 \tag{2.36}$$
$$\hat{Z}_z^s = \frac{2\mu_r}{v_0 \Delta t}\frac{\Delta x \Delta y}{\Delta z} - 4.$$

Electric and magnetic losses can be modeled using either infinitely long stubs or by using matched stubs. In either case the energy is absorbed from the node, and no incident impulses appear on the stubs. The required normalized admittances, $\hat{G}_\xi$ ($\xi = x, y, z$) and normalized impedances, $\hat{R}_\xi$ to model electric and magnetic losses are, respectively, given by [5]

$$\begin{array}{lll} \hat{G}_x = \sigma_{ex} Z_0 \dfrac{\Delta y \Delta z}{\Delta x} & , \ \hat{G}_y = \sigma_{ey} Z_0 \dfrac{\Delta x \Delta z}{\Delta y} & , \ \hat{G}_z = \sigma_{ez} Z_0 \dfrac{\Delta x \Delta y}{\Delta z} \\ \hat{R}_x = \sigma_{mx} \dfrac{\Delta y \Delta z}{\Delta x Z_0} & , \ \hat{R}_y = \sigma_{my} \dfrac{\Delta x \Delta z}{\Delta y Z_0} & , \ \hat{R}_z = \sigma_{mz} \dfrac{\Delta x \Delta y}{\Delta z Z_0} \end{array} \tag{2.37}$$

where $\sigma_{e\xi}$ and $\sigma_{e\xi}$ are the electric and magnetic conductivities in the ξ-direction, respectively.

2.3.1.2 Field Calculations in SCN

Let's consider the evaluation of the field components E_x and H_x. Figure 2.6 shows the link-lines contributing to these field elements. The center of the node is regard as an undefined region where the link-lines converge to form the condensed node. The total voltage in the x-direction can be evaluated by calculating the total charge on the SCN node and dividing it by the total capacitance in the x-direction. For the total incident charge one can write

$$\begin{aligned} Q_{incident} &= C_0 \left(V_1^i + V_2^i + V_9^i + V_{12}^i \right) + C_x^s \left(V_{13}^i \right) \\ &= \frac{\Delta t}{2Z_0} \left(V_1^i + V_2^i + V_9^i + V_{12}^i \right) + \frac{Y_x^s \Delta t}{2} \left(V_{13}^i \right). \end{aligned} \tag{2.38}$$

As no incident impulse appears on the loss stubs, they have no contribution on the total incident charge. The conservation of electric charge implies that the total incident

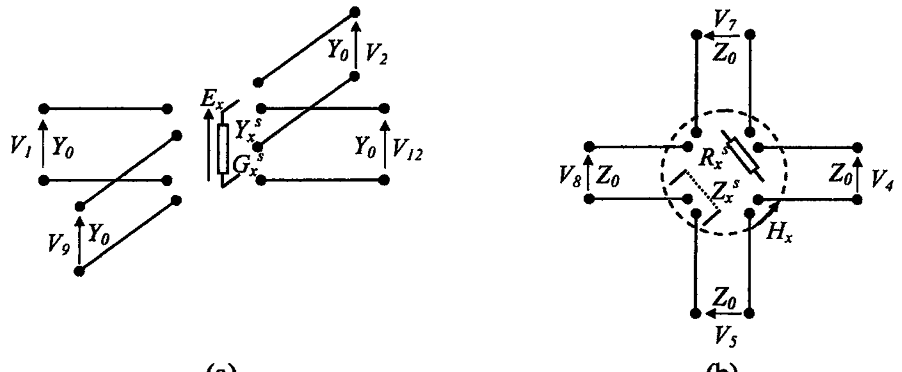

Figure 2.6: The symmetrical condensed node link-lines contributing to: (a) electric field component, E_x; (b) magnetic field component, H_x.

and the reflected charges should be equal. Hence

$$Q_{total} = Q_{incident} + Q_{reflected} = 2Q_{incident}. \tag{2.39}$$

The total capacitance in the x-direction is given by

$$C_{total} = 4C_0 + C_x^s + C_x^{loss} = \frac{2\Delta t}{Z_0} + Y_x^s \frac{\Delta t}{2} + G_x^s \frac{\Delta t}{2}. \tag{2.40}$$

Consequently, the total voltage in the x-direction, after normalizing all impedances/admittances of the stubs to Z_0, is

$$V_x = \frac{Q_{total}}{C_{total}} = \frac{2\left(V_1^i + V_2^i + V_9^i + V_{12}^i + \hat{Y}_x^s V_{13}^i\right)}{4 + \hat{Y}_x^s + \hat{G}_x^s}. \tag{2.41}$$

Using the mappings in (2.26), the field component E_x is derived as

$$E_x = -\frac{V_x}{\Delta x} = -\frac{2\left(V_1^i + V_2^i + V_9^i + V_{12}^i + \hat{Y}_x^s V_{13}^i\right)}{\Delta x\left(4 + \hat{Y}_x^s + \hat{G}_x^s\right)}. \tag{2.42}$$

From Figure 2.6b, it can be seen that the ports contributing to the current I_x are ports 4, 5, 7 and 8. Using Thevenin's equivalent model of transmission-lines, the total voltage is

$$V_{total} = 2\left(V_4^i - V_5^i + V_7^i - V_8^i - V_{16}^i\right). \tag{2.43}$$

The associated total impedance is $Z_{total} = 4Z_0 + Z_x^s + R_x^s$. After normalizing the impedances to Z_0, the current I_x is evaluated as

$$I_x = \frac{V_{total}}{Z_{total}} = \frac{2\left(V_4^i - V_5^i + V_7^i - V_8^i - V_{16}^i\right)}{Z_0\left(4 + \hat{Z}_x^s + \hat{R}_x^s\right)} \tag{2.44}$$

Accordingly,

$$H_x = \frac{I_x}{\Delta x} = \frac{2\left(V_4^i - V_5^i + V_7^i - V_8^i - V_{16}^i\right)}{\Delta x Z_0\left(4 + \hat{Z}_x^s + \hat{R}_x^s\right)} \tag{2.45}$$

Similar procedure can be followed to evaluate the other field components.

2.3.1.3 Field Excitations in SCN

The excitation of a desire field component is carried out by applying particular incident impulses on appropriate ports. Consider the excitation of the electric field $E_x^{excitation}$ in the x-direction. One possible solution is selecting the incident impulses as

$$V_1^i = V_2^i = V_9^i = V_{12}^i = V_{13}^i = -E_x^{excitation}\Delta x / 2 \tag{2.46}$$

Similarly, to excite the magnetic field $H_x^{excitation}$ in the x-direction, the appropriate incident impulses can be taken as

$$\begin{aligned} V_4^i = V_7^i &= \Delta x Z_0\left(\frac{4Z_0 + \hat{R}_x^s}{8}\right)H_x^{excitation} \\ V_5^i = V_8^i &= -\Delta x Z_0\left(\frac{4Z_0 + \hat{R}_x^s}{8}\right)H_x^{excitation} \end{aligned} \tag{2.47}$$

2.3.1.4 Scattering Properties of SCN

The scattering properties of the SCN node can be derived using the method described in [15]. This method simply applies the conservation principles of electric charge and magnetic flux density and enforces the continuity of the electric and magnetic fields. Using the nodal voltages V_x, V_y, and V_z, and the loop currents I_x, I_y, and I_z the reflected impulses into all ports can be determined. For the twelve link-lines which form the standard SCN the reflected impulses are

$$
\begin{aligned}
V_1^r &= V_x - Z_0 I_z - V_{12}^i \\
V_2^r &= V_x + Z_0 I_y - V_9^i \\
V_3^r &= V_y + Z_0 I_z - V_{11}^i \\
V_4^r &= V_y - Z_0 I_x - V_8^i \\
V_5^r &= V_z + Z_0 I_x - V_7^i \\
V_6^r &= V_z - Z_0 I_y - V_{10}^i \\
V_7^r &= V_z - Z_0 I_x - V_5^i \\
V_8^r &= V_y + Z_0 I_x - V_4^i \\
V_9^r &= V_x - Z_0 I_y - V_2^i \\
V_{10}^r &= V_z + Z_0 I_y - V_6^i \\
V_{11}^r &= V_y - Z_0 I_z - V_3^i \\
V_{12}^r &= V_x + Z_0 I_z - V_1^i .
\end{aligned}
\tag{2.48a}
$$

For the capacitive stubs (ports 13, 14, and 15), and the inductive stubs (ports 16, 17 and 18) the reflected impulses are

$$
\begin{aligned}
V_{13}^r &= V_x - V_{13}^i \\
V_{14}^r &= V_x - V_{14}^i \\
V_{15}^r &= V_x - V_{15}^i
\end{aligned}
$$

$$V_{16}^{r} = Z_0 \hat{Z}_x^s I_x + V_{16}^{i}$$
$$V_{17}^{r} = Z_0 \hat{Z}_y^s I_y + V_{17}^{i} \qquad (2.48b)$$
$$V_{18}^{r} = Z_0 \hat{Z}_z^s I_z + V_{18}^{i}.$$

Finally, the reflected impulses on electric loss stubs (ports 19, 20 and 21), and magnetic loss stubs (ports 22, 23 and 24) are given as

$$V_{19}^{r} = V_x$$
$$V_{20}^{r} = V_y$$
$$V_{21}^{r} = V_z$$
$$V_{22}^{r} = Z_0 \hat{R}_x^s I_x$$
$$V_{23}^{r} = Z_0 \hat{R}_y^s I_y \qquad (2.48c)$$
$$V_{24}^{r} = Z_0 \hat{R}_z^s I_z.$$

2.3.1.5 Connection Properties of SCN

For a uniform mesh where the characteristic impedances of all link-lines are identical and equal to Z_0, the connection step is implemented simply by exchanging the reflected impulse between the neighboring nodes. As the capacitive stubs are modeled by open-circuit stubs, the reflected impulses become incident in the next time step with a reflection coefficient $+1$. However, for the inductive stubs modeled by short-circuit stubs, the reflection coefficient is -1.

Consider the node located at the coordinate (x, y, z). The connection step for the twelve link-lines of the standard SCN are

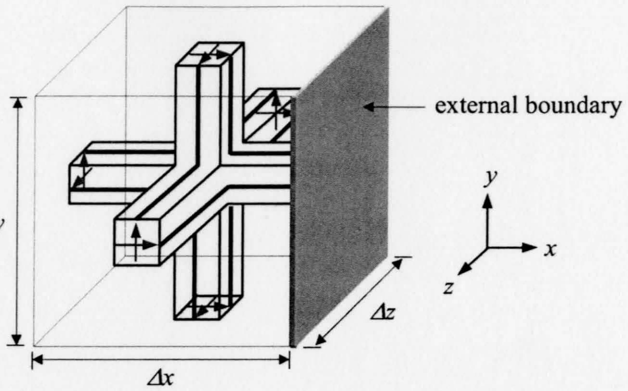

Figure 2.7: External boundary placed at the node arm of the symmetrical condensed node.

$$
\begin{aligned}
{}_{k+1}V_1^i(x,y,z) &= {}_kV_{12}^r(x,y-1,z) & {}_{k+1}V_7^i(x,y,z) &= {}_kV_5^r(x,y+1,z) \\
{}_{k+1}V_2^i(x,y,z) &= {}_kV_9^r(x,y,z-1) & {}_{k+1}V_8^i(x,y,z) &= {}_kV_4^r(x,y,z+1) \\
{}_{k+1}V_3^i(x,y,z) &= {}_kV_{11}^r(x-1,y,z) & {}_{k+1}V_9^i(x,y,z) &= {}_kV_2^r(x,y,z+1) \\
{}_{k+1}V_4^i(x,y,z) &= {}_kV_8^r(x,y,z-1) & {}_{k+1}V_{10}^i(x,y,z) &= {}_kV_6^r(x+1,y,z) \\
{}_{k+1}V_5^i(x,y,z) &= {}_kV_7^r(x,y-1,z) & {}_{k+1}V_{11}^i(x,y,z) &= {}_kV_3^r(x+1,y,z) \\
{}_{k+1}V_6^i(x,y,z) &= {}_kV_{10}^r(x-1,y,z) & {}_{k+1}V_{12}^i(x,y,z) &= {}_kV_1^r(x,y+1,z).
\end{aligned} \quad 2.49a)
$$

The connection procedure for the capacitive and inductive stubs are expressed as

$$
\begin{aligned}
{}_{k+1}V_{13}^i(x,y,z) &= {}_kV_{13}^r(x,y,z) & {}_{k+1}V_{16}^i(x,y,z) &= -{}_kV_{16}^r(x,y,z) \\
{}_{k+1}V_{14}^i(x,y,z) &= {}_kV_{14}^r(x,y,z) & {}_{k+1}V_{17}^i(x,y,z) &= -{}_kV_{17}^r(x,y,z) \\
{}_{k+1}V_{15}^i(x,y,z) &= {}_kV_{15}^r(x,y,z) & {}_{k+1}V_{18}^i(x,y,z) &= -{}_kV_{18}^r(x,y,z).
\end{aligned} \quad (2.49b)
$$

As the electric and magnetic loss stubs are terminated with matched loads, no incident impulses appear on them. This condition is enforced separately on the loss stubs

$$
\begin{aligned}
{}_{k+1}V_{19}^i(x,y,z) &= 0 & {}_{k+1}V_{22}^i(x,y,z) &= 0 \\
{}_{k+1}V_{20}^i(x,y,z) &= 0 & {}_{k+1}V_{23}^i(x,y,z) &= 0 \\
{}_{k+1}V_{21}^i(x,y,z) &= 0 & {}_{k+1}V_{24}^i(x,y,z) &= 0.
\end{aligned} \quad (2.49c)
$$

2.4 Boundary Conditions in TLM

In TLM, external boundaries are place halfway between the nodes, at the node arms. This is illustrated in Figure 2.7 for the symmetrical condensed node.

In many problems, the property of the boundary can be expressed by a single reflection coefficient, Γ_b. This reflection coefficient is then translated to an equivalent load resistance using the medium properties. We denote by Z_m the characteristic impedance of the medium where the wave is propagating. The resistance associated with the reflection coefficient, Γ_b is

$$Z_b = Z_m \frac{1+\Gamma_b}{1-\Gamma_b}. \tag{2.50}$$

The resistance Z_b can be regarded as the load which terminates the TLM mesh to provide the mesh reflection coefficient, Γ_b. The reflection coefficient of each individual link-line, however is different and is given by

$$\Gamma_l = \frac{Z_b - Z_0}{Z_b + Z_0} = \frac{Z_m(1+\Gamma_b) - Z_0(1-\Gamma_b)}{Z_m(1+\Gamma_b) + Z_0(1-\Gamma_b)}, \tag{2.51}$$

where Z_0 is the characteristic impedance of line-lines. For example, consider the following cases where the external boundary can be represented by a single reflection coefficient.

Short-circuit (electric-wall):

$$\Gamma_b = -1 \rightarrow \Gamma_l = -1. \tag{2.52}$$

Open-circuit (magnetic-wall):

$$\Gamma_b = 1 \rightarrow \Gamma_l = 1. \tag{2.54}$$

Match-load:

$$\Gamma_b = 0 \rightarrow \Gamma_l = \frac{Z_m - Z_0}{Z_m + Z_0}. \tag{2.55}$$

In another group of TLM problems, absorbing boundaries are required to truncate the computational domain. Examples are antenna radiation and scattering problems. Ideally, no reflections from an absorbing boundary into the computational domain should occur. Several techniques have been developed for this purpose. In this thesis, discrete Green's function approach or Johns' matrix boundary [7, 8] is used extensively. The idea behind the Johns' matrix is to obtain the response of a TLM mesh to unit impulse excitations at specific nodes. As TLM forms a linear system, the response of the network to an arbitrary excitation is evaluated by convolving the excitation with the Johns' matrix. In order to model an absorbing boundary for a waveguide, a long enough section of the waveguide is simulated beforehand. The waveguide should be long in order to ensure that no reflections from the far end reach the input reference place before the computation is terminated. This technique is specifically useful when the waveguide is excited with its dominant mode profile. In [7] it is shown that the Johns' matrix in this cases reduces to a vector which results in considerable storage saving. For a TLM problem with Johns' matrix absorbing boundaries, the TLM expression in (2.1) is rewritten as

$$_{k+1}\boldsymbol{V} = \boldsymbol{CS}\,{}_{k}\boldsymbol{V} + \sum_{k'=0}^{k} \boldsymbol{J}(k-k')\,{}_{k'}\boldsymbol{V}^{r} + {}_{k}\boldsymbol{V}^{s} \quad , \quad \boldsymbol{V}(0) = \boldsymbol{0} \tag{2.56}$$

where $\boldsymbol{J}(k) \in \mathbb{R}^{N_L \times N_L}$ is the k^{th} time layer of the three dimensional Johns' matrix.

REFERENCES

[1] P.B. Johns and R.L.Beurle, "Numerical modeling of 2-dimensional scattering problems using a transmission line matrix," *Proceedings of IEE,* vol. 118, no. 9, pp. 1203-1208, Sept.1971.

[2] P.B. Johns, "A symmetrical condensed node for the TLM method," *IEEE Trans. Microwaves Theory Tech.*, vol. 35, no. 4, pp. 370-377, April 1987.

[3] W.J.R. Hoefer, "The transmission line matrix (TLM) method", *Numerical Techniques for microwave and millimeter-wave passive structures,* edited by T. Itoh, John Wiley and sons, 1989.

[4] W.J.R. Hoefer, "The transmission line matrix method- Theory and applications," *IEEE Trans. Microwaves Theory Tech.*, vol. 33, no. 10, pp. 882-893, Oct. 1985.

[5] C. Christopoulos, *The Transmission-Line Modeling Method TLM.* IEEE PRESS. 1995.

[6] S. Akhtarzad and P.B Johns, "Solution of Maxwell's equations in three space dimensions and time by the TLM method of numerical analysis," *Proceedings of IEE,* vol. 122, pp. 1349-1352, Dec. 1975.

[7] W. J. Hoefer, "The discrete time domain green's function or Johns' matrix- a new powerful concept in transmission line modeling (TLM)," *Int. Journal of Numerical Modeling: Electronic Networks, Devices and Fields,* vol. 2, pp. 215-225, Dec.1989.

[8] E. G. Costache and W. J. Hoefer, " TLM modeling of dispersive wide-band absorbing boundaries with time domain diakoptics for S-parameter extraction," *IEEE Trans. Microwave Theory Tech.,* vol. 38, no. 4, pp. 379- 385, April 1990.

[9] P. Naylor, "Using 2-D series TLM for modelling TE modes in dielectric and lossy environment," *Electronics Lett.,* vol. 27, no. 17, pp. 1499-1500, Aug. 1991.

[10] R. A. Scaramuzza and A.J. Lowery, "Hybrid symmetrical condensed node for TLM method," *Electronics Lett.*, vol. 26, no. 23, pp. 1947-1949, Nov. 1990.

[11] P. Berini and K. Wu, "A pair of hybrid symmetrical condensed node," *IEEE Microwave and guided wave letters*, vol. 4, no. 7, pp. 244-246, July 1994.

[12] V. Trenkic, C. Christopoulos and T.M. Benson, "New symmetrical super condensed node for TLM method," *Electronics lett.*, vol. 30, no. 4, pp. 329-330, Feb. 1994.

[13] V. Trenkic, C. Christopoulos and T. M. Benson, "Development of a general symmetrical condensed node for the TLM method," *IEEE Trans. Microwaves Theory Tech.*, vol. 44, no. 12, pp. 2129-2135, Dec. 1996.

[14] V. Trenkic, C. Christopoulos and T.M. Benson, "Generally graded mesh using the symmetrical super condensed node," *Electronics lett.*, vol. 30, no. 10, pp. 795-797, May 1994,

[15] V. Trenkic, C. Christopoulos and T.M. Benson, "Simple and elegant formulation of scattering in TLM nodes," *Electronics lett.*, vol. 29, no. 18, pp. 1651-1652, Sept. 1993.

Chapter 3

THE ADJOINT-VARIABLE METHOD FOR SENSITVITY ANALYSIS OF TIME-DOMAIN TLM PROBLEMS

Sensitivity analysis of high-frequency electromagnetic (EM) structures is essential in a vast group of EM problems including gradient-based optimization, statistical analysis, as well as the tolerance and yield analyses [1]. Traditional full-wave analysis approaches for extracting sensitivity information of the system response in the design parameter space require extensive time which makes them inefficient. For an electromagnetic structure, the design problem can be expressed as

$$x^* = \arg\{\min_{x} F(x, \boldsymbol{R}(x))\} \tag{3.1}$$

where x^* is the set of optimal parameters, $\boldsymbol{R}(x)$ is the vector of responses, and F is the objective function. The problem (3.1) is usually solved using gradient-based optimizers. These optimizers require not only the structure response but also its derivatives. The classical approach for extracting sensitivities using finite differences can be time-intensive even for problems with a small number of design parameters.

Adjoint variable methods (AVMs) have been recently developed and incorporated with time-domain TLM problems for efficient sensitivity analysis [2]-[3]. AVM estimates the gradient of a given objective function using only two simulations of the original system and an auxiliary system, referred to as the adjoint system.

This chapter provides the mathematical background of the sensitivity analysis of time-domain TLM problems using the novel technique of the adjoint variable method.

3.1 Adjoint-Sensitivity Analysis for TLM Method

In the adjoint-variable method for TLM, the design sensitivity is obtained through estimating the gradient of a real-valued objective function, $F(\boldsymbol{x},\boldsymbol{V})$ which is taken in the form

$$F(\boldsymbol{x},\boldsymbol{V}) = \int_0^{T_{\max}} \iiint_{\Omega} \psi(\boldsymbol{x},\boldsymbol{V}) d\Omega dt = \int_0^{T_{\max}} \Psi(\boldsymbol{x},\boldsymbol{V}) dt \tag{3.2}$$

where

$\psi(\boldsymbol{x},\boldsymbol{V})$ is the objective function's kernel. It is a differentiable function of the vector of incident impulses, $\boldsymbol{V}$ and the vector of design parameters $\boldsymbol{x}$,

$T_{\max}$ is the simulation time, and

Ω is the observation domain where the objective function is evaluated.

The objective function in (3.2) is the system's global performance measure. The design sensitivity analysis underlies the estimation of the gradient vector of the objective function, defined by

$$\nabla \boldsymbol{F} = \begin{bmatrix} \dfrac{\partial F}{\partial x_1} & \cdots & \dfrac{\partial F}{\partial x_n} \end{bmatrix}. \tag{3.3}$$

Using the chain rule of differentiation, the i^{th} element of the gradient vector can be expressed as follows

$$\frac{\partial F}{\partial x_i} = \frac{\partial^e F}{\partial x_i} + \int_0^{T_{\max}} \left(\frac{\partial \Psi}{\partial V}\right)^T \frac{\partial V}{\partial x_i} dt \tag{3.4}$$

where $\partial^e F/\partial x_i$ indicates the explicit dependency of the objective function on the i^{th} design parameter which is usually equal to zero. The explicit dependency of the kernel function on the vector of incident impulses is known beforehand, so the derivative term inside the integrand can be evaluated for the entire simulation time. However, the vector of incident impulses has an implicit dependency on the design parameters, and the sensitivity expression in (3.4) should be evaluated indirectly. Two possible approaches for sensitivity estimation are the direct differentiation, and the adjoint-variable method. The former is costly in terms of the simulation time. Using forward/backward or central-difference approximations require $(n+1)$ and $(2n+1)$ system analyses, respectively. It is apparent that even for a small number of design parameters direct differentiations is impractical.

The adjoint-variable method, on the other hand, estimates the sensitivity expression in (3.4), using at the most two system analyses by employing an auxiliary system, referred to as the adjoint system.

Assume a band-limited excitation where smooth field variations exist between successive simulation samples for the entire simulation time. Satisfying this condition, the vector of incident impulses at the $(k+1)^{\text{st}}$ time step can be approximated using the first two terms of the Taylor's series as [2]

$$
\begin{aligned}
{}_{k+1}V = V(k\Delta t + \Delta t) &\approx V(k\Delta t) + \left(\frac{\partial V}{\partial t}\right)\Delta t \\
&\approx {}_kV + {}_k\!\left(\frac{\partial V}{\partial t}\right)\Delta t.
\end{aligned} \tag{3.5}
$$

Using (3.5), the TLM simulation is reformulated to [2]

$$
{}_kV + {}_k\!\left(\frac{\partial V}{\partial t}\right)\Delta t = C(x)S(x)\,{}_kV + {}_kV^s. \tag{3.6}
$$

Simplifying (3.6), we get

$$
\left(\frac{\partial V}{\partial t}\right) = A(x)V + \frac{V^s}{\Delta t} \tag{3.7}
$$

where $A(x) = \left[C(x)S(x) - I/\Delta t\right]$ is defined as the TLM system matrix, and I is the identity matrix. The time step subscript was dropped to imply that the expression is valid at any time during the simulation. Let Δx_i denotes a one-cell perturbation in the i^{th} design parameter. The associated changes in the vector of incident impulses and the system matrix are denoted by ΔV_i and ΔA_i, respectively. For the perturbed structure, (3.7) becomes

$$
\frac{\partial}{\partial t}\left(V + \Delta V_i\right) = \left(A(x) + \Delta A_i\right)\left(V + \Delta V_i\right) + \frac{V^s}{\Delta t}. \tag{3.8}
$$

Dividing both sides by Δx_i we get

$$
\frac{\partial}{\partial t}\left(\frac{\Delta V_i}{\Delta x_i}\right) = \frac{\Delta A_i}{\Delta x_i}V + A(x)\frac{\Delta V_i}{\Delta x_i} + \frac{\Delta A_i \Delta V_i}{\Delta x_i}. \tag{3.9}
$$

Taking the limit of (3.9) as $\Delta x_i \to 0$ gives

$$
\frac{\partial^2 V}{\partial x_i \partial t} - \frac{\Delta A_i}{\Delta x_i}V - A(x)\frac{\Delta V_i}{\Delta x_i} - \Delta A_i\frac{\partial V}{\partial x_i} \approx 0. \tag{3.10}
$$

The terms containing the variation of the system matrix are kept unchanged, as later in the derivation the discrete form will be used. Multiplying both sides of (3.10) by the transpose of the adjoint vector, $\boldsymbol{\lambda}$, we get [5]

$$\int_0^{T_{\max}} \boldsymbol{\lambda}^T \left(\frac{\partial^2 \boldsymbol{V}}{\partial x_i \partial t} - \frac{\Delta \boldsymbol{A}_i}{\Delta x_i} \boldsymbol{V} - \boldsymbol{A}(\boldsymbol{x}) \frac{\partial \boldsymbol{V}}{\partial x_i} - \Delta \boldsymbol{A}_i \frac{\partial \boldsymbol{V}}{\partial x_i} \right) dt \approx 0. \tag{3.11}$$

Integrating (3.11) by parts yields

$$\boldsymbol{\lambda}^T \frac{\partial \boldsymbol{V}}{\partial x_i}\bigg|_0^{T_{\max}} - \int_0^{T_{\max}} \left(\frac{d\boldsymbol{\lambda}^T}{dt} + \boldsymbol{\lambda}^T \left(\boldsymbol{A} + \Delta \boldsymbol{A}_i \right) \frac{\partial \boldsymbol{V}}{\partial x_i} \right) dt = \int_0^{T_{\max}} \boldsymbol{\lambda}^T \frac{\Delta \boldsymbol{A}_i}{\Delta x_i} \boldsymbol{V} dt. \tag{3.12}$$

The vector of the adjoint impulses is assumed to satisfy the terminal condition $\boldsymbol{\lambda}(T_{\max}) = \boldsymbol{0}$. The initial condition of the original simulation requires that $\boldsymbol{V}(0) = \boldsymbol{0}$. It follows that the first term in the last expression vanishes. Comparing the left-hand side of (3.12) with the second term of (3.4), suggests the following expression for the vector of adjoint impulses

$$\frac{d\boldsymbol{\lambda}}{dt} + (\boldsymbol{A} + \Delta \boldsymbol{A}_i)^T \boldsymbol{\lambda} = \frac{\partial \Psi}{\partial \boldsymbol{V}}. \tag{3.13}$$

Using backward finite-difference approximations, the first term in (3.13) is given by

$$\frac{d\boldsymbol{\lambda}}{dt} \approx \frac{{}_k\boldsymbol{\lambda} - {}_{k-1}\boldsymbol{\lambda}}{\Delta t}. \tag{3.14}$$

The second term in (3.13) can be expanded as

$$\left(\boldsymbol{A} + \Delta \boldsymbol{A}_i \right)^T = \frac{\boldsymbol{S}^T (\boldsymbol{x} + \Delta \boldsymbol{x}_i) \boldsymbol{C}^T (\boldsymbol{x} + \Delta \boldsymbol{x}_i) - \boldsymbol{I}}{\Delta t} \tag{3.15}$$

where $\boldsymbol{S}(\boldsymbol{x} + \Delta \boldsymbol{x}_i)$ and $\boldsymbol{C}(\boldsymbol{x} + \Delta \boldsymbol{x}_i)$ are the system scattering and connection matrices of the perturbed problem. The vector, $\Delta \boldsymbol{x}_i$ is defined as the perturbation vector with non-zero element only at the i^{th} element, where its value is Δx_i. Inserting (3.14) and (3.15) in (3.13) results in a TLM simulation for the adjoint vector

$$_{k-1}\boldsymbol{\lambda} = \boldsymbol{S}^T(\boldsymbol{x}+\Delta\boldsymbol{x}_i)\boldsymbol{C}^T(\boldsymbol{x}+\Delta\boldsymbol{x}_i)\,_k\boldsymbol{\lambda} - \,_k\boldsymbol{\lambda}^s \quad , \quad \boldsymbol{\lambda}(T_{\max}) = \boldsymbol{0} \tag{3.16}$$

with the adjoint excitation given by

$$_k\boldsymbol{\lambda}^s = \,_k(\frac{\partial \Psi}{\partial \boldsymbol{V}})\Delta t. \tag{3.17}$$

The implementation of (3.16) is impractical as the vector of adjoint impulses is derived from a perturbed problem. An approximation is thus necessary to estimate the adjoint vector from the unperturbed structure. In fact, we assume that perturbation done in each parameter is small and does not significantly affect the distribution of the incident impulses. Accordingly, the required adjoint impulses in (3.16) are approximated by the values of the corresponding incident impulses for the unperturbed adjoint problem

$$_{k-1}\boldsymbol{\lambda} = \boldsymbol{S}^T(\boldsymbol{x})\boldsymbol{C}^T(\boldsymbol{x})\,_k\boldsymbol{\lambda} - \,_k\boldsymbol{\lambda}^s \quad , \quad \boldsymbol{\lambda}(T_{\max}) = \boldsymbol{0}. \tag{3.18a}$$

When Johns matrix absorbing boundaries are employed, it is shown that the TLM simulation of the adjoint problem can be expressed as [3]

$$_{k-1}\boldsymbol{\lambda} = \boldsymbol{S}^T(\boldsymbol{x})\left[\boldsymbol{C}^T(\boldsymbol{x})\,_k\boldsymbol{\lambda} + \sum_{k'}^{N_t}\boldsymbol{J}^T(k'-k)\,_{k'}\boldsymbol{\lambda}\right] - \,_k\boldsymbol{\lambda}^s \quad , \quad \boldsymbol{\lambda}(T_{\max}) = \boldsymbol{0}. \tag{3.18b}$$

The following points should be made regarding the TLM simulation of the adjoint system:

- The AVM simulation runs backward in time starting at $t = T_{\max}$, with the terminal condition $\boldsymbol{\lambda}(T_{\max}) = \boldsymbol{0}$.
- The system scattering and connection matrices of the adjoint system are the transpose of those in the original system.

- The order of the scattering and the connection steps in the adjoint system is reversed.
- The excitation of the adjoint system is obtained from the original simulation. Hence the two simulations can not be run in parallel.
- Both the original and the adjoint simulations are obtained from the unperturbed structure.

Returning to the sensitivity expression in (3.4), the i^{th} element of the gradient vector of the objective function is approximated to obtain

$$\begin{aligned}\frac{\partial F}{\partial x_i} &\approx \frac{\partial^e F}{\partial x_i} - \int_0^{T_{max}} \boldsymbol{\lambda}^T \frac{\Delta A_i}{\Delta x_i} \boldsymbol{V} dt \\ &\approx \frac{\partial^e F}{\partial x_i} - \sum_{k=0}^{N_t} {}_k\boldsymbol{\lambda}^T {}_k\boldsymbol{\eta}^i\end{aligned} \tag{3.19}$$

where ${}_k\boldsymbol{\eta}^i = [\Delta A_i / \Delta x_i]\, {}_k\boldsymbol{V}$, and N_t is the total number of simulation time steps. It should be noted that the vector ${}_k\boldsymbol{\eta}^i$ has a small number of non-zero elements. This it apparent from the fact that the variation of the system matrix, ΔA_i is non-zero only for the TLM nodes which are directly affected by the one-cell perturbation. In practice, only the non-zero elements are stored and employed in the sensitivity estimations. A detailed discussion about determining the elements of the vector ${}_k\boldsymbol{\eta}^i$ for the general cases when the structure undergoes perturbations in the physical dimensions as well as the material properties is provided in the next section.

3.1.1 Practical Implementation

The vector ${}_k\boldsymbol{\eta}^i$ plays an important role in the TLM-AVM algorithm. It simply reflects the variation of the system matrix and its elements depend on the way link-lines are affected by the perturbation. In general

$$ {}_k\boldsymbol{\eta}^i = \frac{\Delta \boldsymbol{A}_i}{\Delta x_i}\,{}_k\boldsymbol{V} = \frac{1}{\Delta x_i}\left[\Delta \boldsymbol{C}_i \boldsymbol{S}(\boldsymbol{x}) + \boldsymbol{C}(\boldsymbol{x})\Delta \boldsymbol{S}_i\right]{}_k\boldsymbol{V} \tag{3.20} $$

where $\Delta\boldsymbol{S}_i = \boldsymbol{S}(\boldsymbol{x}+\Delta x_i) - \boldsymbol{S}(\boldsymbol{x})$ and $\Delta\boldsymbol{C}_i = \boldsymbol{C}(\boldsymbol{x}+\Delta x_i) - \boldsymbol{C}(\boldsymbol{x})$ are the variations in the system scattering and connection matrices, respectively. The first term in (3.20) addresses the case when Δx_i is due to a metallic discontinuity, while the second term includes the perturbations due to dielectric/magnetic discontinuities.

3.1.1.1 Metallic Discontinuities

The variations of the system matrix due to a perturbation in a metallic discontinuity is realized by associated changes in the system connection matrix, while the system scattering matrix remains unchanged:

$$ \Delta \boldsymbol{A}_i = \frac{\Delta \boldsymbol{C}_i \boldsymbol{S}(\boldsymbol{x})}{\Delta t} = \frac{\boldsymbol{C}(\boldsymbol{x}+\Delta x_i)\boldsymbol{S}(\boldsymbol{x}) - \boldsymbol{C}(\boldsymbol{x})\boldsymbol{S}(\boldsymbol{x})}{\Delta t}. \tag{3.21} $$

Consider the case where the link-lines with indices m and n are connected together, and the perturbation Δx_i results in metallizing the node of the n^{th} link. Using (3.21), the m^{th} component of the vector ${}_k\boldsymbol{\eta}^i$ is

$$ \begin{aligned} {}_k\eta^i_m = \left(\frac{\Delta \boldsymbol{A}_i}{\Delta x_i}\,{}_k\boldsymbol{V}\right)_m &= \frac{1}{\Delta x_i \Delta t}\left[\boldsymbol{C}(\boldsymbol{x}+\Delta x_i)\boldsymbol{S}(\boldsymbol{x})\,{}_k\boldsymbol{V} - \boldsymbol{C}(\boldsymbol{x})\boldsymbol{S}(\boldsymbol{x})\,{}_k\boldsymbol{V}\right]_m \\ &= \frac{1}{\Delta x_i \Delta t}\left[\boldsymbol{C}(\boldsymbol{x}+\Delta x_i)\,{}_k\boldsymbol{V}^r - \boldsymbol{C}(\boldsymbol{x})\,{}_k\boldsymbol{V}^r\right]_m. \end{aligned} \tag{3.22} $$

As the m^{th} link-line observes a metallic boundary after the perturbation, the first term in (3.22) is evaluated as

$$\left[C(x+\Delta x_i)\,{}_k V^r\right]_m = {}_{k+1}V_m = -{}_k V^r_m. \tag{3.23}$$

On the other hand, the second term in (3.22) refers to the unperturbed problem. As the m^{th} and n^{th} link-lines are connected to each other, this term can be simplified to

$$\left[C(x)\,{}_k V^r\right]_m = {}_{k+1}V_m = {}_k V^r_n. \tag{3.24}$$

Inserting (3.23) and (3.24) into (3.22), gives

$$ {}_k\eta^i_m = -\frac{1}{\Delta x_i \Delta t}\left({}_k V^r_m + {}_k V^r_n\right). \tag{3.25}$$

Similar argument shows that when the perturbation removes the metallization of the node of the n^{th} link-line, the m^{th} element of ${}_k\eta^i$ is evaluated as

$$ {}_k\eta^i_m = \frac{1}{\Delta x_i \Delta t}\left({}_k V^r_m + {}_k V^r_n\right). \tag{3.26}$$

Figure 3.1 illustrates snapshots of the impulses in the original and the adjoint simulations which determine the final impulse storage in the two simulations.

3.1.1.2 Dielectric Discontinuities

When the structure experiences a perturbation due to a dielectric discontinuity, the variations in the system matrix is realized through the associated changes in the system scattering matrix. In this case the system connection matrix remains unchanged. This becomes clear by noticing that a dielectric perturbation only affects the nodal scattering property which depends on the medium constitutive parameters. In mathematical form we have

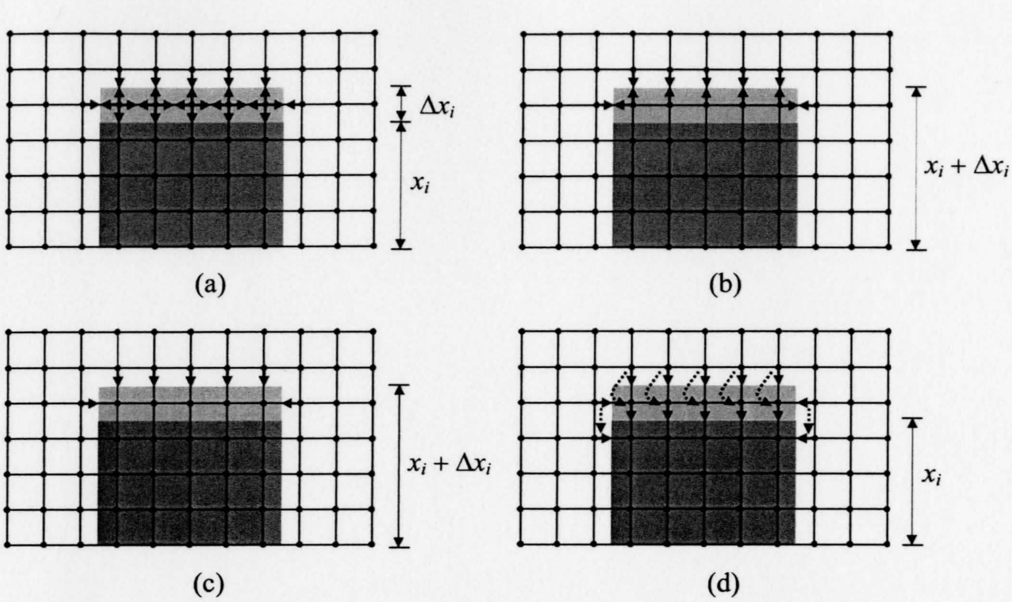

Figure 3.1: Illustration of the impulse storage for the original and the adjoint simulations for a metallic discontinuity at the k^{th} time step. (a) The scattered impulses of the original simulation for the nodes affected by the perturbation. (b) Reflected impulses of the original simulation to be stored for the evaluation of ${}_k\eta^i$. (c) Adjoint impulses of the perturbed structure. (d) The approximated adjoint impulses to be stored for sensitivity calculations.

$$\Delta \boldsymbol{A}_i = \frac{\boldsymbol{C}(\boldsymbol{x})\Delta \boldsymbol{S}_i}{\Delta t} = \frac{\boldsymbol{C}(\boldsymbol{x})\left[\boldsymbol{S}(\boldsymbol{x}+\Delta \boldsymbol{x}_i) - \boldsymbol{S}(\boldsymbol{x})\right]}{\Delta t}. \tag{3.27}$$

Accordingly

$${}_k\boldsymbol{\eta}^i = \frac{\boldsymbol{C}(\boldsymbol{x})\Delta \boldsymbol{S}_i}{\Delta x_i \Delta t} = \frac{1}{\Delta x_i \Delta t}\boldsymbol{C}(\boldsymbol{x})\left[\boldsymbol{S}(\boldsymbol{x}+\Delta \boldsymbol{x}_i) - \boldsymbol{S}(\boldsymbol{x})\right]{}_k\boldsymbol{V}. \tag{3.28}$$

In implementing (3.28), the incident impulses of the original system are scattered using the temporary scattering matrix, $\Delta \boldsymbol{S}_i$ where its block diagonal matrices are zero everywhere except for the nodes which are directly affected by the perturbation. This results in a considerable memory saving.

Figure 3.2 illustrates the impulses in the original and the adjoint simulations to be stored for sensitivity estimations.

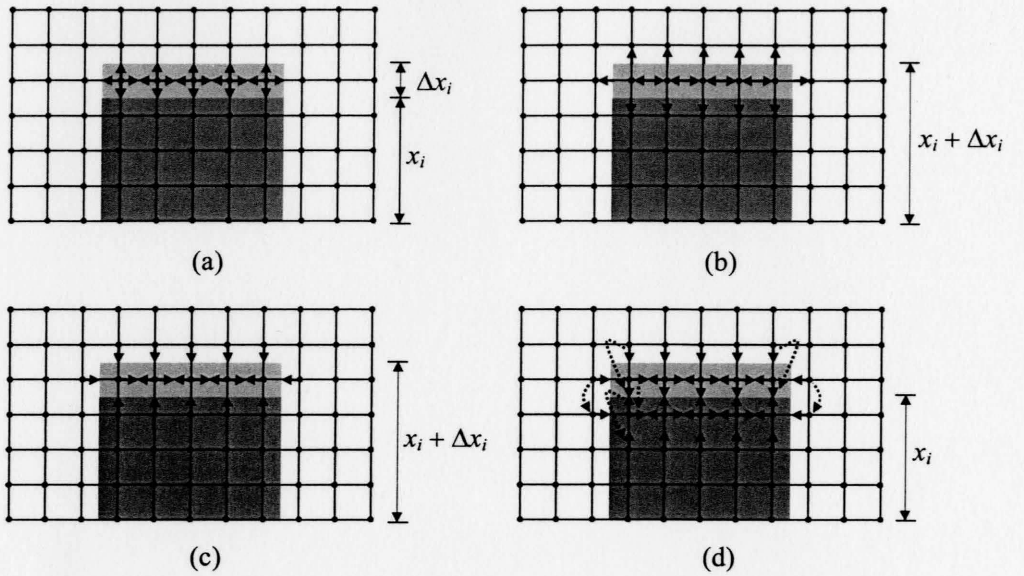

Figure 3.2: Illustration of the impulse storage for the original and the adjoint simulations for a dielectric/magnetic discontinuity at the k^{th} time step. (a) The incident impulses of the perturbed nodes in the original system are scattered using the temporary nodal scattering matrix, $\Delta \boldsymbol{S}^i$ (b) The temporary reflected impulses of the original system are connected to the neighboring nodes, are used to evaluate ${}_k\boldsymbol{\eta}^i$. (c) The associated non-zero adjoint impulses of the perturbed structure. (d) The approximated adjoint impulses to be stored for sensitivity calculations.

A second approach for obtaining the sensitivities with respect to dielectric discontinuities is proposed in [6], where the analytical dependencies of nodal scattering matrices to medium properties are employed. It is shown that the sensitivities of the objective function are derived as

$$\frac{\partial F}{\partial x_i} = \frac{\partial^e F}{\partial x_i} - \Delta t \sum_{n=1}^{l+m} \sum_{k=1}^{N_t} {}_k\boldsymbol{\lambda}^T \frac{\partial \boldsymbol{A}}{\partial \varepsilon_{r,n}} {}_k\boldsymbol{V} \frac{\Delta \varepsilon_{r,n}}{\Delta x_i} \tag{3.29}$$

where $\varepsilon_{r,n}$ is the relative permittivity of the n^{th} node, and the outer summation is carried over all the perturbed nodes.

It is worth mentioning that the sensitivity calculations based on (3.28) and (3.19) is general and can be applied to both dielectric and magnetic discontinuities. The expression (3.29), however, provides acceptable results only if the contrast between the relative permittivity or permeability of the discontinuity and the surrounding medium is not large.

The algorithm of the adjoint-variable method is summarized in the following steps [2]:

Stage 1: *Parameterization*

For each perturbation, Δx_i $i = 1, 2, \ldots, n$, determine the set of link-line indices, L_i for which the associated scattering and connection matrices are perturbed.

Stage 2: *Original System Analysis*

Perform the original TLM simulation, and store the non-zero elements of the vector ${}_k\boldsymbol{\eta}^i$ from (3.20) for all time steps. Also obtain the vector of adjoint excitation defined in (3.17) for the entire simulation time.

Stage 3: *Adjoint System Analysis*

Using the derived adjoint excitations from stage 2, perform the adjoint simulation (3.18). At each time step approximate the adjoint impulses associated with the set of link-lines, L_i $i = 1, 2, \ldots, n$ and store them for all time steps.

Stage 4: *Sensitivity Estimation*

Approximate the objective function sensitivities given in (3.19) for all design parameters.

3.1.2 Adjoint-Variable Method for *S*-Parameter Sensitivities

The adjoint-variable method has been recently extended to include the sensitivity estimation of the *S*-parameters within the time-domain framework [7]. This section provides a review of this algorithm.

Consider an N_p–port network, where the q^{th} port is excited and the rest of the ports are matched. For a given mode υ and frequency ω_0, the $\tilde{S}_{pq}$ parameter is defined as [8]

$$\tilde{S}_{pq} = \sqrt{\frac{Z_q^{(\upsilon)}}{Z_p^{(\upsilon)}}}\frac{\tilde{E}_{pq}^{(\upsilon)}}{\tilde{E}_q^{(\upsilon)}}. \tag{3.30}$$

Here, $Z_\xi^{(\upsilon)}$ $(\xi = p, q)$ is the wave impedance of the ξ^{th} port for mode υ, and

$$\begin{aligned} \tilde{E}_{pq}^{(\upsilon)} &= \int_0^{T_{\max}} \iint_{\Omega_p} E_{q\perp}^{ou}(\boldsymbol{r}', t) e_{p\perp}^{(\upsilon)}(\boldsymbol{r}') ds_p' e^{-j\omega_0 t} dt \\ \tilde{E}_q^{(\upsilon)} &= \int_0^{T_{\max}} \iint_{\Omega_q} E_{q\perp}^{in}(\boldsymbol{r}', t) e_{q\perp}^{(\upsilon)}(\boldsymbol{r}') ds_q' e^{-j\omega_0 t} dt \end{aligned} \tag{3.31}$$

where

$\tilde{E}_{pq}^{(\upsilon)}$ is the spectrum at the p^{th} port, due to the excitation of the q^{th} port,

$\tilde{E}_q^{(\upsilon)}$ is the spectrum at the q^{th} excitation port,

$E_{q\perp}^{ou}$ is the field solution of the outgoing wave at the p^{th} port which is transverse to the propagation direction,

$E_{q\perp}^{in}$ is the field solution of the incoming wave at the q^{th} excitation port, which is transverse to the propagation direction,

$e_{\xi\perp}^{(\upsilon)}$ is the modal distribution at the ξ^{th} port,

ds'_ξ is the surface element at the ξ^{th} port, and

Ω_ξ is the cross-section of the ξ^{th} port.

Assuming that the spectrum of the reference is independent of the design parameters, the sensitivity of $\widetilde{S}_{pq}$, with respect to the i^{th} design parameter is evaluated as

$$\frac{\partial \widetilde{S}_{pq}}{\partial x_i} = \sqrt{\frac{Z_q^{(\upsilon)}}{Z_p^{(\upsilon)}}} \frac{1}{\widetilde{E}_q^{(\upsilon)}} \frac{\partial \widetilde{E}_{pq}^{(\upsilon)}}{\partial x_i}. \tag{3.32}$$

Expression (3.32) indicates that the sensitivity of the $\widetilde{S}_{pq}$ parameter is basically a scaled value of the sensitivity of the output spectrum, $\widetilde{E}_{pq}^{(\upsilon)}$; hence it suffices to concentrate only on estimating the sensitivities of $\widetilde{E}_{pq}^{(\upsilon)}$.

In order to obtain an objective function in the form given by (3.2), the expression of $\widetilde{E}_{pq}^{(\upsilon)}$ is decomposed into its real and imaginary components

$$\begin{aligned} \operatorname{Re}\left[\widetilde{E}_{pq}^{(\upsilon)}\right] &= \int_0^{T_{\max}} \iint_{\Omega_p} E_{q\perp}^{ou}(\boldsymbol{r}',t) e_{p\perp}^{(\upsilon)}(\boldsymbol{r}') \cos(\omega_0 t) ds'_p dt \\ \operatorname{Im}\left[\widetilde{E}_q^{(\upsilon)}\right] &= -\int_0^{T_{\max}} \iint_{\Omega_q} E_{q\perp}^{in}(\boldsymbol{r}',t) e_{q\perp}^{(\upsilon)}(\boldsymbol{r}') \sin(\omega_0 t) ds'_q dt. \end{aligned} \tag{3.33}$$

Accordingly, the objective function kernels are determined as

$$\begin{aligned} \psi_{\text{Re}} &= \iint_{\Omega_p} E_{q\perp}^{ou}(\boldsymbol{r}',t) e_{p\perp}^{(\upsilon)}(\boldsymbol{r}') \cos(\omega_0 t) ds'_p \\ \psi_{\text{Im}} &= -\iint_{\Omega_p} E_{q\perp}^{ou}(\boldsymbol{r}',t) e_{p\perp}^{(\upsilon)}(\boldsymbol{r}') \sin(\omega_0 t) ds'_p \end{aligned} \tag{3.34}$$

which are further discretized to

$$\begin{aligned}\psi_{\mathrm{Re}} &= \Delta s \sum_{j\in\Omega_p} E_{q\perp}^{ou}(\boldsymbol{r}_j,t)e_{p\perp}^{(\upsilon)}(\boldsymbol{r}_j)\cos(\omega_0 t)\\ \psi_{\mathrm{Im}} &= -\Delta s \sum_{j\in\Omega_p} E_{q\perp}^{ou}(\boldsymbol{r}_j,t)e_{p\perp}^{(\upsilon)}(\boldsymbol{r}_j)\sin(\omega_0 t).\end{aligned} \tag{3.35}$$

The excitation of the adjoint simulation is obtained from the kernel of the objective function based on (3.17). In order to derive the required adjoint excitation for the real and imaginary parts of the output spectrum, the expressions given in (3.35) should be reformulated in terms of the incident impulses. This can be done through mapping the field components to the vector of incident impulses

$$E_{q\perp}^{ou}(\boldsymbol{r}'_j,t) = \boldsymbol{a}^T \boldsymbol{V}(\boldsymbol{r}'_j,t) \tag{3.36}$$

where $\boldsymbol{a}$ relates the vector of incident voltage impulses to the field vector. Replacing (3.36) in (3.35), the adjoint excitation at the k^{th} time step, at the node location specified by $\boldsymbol{r}'_j$ is obtained as

$$\begin{aligned}{}_k\lambda_{\mathrm{Re}}^s(\boldsymbol{r}'_j) &= \Delta t\Delta s a e_{p\perp}^{(\upsilon)}(\boldsymbol{r}'_j)\cos(\omega_0 k\Delta t)\\ {}_k\lambda_{\mathrm{Im}}^s(\boldsymbol{r}'_j) &= -\Delta t\Delta s a e_{p\perp}^{(\upsilon)}(\boldsymbol{r}'_j)\sin(\omega_0 k\Delta t).\end{aligned} \tag{3.37}$$

Notice that the real and imaginary parts of the adjoint excitation inherit the same modal distribution as that of the original simulation. Also, the two excitations have only a phase difference of $\pi/2$ which can be translated, in time-domain, into a time-shift

$$T_0(\omega_0) = \mathrm{round}\left(\frac{\pi}{2\omega_0}\right) \tag{3.38}$$

At first glance, it may appear that two separate adjoint simulations with excitations λ_{Re}^s and λ_{Im}^s are required to obtain the vector of adjoint impulses. This, however, can be avoided. In [7] it is shown that the sensitivities of the real and imaginary parts of the output spectrum can be obtained from

$$
\begin{aligned}
\frac{\partial}{\partial x_i}\mathrm{Re}\left[\tilde{E}_{pq}^{(\upsilon)}\right] &\approx -\Delta t\sum_{k=0}^{N_t} {}_k\tilde{\boldsymbol{\lambda}}_{p,\mathrm{Re}}^T({}_k\boldsymbol{\eta}_q^i) \\
\frac{\partial}{\partial x_i}\mathrm{Im}\left[\tilde{E}_{pq}^{(\upsilon)}\right] &\approx -\Delta t\sum_{k=0}^{N_t} {}_k\tilde{\boldsymbol{\lambda}}_{p,\mathrm{Im}}^T({}_k\boldsymbol{\eta}_q^i) \\
&\approx -\Delta t\sum_{k=T_0}^{N_t} {}_k\tilde{\boldsymbol{\lambda}}_{p,\mathrm{Re}}^T({}_k\boldsymbol{\eta}_q^i)
\end{aligned}
\tag{3.39}
$$

where $\tilde{\boldsymbol{\lambda}}_{p,\mathrm{Re}}$ is the vector of the steady-state adjoint impulses obtained from the adjoint simulation with excitation λ_{Re}^s, and T_0 is the shift in the sampling index given by (3.38).

For an N_p–port network, the steps (3.30)-(3.39) should be repeated to evaluate all the *S*-parameters sensitivities, hence N_p adjoint simulations are required to estimate the sensitivities with respect to all design parameters.

The above algorithm is applicable if the sensitivities at a single frequency is desired. However, in wide-band problems where the sensitivity estimations are required over a band of frequencies, the above algorithm becomes inefficient. A novel technique to tackle this problem is proposed in [7]. In the suggested method, instead of using a monochromatic excitation, a wide-band excitation is used which covers the entire range of frequencies of interest. Discrete Fourier Transform (DFT) is then employed to decompose the adjoint impulses into their spectral components. Same excitation is utilized for the original simulation with the only difference in the time-reference. The wide-band excitation is taken as:

$$
\lambda^s(\boldsymbol{r}_j,\tau)=\frac{\boldsymbol{a}}{\|\boldsymbol{a}\|^2}e_{p\perp}(\boldsymbol{r}_j)h(\tau) \quad , \quad j\in\Omega_p \tag{3.40}
$$

where τ is the time variable in the adjoint framework which is backward in time with respect to that of the original system, and $h(\tau)$ represent the time dependence of the

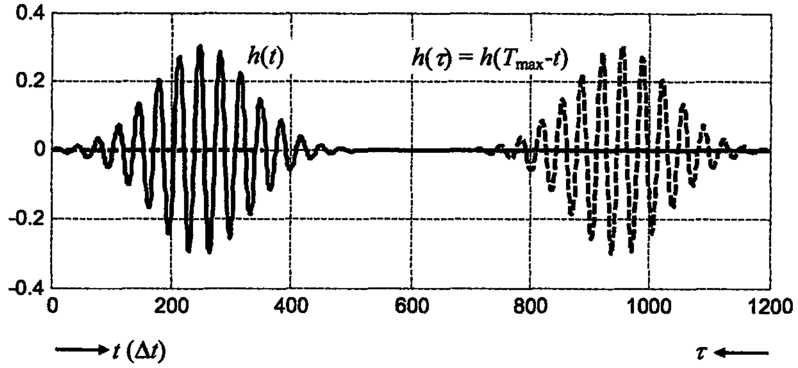

(a)

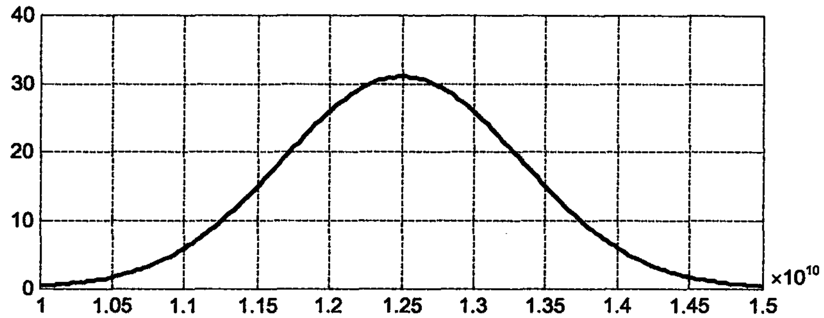

(b)

Figure 3.3: An illustration of a wideband excitation waveform, centered at $f_0 = 12.5$ GHz and covering the frequency range of 10.0 GHz – 15.0 GHz, used for extracting the S-parameter sensitivities. (a) Time dependence in the original and the adjoint system. (b) Fourier transform of the excitations.

wide-band excitation. Figure 3.3 illustrates an example of the excitation waveform in the original and the adjoint simulations.

Once the structure is excited using the wide-band excitation (3.40), the real and imaginary parts of the l^{th} component of the adjoint impulses are extracted as

$$\begin{aligned}
\left({}_k\tilde{\lambda}_{p,\mathrm{Re}}\right)_l &= \Delta t \Delta s |\boldsymbol{a}|^2 \frac{\left|\left({}_k\tilde{\lambda}_p(\omega_m)\right)_l\right|}{\left|\widetilde{H}(\omega_m)\right|} \cos\left[\omega_m n \Delta\tau + \varphi_{p,l} - \varphi_h - \omega_m N_t \Delta\tau\right] \\
\left({}_k\tilde{\lambda}_{p,\mathrm{Im}}\right)_l &= \Delta t \Delta s |\boldsymbol{a}|^2 \frac{\left|\left({}_k\tilde{\lambda}_p(\omega_m)\right)_l\right|}{\left|\widetilde{H}(\omega_m)\right|} \cos\left[\omega_m n \Delta\tau + \varphi_{p,l} - \varphi_h - \omega_m N_t \Delta\tau - \frac{\pi}{2}\right]
\end{aligned} \tag{3.41}$$

where

$\tilde{\lambda}_{p,\mathrm{Re}}$ is the vector of the real part of the predicted steady-state adjoint impulses due to a monochromatic adjoint excitation in the form given in (3.37),

$\tilde{\lambda}_{p,\mathrm{Im}}$ is the vector of the imaginary part of the predicted steady-state adjoint impulses due to a monochromatic adjoint excitation,

$\tilde{\lambda}_{p}$ is the vector of the adjoint impulses obtained from the wideband adjoint excitation given in (3.40),

$\widetilde{H}$ is the Fourier transform of the wideband adjoint excitation defined as

$$\widetilde{H}(\omega_m) = \sum_{n=1}^{N_t} h(\tau_n) e^{-j(m-1)(n-1)\Delta\omega\Delta t}$$

where $\Delta\omega = 2\pi/N_t\Delta t$, and $\Delta\tau = \Delta t$,

$\varphi_{p,l}$ is the phase of the l^{th} component of the vector of adjoint impulses obtained from the wideband adjoint excitation of (3.40)

$$\varphi_{p,l} = \text{Angle}\left\{\left(\tilde{\lambda}_p(\omega_m)\right)_l\right\},$$

and

φ_h is the phase of the wideband adjoint excitation in (3.40) and is defined as

$$\varphi_h = \text{Angle}\left\{\widetilde{H}(\omega_m)\right\}.$$

The predicted adjoint impulses are then employed in (3.39) to estimate the sensitivities of the S-parameters over the range of frequencies of interest.

The AVM approach for the S-parameter sensitivity estimations is summarized in the following steps [7]:

Stage 1: *Parameterization*

For each perturbation, Δx_i $i = 1, 2, \ldots, n$, determine the set of link-line indices, L_i for which the associated scattering and connection matrices are perturbed.

Stage 2: *Original System Analysis*

Perform the original TLM simulation with the wideband excitation in form of (3.40), to obtain the *S*-parameters. Store the non-zero elements of ${}_k\boldsymbol{\eta}^i$ from (3.20) for all time steps.

Stage 3: *Adjoint System Analysis*

Using the wideband excitation in form of (3.40) at the p^{th} port, carry out the backward AVM simulation (3.18), and store the associated adjoint impulses $\tilde{\boldsymbol{\lambda}}_p$ for all link-lines L_i $i = 1, 2, \ldots, n$ for all time steps.

Stage 4: *Sensitivity Estimation*

Repeat for port $q = 1, 2, \ldots, N_p$

Repeat for port $p = 1, 2, \ldots, N_p$

Repeat for parameter $i = 1, 2, \ldots, n$

Repeat for frequency ω_m $m = 1, 2, \ldots, N_\omega$

Obtain the m^{th} spectral component of the vector $\tilde{\boldsymbol{\lambda}}_p$

Evaluate the real and imaginary parts of the predicted steady-state adjoint impulses using (3.41).

Estimate the sensitivities of the output spectrum, $\widetilde{E}_{pq}^{(\upsilon)}$ given in (3.39).

Obtain the *S*-parameter sensitivities through (3.32).

End

End

End

End

3.2 Examples

This chapter is finalized by illustrating the TLM-AVM approach for sensitivity analysis of waveguide structures. Time-domain functions such as the energy function and S-parameters are both considered.

3.2.1 Rectangular Dielectric Discontinuity

The geometry of a rectangular waveguide with a dielectric discontinuity is illustrated in Figure 3.4. The width of the waveguide is a = 30.0 mm. Its length is d = 60.0 mm. The structure is uniformly discretize with TLM cells of size $\Delta l = 1.0$ mm. A narrowband Gaussian-modulated sinusoidal excitation centered at $f_c = 3.0$ GHz with bandwidth $\Delta f = 500$ MHz is used. The excitation has a dominant mode spatial profile. The objective function is taken as a measure of the delivered power to the output port and is expressed as

$$F = \int_{0}^{T_{\max}} \left(\sum_{i=1}^{N_x} E_{y,k}^2 \right) dt \tag{3.42}$$

where E_y is the y component of the electric field, and N_x is the number of nodes along the x-direction at the output port. The vector of design parameter is $\boldsymbol{x} = [\,L \;\; W\,]^T$. The

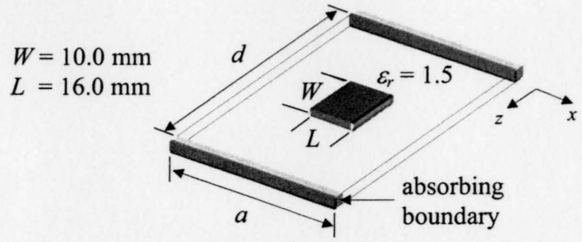

Figure 3.4: Rectangular waveguide with dielectric discontinuity.

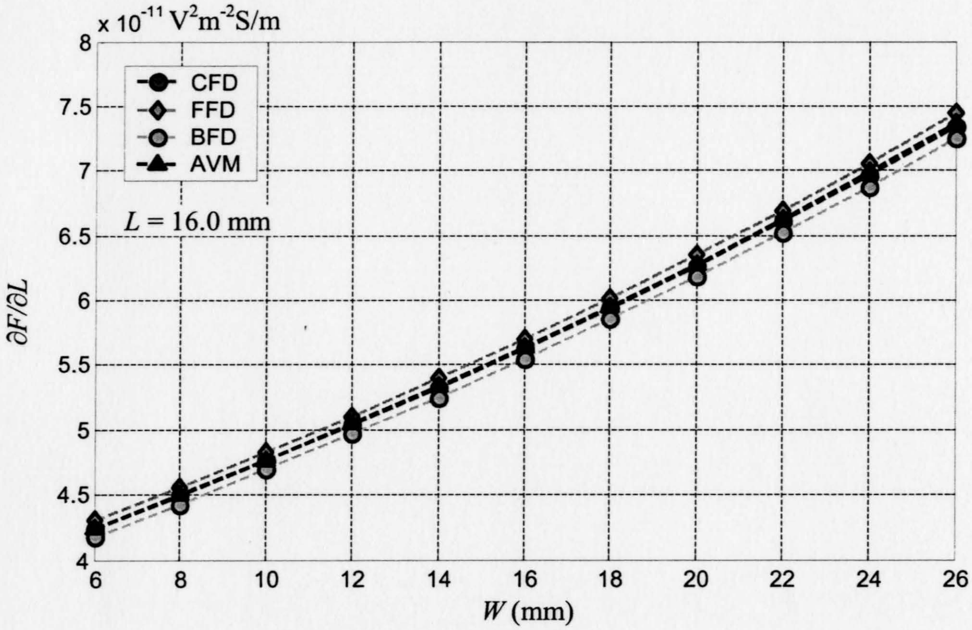

(a)

Figure 3.5: The objective function sensitivity, $\partial F/\partial L$ for different values of W.

simulation is run for 4000 time steps. Figures 3.5 and 3.6 illustrate the objective function sensitivities obtained from the AVM and the finite differences for different values of W.

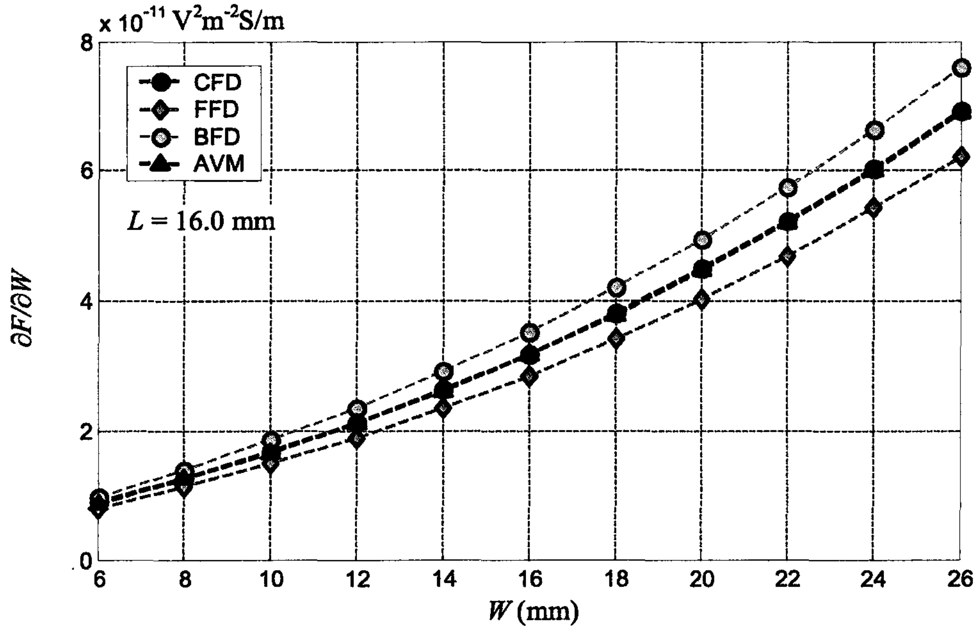

(b)

Figure 3.6: The objective function sensitivity, $\partial F/\partial W$ for different values of W.

As can be observed, the results obtained from the AVM and the finite differences have excellent match. While the forward/backward and central finite differences estimate the sensitivities using 3 and 5 TLM simulations, respectively, the AVM extracts the same information using only two simulations.

3.2.1 Double-Resonator Filter

The geometry of the double-resonator waveguide filter is shown in Figure 3.7. The AVM approach is used to estimate the sensitivities of the reflections $\tilde{S}_{11}$ and $\tilde{S}_{21}$ with respect to the physical dimensions of the metallic discontinuities. The structure is discretized with uniform cells of size $\Delta l = 1.0$ mm. A wideband Gaussian modulated excitation centered at $f_c = 4.0$ GHz with the spectrum range from 3.0 GHz to 5.0 GHz,

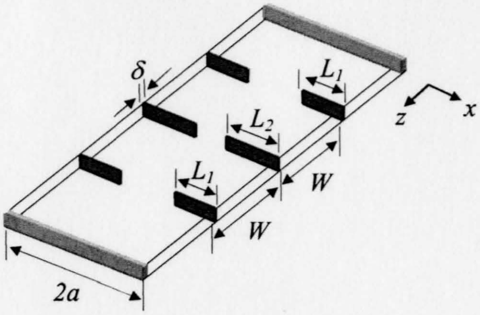

(a)

a	30.0
δ	1.0
W	30.0
L_1	18.0
L_2	19.0
all dimensions in mm	

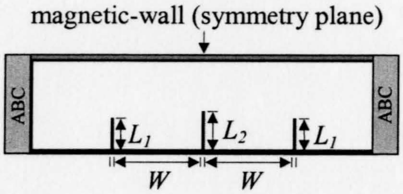

(b)

Figure 3.7: Double-resonator waveguide filter. (a) 3D view. (b) The cross section of the filter in the *xz*-plane with employed symmetry and Johns matrix absorbing boundaries at the input and output ports.

is employed. The excitation has TE_{10} mode spatial profile. Symmetry is utilized to simulate only half of the structure. The filter is terminated at the input and output ports by modal Johns' matrix boundaries with $N_t = 6000$ time steps. The vector of design parameters is taken as $\boldsymbol{x} = [\, L_1 \;\; L_2]^T$. Figure 3.8 illustrates the *S*-parameters of the filter. The sensitivities of the real and imaginary parts of $\tilde{S}_{11}$ and $\tilde{S}_{21}$ obtained from the adjoint-variable method and the central finite differences over a frequency band are shown in Figures 3.9–3.12. The results indicate good match between the two approaches. While the central differences provide the sensitivities using 7 TLM simulations, the AVM extracts the same information using only two simulations.

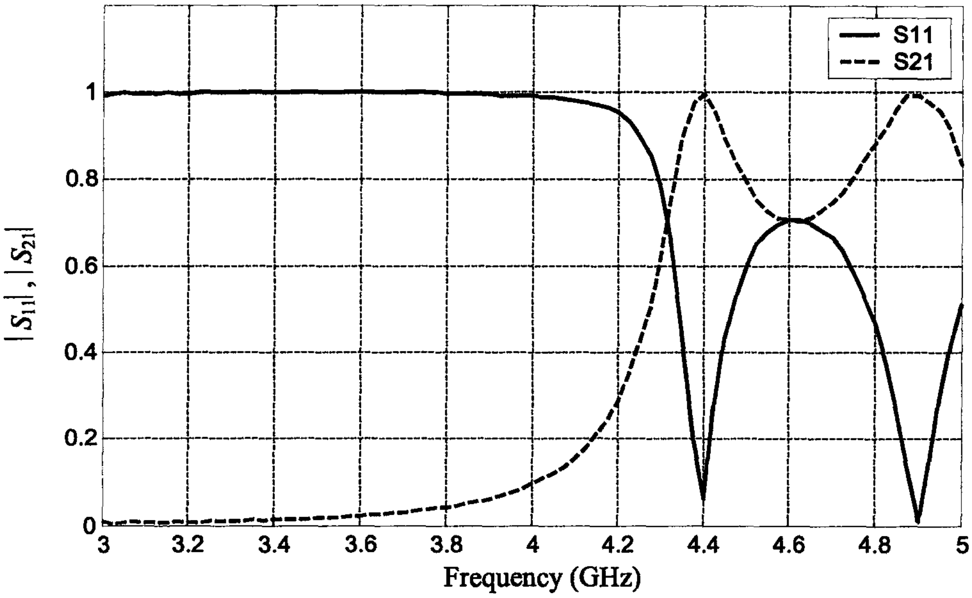

(a)

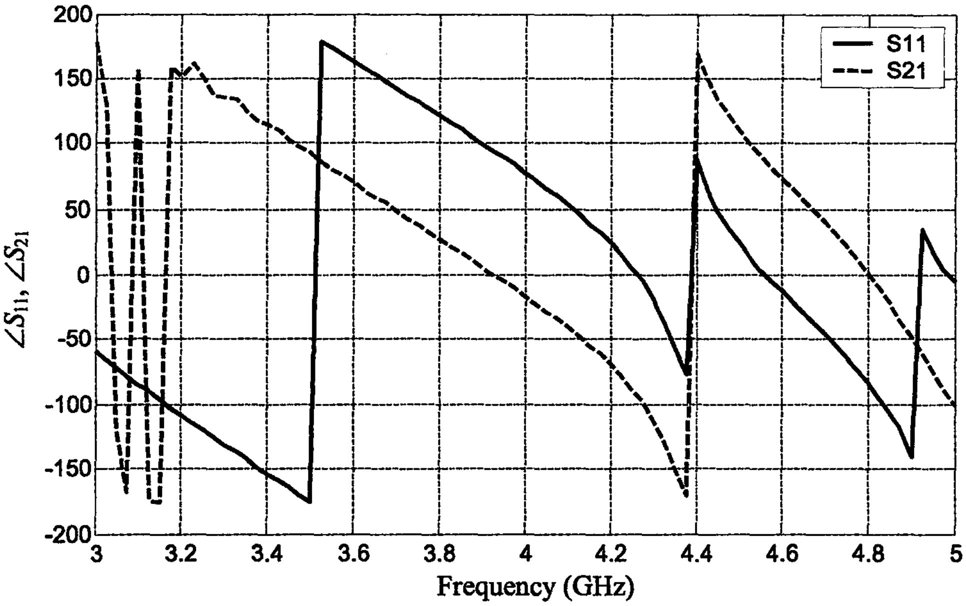

(b)

Figure 3.8: The S-parameters of the double-resonator waveguide filter. (a) $|S_{11}|,|S_{21}|$. (b) $\angle S_{11}, \angle S_{21}$.

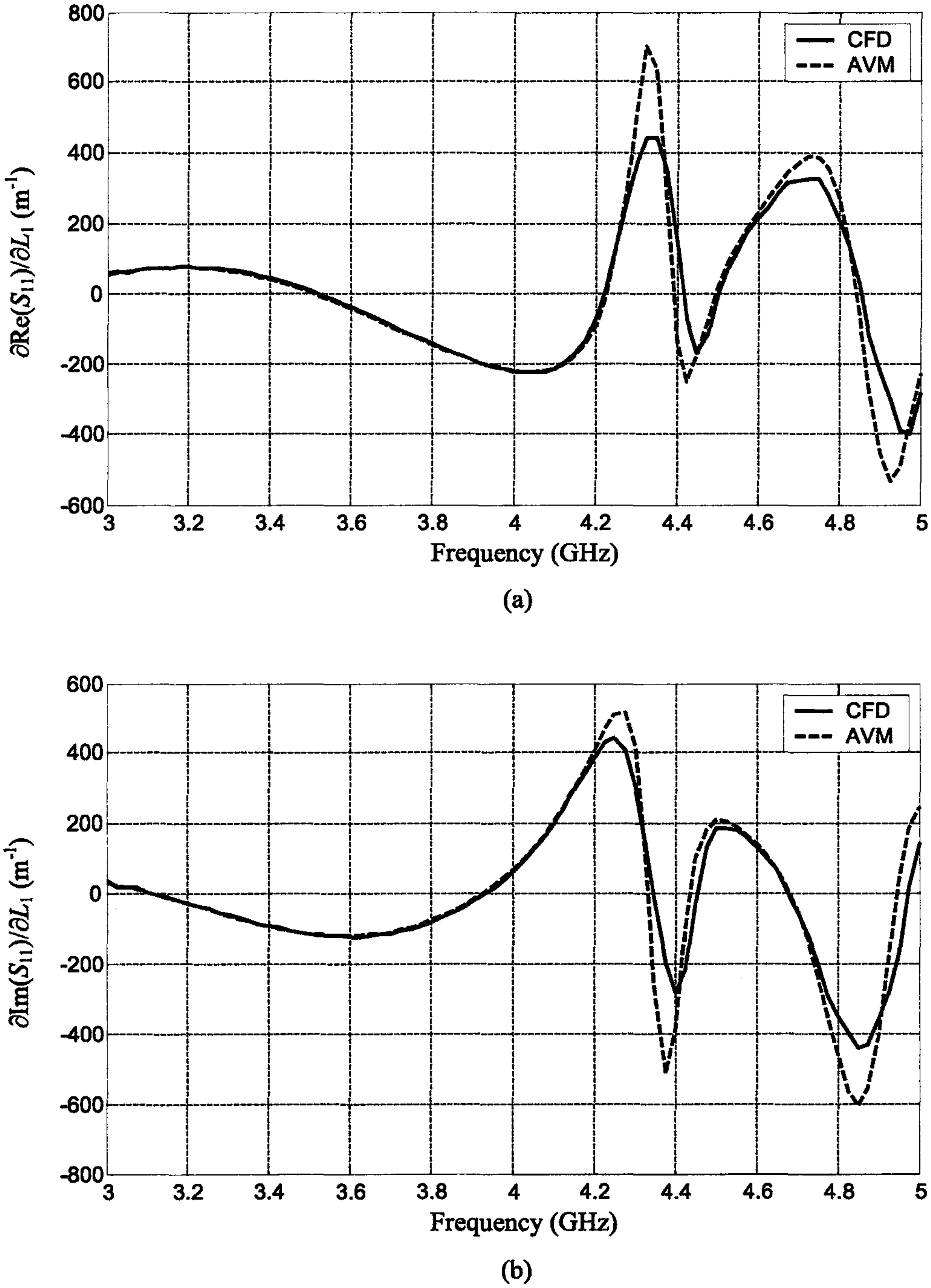

Figure 3.9: Sensitivities of the real and imaginary parts of S_{11} with respect to L_1.

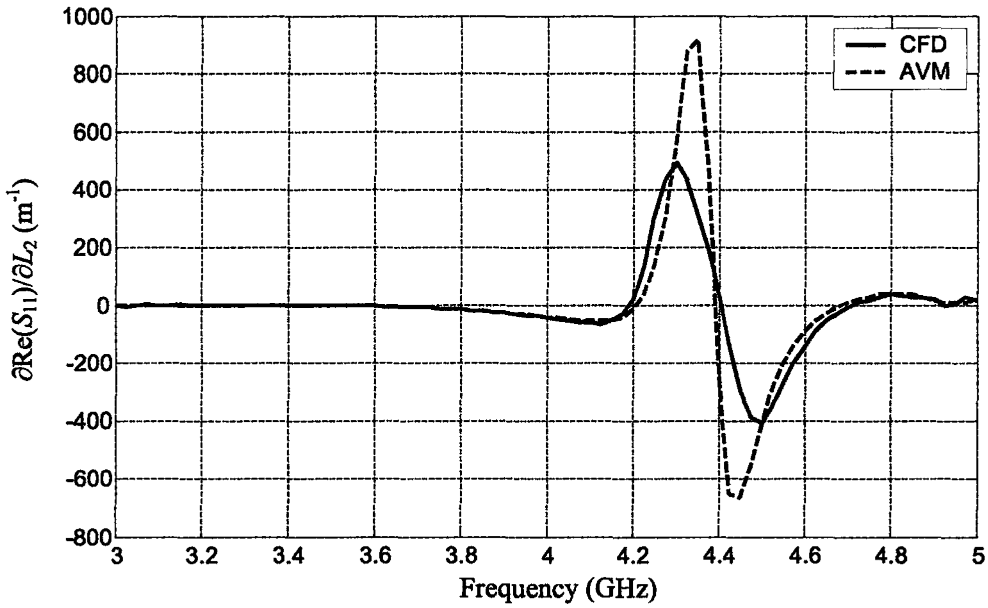

(a)

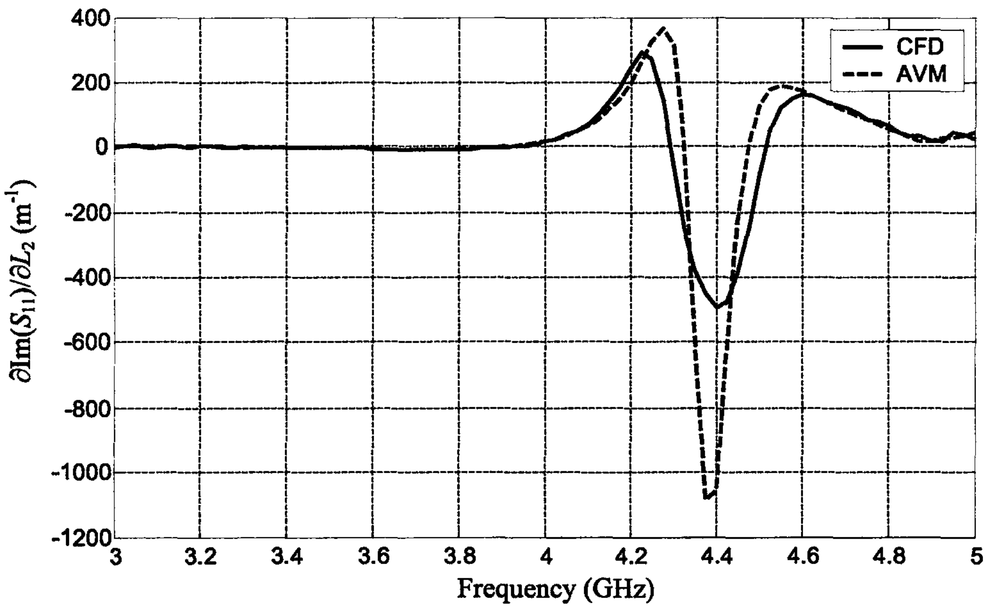

(b)

Figure 3.10: Sensitivities of the real and imaginary parts of S_{11} with respect to L_2.

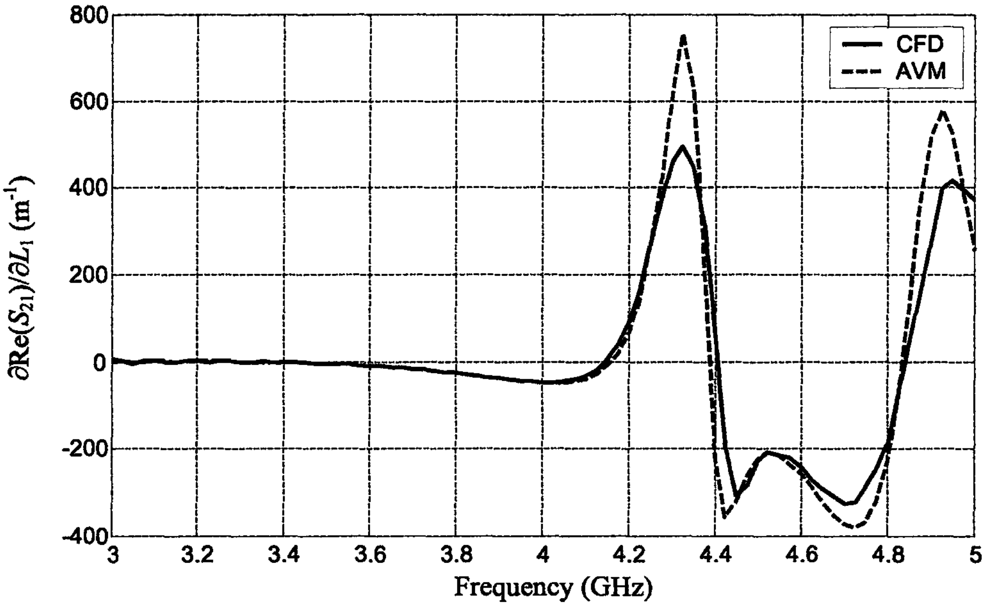

(a)

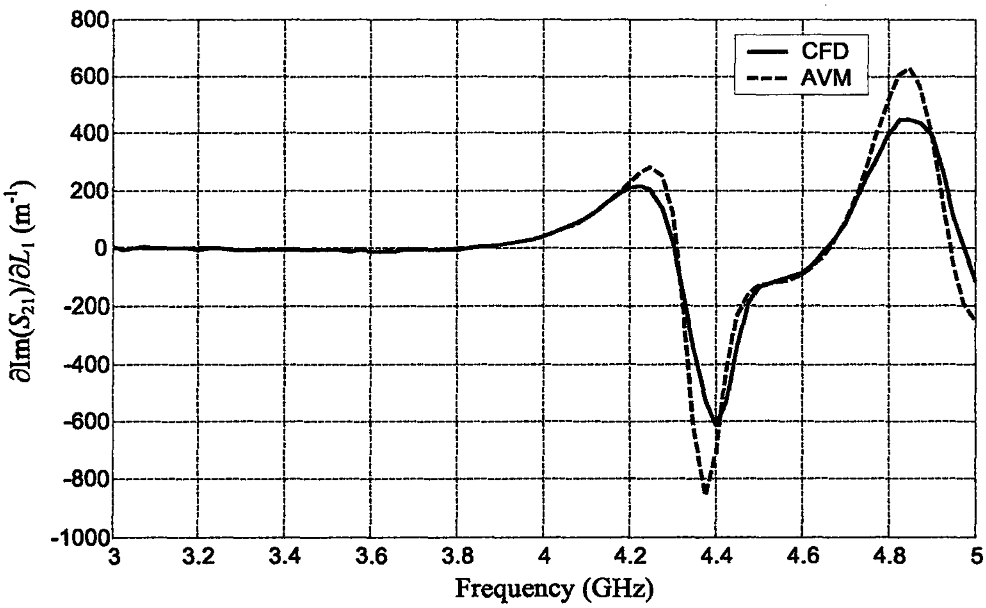

(b)

Figure 3.11: Sensitivities of the real and imaginary parts of S_{21} with respect to L_1.

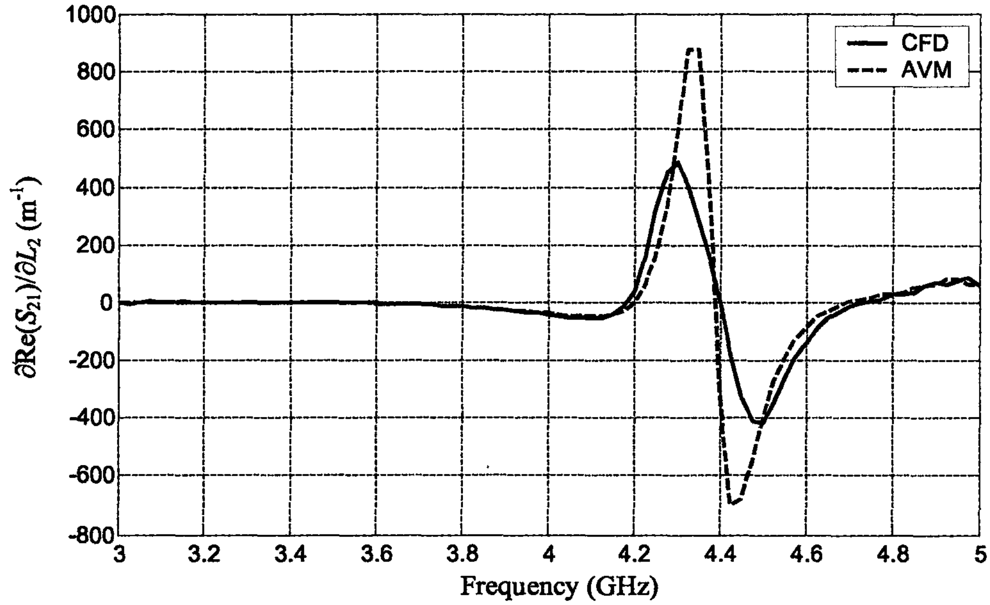

(a)

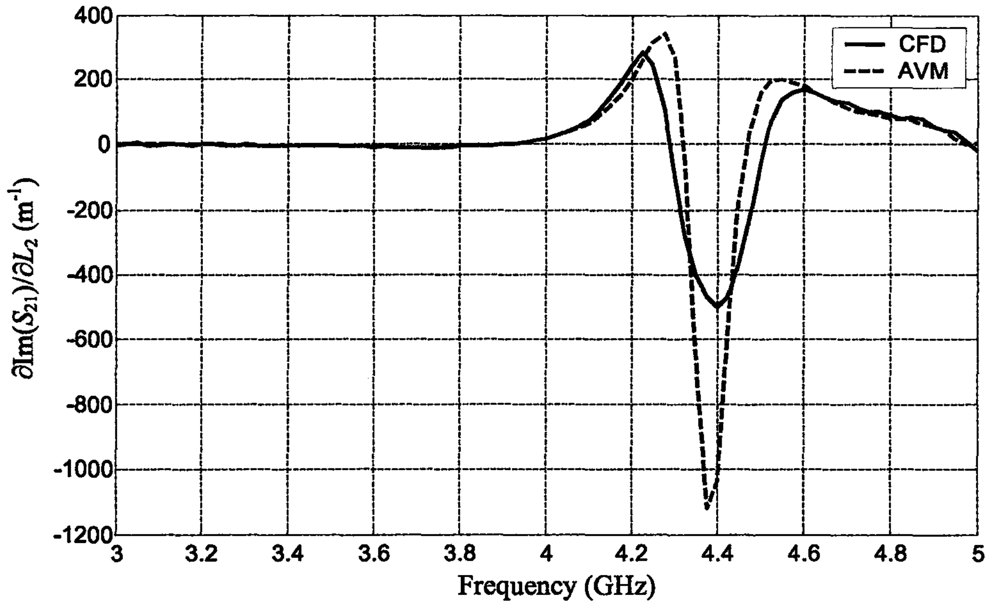

(b)

Figure 3.12: Sensitivities of the real and imaginary parts of S_{21} with respect to L_2.

REFERENCES

[1] N.K. Georgieva, S. Glavic, M.H. Bakr and J.W. Bandler, "Feasible adjoint sensitivity technique for EM design optimization," *IEEE Trans. Microwave Theory Tech.*, vol. 50, pp. 2751-2758 , Dec. 2002.

[2] M.H. Bakr and N.K. Nikolova, "An adjoint variable method for time domain TLM with fixed structured grids," *IEEE Trans. Microwave Theory Tech.*, vol. 52, Feb. 2004, pp. 554-559.

[3] M.H. Bakr and N.K. Nikolova, "An adjoint variable method for time domain TLM with wideband Johns matrix boundaries," *IEEE Trans. Microwave Theory Tech.*, vol. 52, Feb.2004, pp. 678-685.

[4] Y.S. Chung, C. Cheon, I.H. Park and S.Y. Hahn, "Optimal design method for microwave device using time domain method and design sensitivity analysis-part II: FDTD case,"*IEEE Trans. Magnetics.*, vol. 37, pp. 3255-3259, Sep. 2001.

[5] E.J. Haug, K.K. Choi and V. Komkov, *Design Sensitivity Analysis of Structural Systems.*Orlando, Florida: Academic Press Inc., 1986.

[6] P.A.W. Basl, M.H. Bakr and N.K. Nikolova, "Efficient estimation of sensitivities in TLM with dielectric discontinuities," *Microwave and Wireless Components Letters*, vol 15, No. 2, February 2005, pp. 89-91.

[7] M.H. Bakr and N.K. Nikolova, "Efficient Estimation of Adjoint-Variable *S*-Parameter Sensitivities with Time Domain TLM," *Int. J. of Numerical Modeling: Electronic Networks, Devices and Fields,* vol. 18, pp. 171-187, Mar. 2005.

[8] N.K. Nikolova, Ying Li, Yan Li, and M.H. Bakr, "Sensitivity analysis of scattering parameters with electromagnetic time-domain simulators," *IEEE Trans. Microwave Theory Tech.,* to be published.

[9] M.H. Bakr and N.K. Nikolova, "An adjoint variable method for frequency domain TLM problems with conducting boundaries," *IEEE Microwave and Wireless Components Letters*, vol. 13, pp. 408-410, Nov. 2003.

[10] N.K. Nikolova, H.W. Tam, and M.H. Bakr, "Sensitivity analysis with the FDTD method on structured grids," *IEEE Trans. Microwave Theory Tech.*, vol. 52, April 2004, pp. 1207-1216.

[11] A.D. Belegundu and T.R. Chandrupatla, *Optimization Concepts and Applications in Engineering*. Upper Saddle River, NJ: Prentice-Hall Inc., 1999.

[12] H. Akel and J.P. Webb, "Design sensitivities for scattering-matrix calculation with tetrahedral edge elements," *IEEE Trans. Magnetics*, vol. 36, pp. 1043-1046, July 2000.

[13] W.J.R. Hoefer, "The transmission-line matrix method-theory and applications," *IEEE Trans. Microwave Theory Tech.*, vol. MTT-33, pp. 882-893, Oct. 1985.

[14] C. Eswarappa, G.I. Costache, W.J.R. Hoefer, "Transmission line matrix modeling of dispersive wide-band absorbing boundaries with time-domain diakoptics for S-parameter extraction," *IEEE Trans. Microwave Theory Tech.*, vol. 38, pp. 379-386, April 1990.

[15] C. Christopoulos, *The Transmission-Line Modeling Method TLM.* New York, NY : IEEE Press, 1995.

[16] M. Forest and W.J.R. Hoefer, "A novel synthesis technique for conducting scatterers using TLM time reversal," *IEEE Trans. Microwave Theory Tech.*, vol. 43, pp. 1371-1378, June 1995.

[17] D.G. Swanson, Jr., and W.J.R. Hoefer, *Microwave Circuit Modeling Using Electromagnetic Field Simulation.* Norwood, MA: Artech House, 2003.

[18] P.B. Johns, "A symmetric condensed node for the TLM method," *IEEE Trans. Microwave Theory Tech.*, vol. MTT-35, pp. 370-377, April 1987.

Chapter 4

A TRANSFORMED TLM FORMULATION FOR ADJOINT-VARIABLE BASED SENSITIVITY ANALYSIS

In the previous chapter, an adjoint system was developed for the efficient sensitivity estimation of TLM problems [1]-[2]. It was explained that the analyses of the original and the adjoint systems are obtained from the unperturbed structure. However, the two systems are different in the following:

- The original TLM simulation runs forward in time, while the AVM simulation runs backward, starting at the simulation time, T_{max}.
- The system scattering and connection matrices of the adjoint problem are the transpose of those of the original problem.
- The order of the scattering and the connection steps in the adjoint problem is reversed.

The above differences imply that, in general the TLM-AVM framework requires two distinct simulation engines for analyzing each problem. This, in turn limits the employment of the available commercial-solvers with the adjoint variable method.

In this chapter, a novel approach is presented which unifies the mathematical form of the original and the adjoint problems into an identical TLM expression [3]. The unique formulation suggests using a single TLM engine with the only difference in the excitation.

4.1 The Transformed TLM-AVM Formulation

In TLM, the nodal scattering matrix is generally asymmetric. In the proposed formulation, a matrix transformation is utilized to split the nodal scattering matrices of all nodes into two matrices

$$\boldsymbol{S}^m = \boldsymbol{S}'^m \boldsymbol{T}^m \tag{4.1}$$

where $\boldsymbol{S}^m$ is the nodal asymmetric scattering matrix of the m^{th} node, $\boldsymbol{S}'^m$ is the new nodal symmetrical scattering matrix, and $\boldsymbol{T}^m$ is the transforming diagonal matrix. For the lossless 2–D shunt node [4] (see Figure 2.2), the mathematical forms of $\boldsymbol{S}'^m$ and $\boldsymbol{T}^m$ are given as

$$\boldsymbol{S}'^m = \frac{1}{Y}\begin{bmatrix} 2-Y & 2 & 2 & 2 & 2 \\ 2 & 2-Y & 2 & 2 & 2 \\ 2 & 2 & 2-Y & 2 & 2 \\ 2 & 2 & 2 & 2-Y & 2 \\ 2 & 2 & 2 & 2 & 2-\dfrac{Y}{Y_0} \end{bmatrix}$$

$$\boldsymbol{T}^m = \begin{bmatrix} \boldsymbol{I}_4 & \\ & Y_0 \end{bmatrix} \tag{4.2}$$

where Y_0 is the normalized admittance of the dielectric stub of the m^{th} node, $Y = 4 + Y_0$, and $\boldsymbol{I}_4 \in \Re^{4\times4}$ is the unity matrix. The matrix $\boldsymbol{T}^m$ scales the incident impulse of the dielectric-stub (fifth link) by the normalized admittance of the same stub.

Similarly, for the lossless 3–D TLM problems with symmetrical condensed nodes [5], the asymmetric nodal scattering matrix can be decomposed into

$$\boldsymbol{S}'^m = \begin{bmatrix} \boldsymbol{S}_{sym}^m & \boldsymbol{B}^m \\ \boldsymbol{B}^{m^T} & \boldsymbol{D}^m \end{bmatrix}$$

$$\boldsymbol{T}^m = \begin{bmatrix} \boldsymbol{I}_{12} & & & & & & & \\ & Y_x & & & & 0 & & \\ & & Y_y & & & & & \\ & & & Y_z & & & & \\ & & & & 1/Z_x & & & \\ & 0 & & & & 1/Z_y & & \\ & & & & & & 1/Z_z \end{bmatrix} \tag{4.3}$$

where $Y_x, Y_y, Y_z / Z_x, Z_y$ and Z_z are the normalized admittances/impedances of the capacitive/inductive stubs of the m^{th} node in the x, y and z directions, respectively, and $\boldsymbol{S}_{sym}^m \in \Re^{12\times12}$ is the scattering matrix of the symmetrical condensed node without capacitive and inductive stubs. The matrices $\boldsymbol{B}^m \in \Re^{12\times6}$ and $\boldsymbol{D}^m \in \Re^{6\times6}$ are given by

$$
\boldsymbol{B}^m = \begin{bmatrix}
e & & & & & f \\
e & & & & -f & \\
& e & & & & -f \\
& e & & f & & \\
& & e & -f & & \\
& & e & & f & \\
& & e & f & & \\
& e & & -f & & \\
e & & & & f & \\
& & e & & -f & \\
& e & & & & f \\
e & & & & & -f
\end{bmatrix}
$$

$$
\boldsymbol{D}^m = \begin{bmatrix}
h/Y_x & & & & & \\
& h/Y_y & & & 0 & \\
& & h/Y_z & & & \\
& & & jZ_x & & \\
& 0 & & & jZ_y & \\
& & & & & jZ_z
\end{bmatrix} \tag{4.4}
$$

where e, f, h and j are functions of the characteristic impedances and admittances of the different stubs of the m^{th} node [6].

Assume that the computational domain is uniformly discretized into a total of N nodes with the total number of associated TLM links, N_L. As was explained earlier in chapters 2 and 3, a single TLM step of the original and the adjoint problem, at the k^{th} time step are respectively given by

$$
{}_{k+1}\boldsymbol{V} = \boldsymbol{C}(\boldsymbol{x})\boldsymbol{S}(\boldsymbol{x})\,{}_k\boldsymbol{V} + {}_k\boldsymbol{V}^s \quad , \quad \boldsymbol{V}(0) = \boldsymbol{0}, \tag{4.5}
$$

and

$$
{}_{k-1}\boldsymbol{\lambda} = \boldsymbol{S}^T(\boldsymbol{x})\boldsymbol{C}^T(\boldsymbol{x})\,{}_k\boldsymbol{\lambda} - {}_k\boldsymbol{\lambda}^s \quad , \quad \boldsymbol{\lambda}(T_{\max}) = \boldsymbol{0}. \tag{4.6}
$$

The new formulation exploits the matrix decomposition (4.1). Define $\boldsymbol{S}' \in \Re^{N_L \times N_L}$ and $\boldsymbol{T} \in \Re^{N_L \times N_L}$ as the new block diagonal matrices whose m^{th} blocks are $\boldsymbol{S}'^m$ and $\boldsymbol{T}^m$, respectively. Using the transformation (4.1), and multiplying both sides of (4.5) by the matrix $\boldsymbol{T}$, the original TLM simulation can be written as

$$ {}_{k+1}\boldsymbol{V}' = \boldsymbol{C}'(\boldsymbol{x})\boldsymbol{S}'(\boldsymbol{x})\,{}_{k}\boldsymbol{V}' + {}_{k}\boldsymbol{V}'^{s} \quad , \quad \boldsymbol{V}'(0) = \boldsymbol{0} \tag{4.7} $$

where

${}_{k}\boldsymbol{V}' = \boldsymbol{T}\,{}_{k}\boldsymbol{V} \in \Re^{N_L}$	is the transformed vector of incident impulses at the k^{th} time step,
$\boldsymbol{C}' = \boldsymbol{TC} \in \Re^{N_L \times N_L}$	is the new connection matrix, and
${}_{k}\boldsymbol{V}'^{s} = \boldsymbol{T}\,{}_{k}\boldsymbol{V}^{s} \in \Re^{N_L}$	is the transformed vector of original excitation at the k^{th} time step.

The TLM expression (4.7) is the transformed original TLM simulation.

For the adjoint simulation, we multiply both sides of (4.6) by $\boldsymbol{S}^T$ and exploit the lossless domain property $\boldsymbol{S}^T\boldsymbol{S}^T = \boldsymbol{S}^T(\boldsymbol{S}^T)^{-1} = \boldsymbol{I}$ where $\boldsymbol{I} \in \Re^{N_L \times N_L}$ is the identity matrix. Expression (4.6) can then be rearranged as

$$ \boldsymbol{S}^T(\boldsymbol{x})\,{}_{k-1}\boldsymbol{\lambda} = \boldsymbol{C}^T(\boldsymbol{x})\left[\boldsymbol{S}^T(\boldsymbol{x})\boldsymbol{S}^T(\boldsymbol{x})\right]{}_{k}\boldsymbol{\lambda} - \boldsymbol{S}^T(\boldsymbol{x})\,{}_{k}\boldsymbol{\lambda}^{s}. \tag{4.8} $$

Using $\boldsymbol{S}^T = \boldsymbol{TS}'$, and taking into account that the connection matrix $\boldsymbol{C}$ is symmetric, (4.8) can be rewritten as

$$ {}_{k-1}\boldsymbol{\lambda}' = \boldsymbol{C}'(\boldsymbol{x})\boldsymbol{S}'(\boldsymbol{x})\,{}_{k}\boldsymbol{\lambda}' - {}_{k}\boldsymbol{\lambda}'^{s} \quad , \quad \boldsymbol{\lambda}'(T_s) = \boldsymbol{0} \tag{4.9} $$

where ${}_{k}\boldsymbol{\lambda}' = \boldsymbol{TS}'\,{}_{k}\boldsymbol{\lambda} \in \Re^{N_L}$ and ${}_{k}\boldsymbol{\lambda}'^{s} = \boldsymbol{TS}'\,{}_{k}\boldsymbol{\lambda}^{s} \in \Re^{N_L}$ are the k^{th} time step transformed vectors of adjoint impulses and adjoint excitation, respectively. In (4.9) the commutative property of the matrices $\boldsymbol{C}$ and $\boldsymbol{T}$ is exploited.

Expressions (4.7) and (4.9) are the transformed original and adjoint simulations, respectively. They have an identical mathematical form and they differ only in their excitation. A single TLM simulation engine can be used for both simulations. For a TLM problem with N design parameters, the transformed formulation estimates the sensitivity of the objective function using only one adjoint simulation while the corresponding accurate central finite differences approximation requires $2N$ simulations.

4.2 Examples

4.2.1 Metallic Discontinuity in Rectangular Waveguide

The geometry of a rectangular waveguide with a metallic discontinuity is illustrated in Figure 4.1. The waveguide is filled with polystyrene ($\varepsilon_r = 2.56$). The vector of design parameters is $\boldsymbol{x} = [H \quad W \quad L]^T$. The structure is uniformly discretized with cell size $\Delta l = 1$ mm. A narrow band Gaussian modulated sinusoid centered at $f_c = 3.5$ GHz is used to excite the structure with dominant mode spatial profile. The objective function is taken as

$$F(\boldsymbol{x}, \boldsymbol{V}) = \int_0^{T_s} \left(\sum_{i=1}^{N_x} \sum_{j=1}^{N_y} E_{y,k}^2(i, j, N_z) \right) dt \tag{4.10}$$

where N_x, N_y and N_z are the number of cells in the x, y and z directions, respectively. Figures 4.2–4.4 illustrate the sensitivities of (4.10) obtained using both the new AVM formulation and the central-finite differences. The results show good match between both approaches. Note that in Figure 4.4, the results almost completely coincide and their

a	40.0
b	20.0
c	50.0
all dimensions in mm	

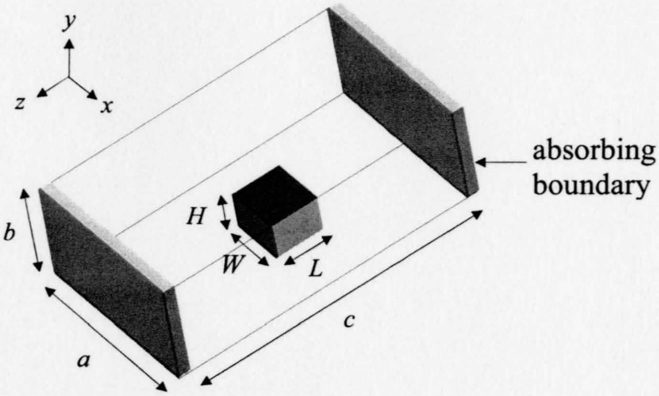

Figure 4.1: Rectangular waveguide with a metallic discontinuity.

difference can hardly be observed. The AVM approach requires only one extra 3–D simulation while the central difference approximation requires 6 additional simulations.

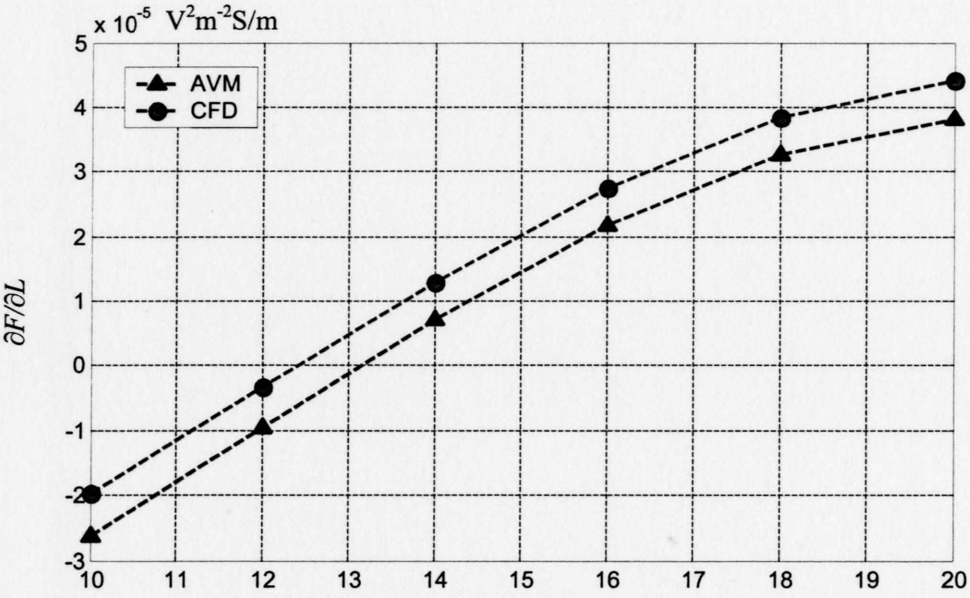

Figure 4.2: Sensitivities of the objective function with respect to the dimensions of the metallic discontinuity for $H = 5\Delta l$ and $W = 10\Delta l$, over a sweep of L; $\partial F/\partial L$ obtained using AVM (-•-) and using CDs (-▲-).

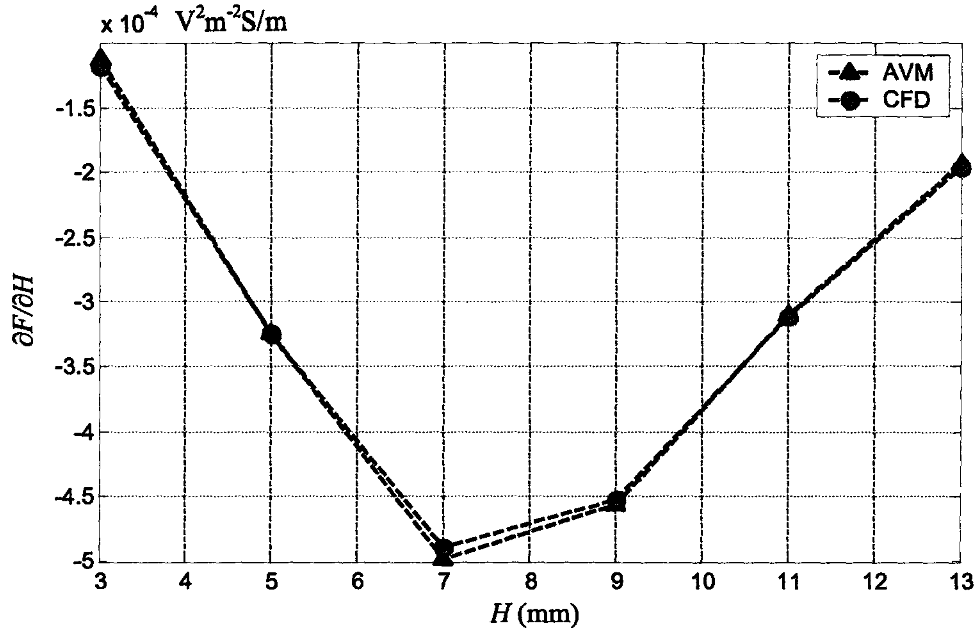

Figure 4.3: Sensitivities of the objective function with respect to the dimensions of the metallic discontinuity for $L = 20\Delta l$ and $W = 10\Delta l$, over a sweep of H; $\partial F/\partial H$ obtained using AVM (-•-) and using CDs (-▲-).

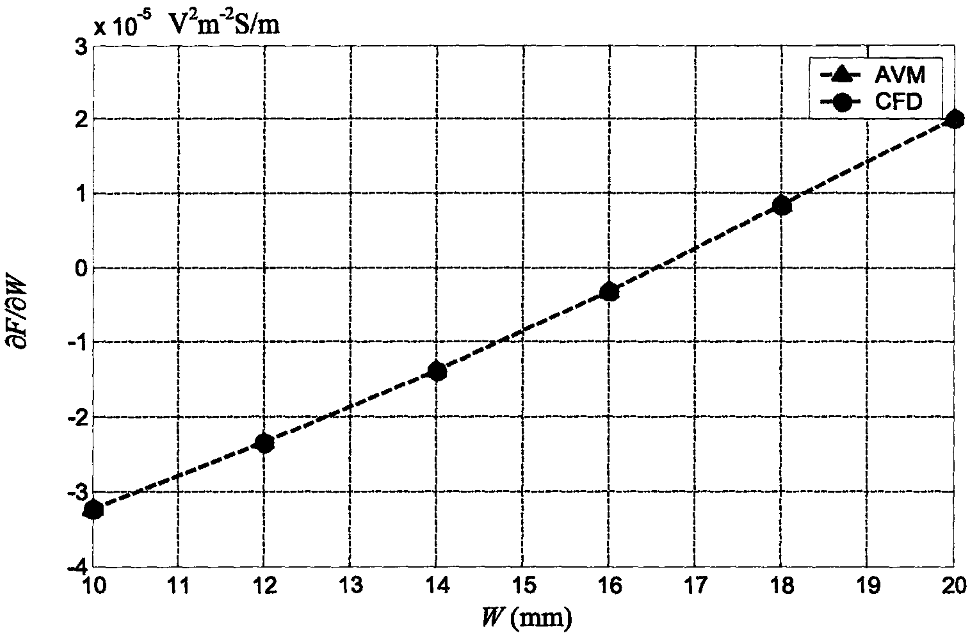

Figure 4.4: Sensitivities of the objective function with respect to the dimensions of the metallic discontinuity for $H = 5\Delta l$ and $L = 10\Delta l$, over a sweep of W; $\partial F/\partial W$ obtained using AVM (-•-) and using CDs (-▲-).

4.2.2 Single-Resonator Filter

The new AVM formulation is applied to estimate the sensitivities of a single-resonator filter (see Figure 4.5) filled with polystyrene ($\varepsilon_r = 2.56$). A uniform square TLM cell of dimension $\Delta l = 1.0$ mm is utilized. The vector of design parameters is $\boldsymbol{x} = [D \quad W]^T$. The objective function is defined as a measure of the power delivered to the output port

$$F(\boldsymbol{x}, \boldsymbol{V}) = \Delta t \sum_{k=1}^{N_t} \sum_{i=1}^{N_x} V_{4,k}^2(i, N_z) \tag{4.11}$$

where $V_{4,k}$ is the value of the incident voltage at the forth link at the k^{th} time step. The waveguide is excited at the input port with a Gaussian-modulated sinusoidal signal centered at frequency $f_0 = 3.0$ GHz. The simulation runs for 4000 time steps. The sensitivities of (4.11) are estimated using the modified AVM formulation and the forward/backward and central-differences (CDs), as illustrated in Figures 4.6-4.8. Good matches are obtained in all cases, however the best match is derived between the AVM and the central finite differences, which implies the efficiency of the adjoint variable method in terms of the algorithm's efficiency.

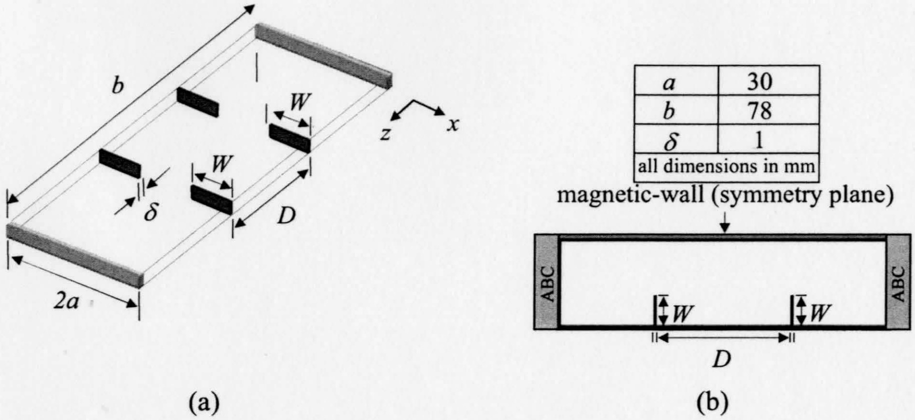

Figure 4.5: Single-resonator waveguide filter. (a) 3D view. (b) The cross section of the filter in the *xz*-plane with employed symmetry and single-reflection absorbing boundaries at the input and output ports.

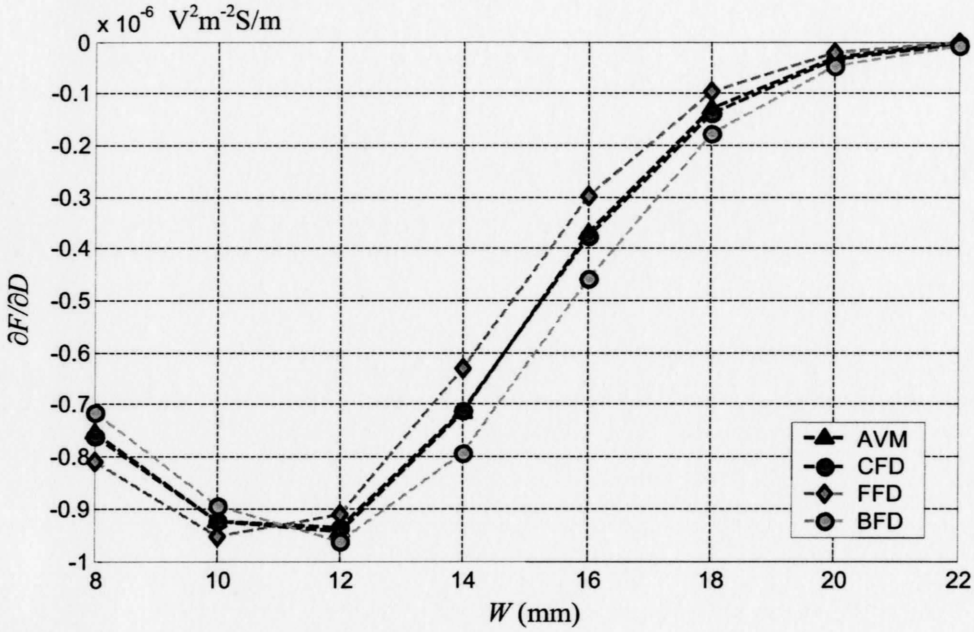

Figure 4.6: Sensitivities of the objective function, $\partial F/\partial W$ at $D = 36\Delta l$ over different values of W.

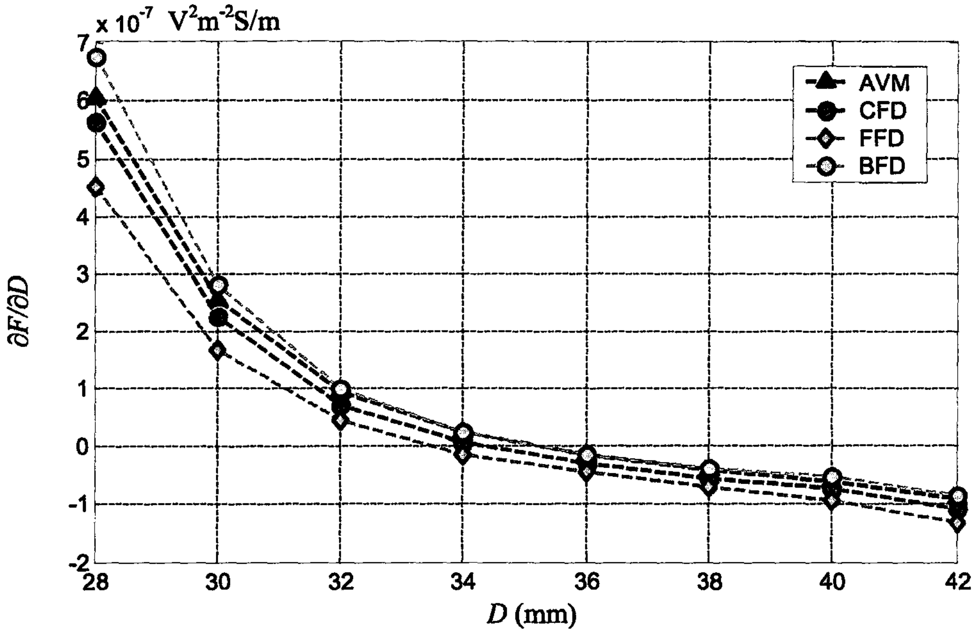

Figure 4.7: Sensitivities of the objective function, $\partial F/\partial D$ at $W = 16\Delta l$ over different values of D.

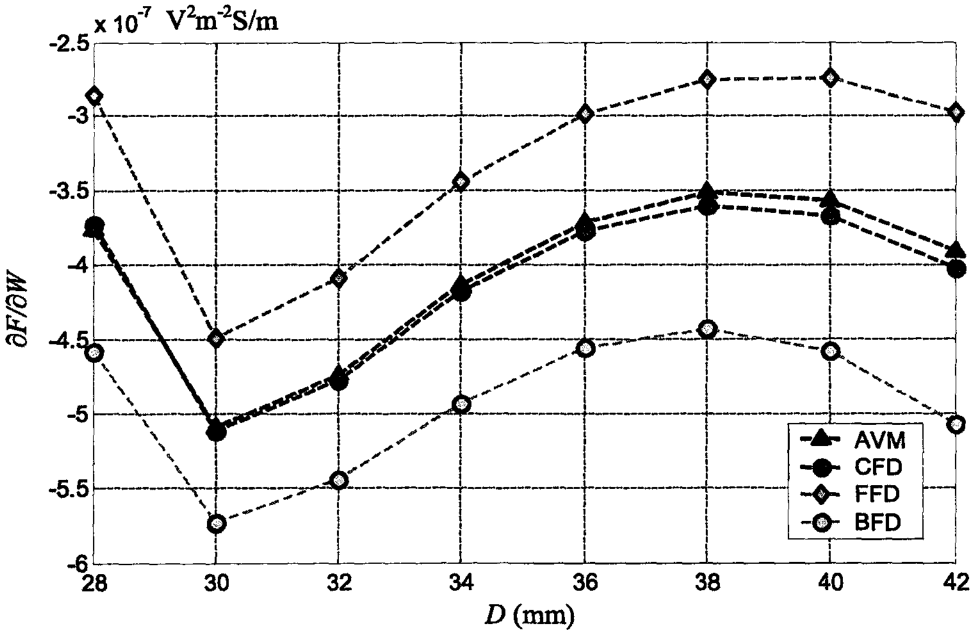

Figure 4.8: Sensitivities of the objective function, $\partial F/\partial W$ at $W = 16\Delta l$ over different values of D.

REFERENCES

[1] M.H. Bakr and N.K. Nikolova, "An adjoint variable method for time domain TLM with fixed structured grids," *IEEE Trans. Microwave Theory Tech.*, vol 52, pp. 554-559, Feb. 2004.

[2] M.H. Bakr and N.K. Nikolova, "An adjoint variable method for time domain TLM with wideband Johns matrix boundaries," *IEEE Trans. Microwave Theory Tech.*, vol 52, pp. 678-685, Feb. 2004.

[3] P. Abolghasem, M.H. Bakr, W. J. R. Hoefer, and P. M. So, "A transformed TLM formulation for adjoint-variable based sensitivity analysis," *Microwave and Wireless Components Letters*, vol. 15, No. 11, pp. 817-819, November 2005.

[4] W.J.R. Hoefer, "The transmission-line matrix method-Theory and applications," *IEEE Trans. Microwave Theory Tech.*, vol. MTT-33, pp. 882-893, Oct. 1985.

[5] P.B. Johns, "A symmetric condensed node for the TLM method," *IEEE Trans. Microwave Theory Tech.*, vol. MTT-35, pp.370-377, April 1987.

[6] C. Christopoulos, *The Transmission-Line Modeling Method TLM.* New York, NY: IEEE Press, 1995.

Chapter 5

ADJOINT-VARIABLE METHOD FOR 3D-TLM WITH HYBRID SYMMETRICAL CONDENSED NODE

In the stub-loaded symmetrical condensed node [1], it is required that all the twelve link-lines have the same characteristic impedance. This impedance was selected to be equal to that of the free space. Any deficiency in the modeling of the permittivity and permeability of media other than air was compensated by introducing extra open and short circuit stubs at the node center [2]. The stub-loaded SCN was later utilized in TLM problems with variable meshes. The goal was reducing the required memory storage by defining finer mesh in areas with fast field variations, and coarser mesh for the rest of the structure. In the graded and variable mesh schemes, the maximum required time-step is determined by the ratio of the largest to the smallest grid dimensions. This constraint could impair the advantage of reducing the memory storage in large problems where large grid dimension ratios where used. Scaramuzza and Lowery [3] addressed this issue for the stub-loaded SCN by relaxing the required condition of having identical characteristic impedance on all twelve link-lines. The resulting node was referred to as the hybrid symmetrical condensed node (HSCN). Here, the required inductances are modeled at the node and only three extra open-circuit stubs are added to take into consideration the required capacitances. It turned out that the HSCN had also the advantage of having better dispersion properties in addition to memory storage saving. Alternative schemes were proposed in [4] where all the required capacitances are included at the node and the inductance deficiencies are compensated for by adding three extra short-circuit stubs for each polarization direction.

The aim of this chapter is to utilize the HSCN scheme in the adjoint sensitivity analysis for time domain TLM. A detailed discussion about the theoretical background of the HSCN is provided to gain deeper insight into the characteristics of the hybrid node, and to emphasis its advantages over the traditional SCN. The algorithm is then integrated with the adjoint variable method for sensitivity analysis of 3–D EM problems.

5.1 The Hybrid Symmetrical Condensed Node

In this section the characteristics of the hybrid symmetrical condensed node including the choice of the mesh parameters, the field calculations and excitations, and the scattering and connection properties are discussed in detail. In all derivations, the node numbering scheme proposed by Johns for symmetrical condensed node are adopted.

5.1.1 Mesh Parameters

Consider the node shown in Figure 5.1 which illustrates the discretization element of the medium in a single block of size (Δx, Δy, Δz). We define L_x, L_y and L_z to be

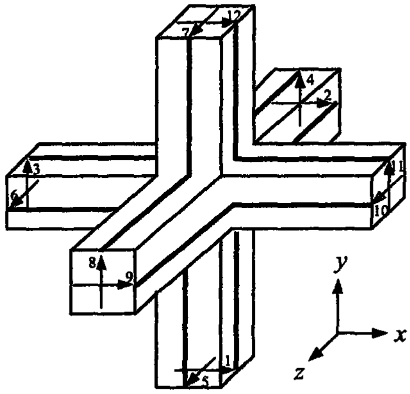

Figure 5.1: The unit cell of the standard symmetrical condensed node used as the basic building block of the hybrid node.

the total inductances modeled by the block in the x, y and z directions, respectively. Each of these inductances is associated with the corresponding magnetic field component at the node center. As an example, consider the total inductance with x-polarization, L_x. The link-lines contributing to the H_x component of the magnetic field are ports 4, 5, 7 and 8. In the hybrid scheme, it is assumed that all the link-lines contributing to a certain magnetic field have the same characteristic impedance; hence the transmission-lines associated with ports 4, 5, 7 and 8 have identical characteristic impedances, Z_x. Notice that although each of these ports contributes to the same magnetic field component, they have distinct polarizations: ports 4 and 8 are y-polarized while ports 5 and 7 have z-polarization. It seems to be reasonable to divide the total inductance in each direction into two portions according to the polarization of the terms. It follows that we have

$$\begin{aligned} L_x &= L'_{yz}\Delta y + L'_{zy}\Delta z = \mu\frac{\Delta y\Delta z}{\Delta x} \\ L_y &= L'_{xz}\Delta x + L'_{zx}\Delta z = \mu\frac{\Delta x\Delta z}{\Delta y} \\ L_z &= L'_{xy}\Delta x + L'_{yx}\Delta y = \mu\frac{\Delta x\Delta y}{\Delta z} \end{aligned} \tag{5.1}$$

where L'_{qp} represents the inductance per unit length of the link-line parallel to the q-axis with polarization p, and μ is the permeability of the medium at the node location[1]. It follows that three distinct values of characteristic impedances can be assigned to three sets of link-lines contributing to each of the three components of the magnetic field. Remember from the transmission-line theory that the characteristic impedance of each link-line is associated to the inductance and capacitance per unit length of the same line:

$$\begin{aligned}
\sqrt{\frac{L'_{yz}}{C'_{yz}}} &= \sqrt{\frac{L'_{zy}}{C'_{zy}}} \\
\sqrt{\frac{L'_{xz}}{C'_{xz}}} &= \sqrt{\frac{L'_{zx}}{C'_{zx}}} \\
\sqrt{\frac{L'_{xy}}{C'_{xy}}} &= \sqrt{\frac{L'_{yx}}{C'_{yx}}}
\end{aligned} \tag{5.2}$$

where C'_{qp} represents the capacitance per unit length of the link-line parallel to the q-axis with polarization p. Moreover, assume that each two pairs of the orthogonal link-lines contributing to a certain magnetic field to have the same total inductance. Hence

$$\begin{aligned}
L'_{yz}\Delta y &= L'_{zy}\Delta z \\
L'_{xz}\Delta x &= L'_{zx}\Delta z \\
L'_{xy}\Delta x &= L'_{yx}\Delta y.
\end{aligned} \tag{5.3}$$

From (5.1) and (5.3), it follows that the inductance per unit length of the link-lines can be expressed as

[1] All lumped elements and transmission line parameters with a prime superscript represent the corresponding *per unit length* parameter.

$$
\begin{aligned}
L'_{yz} &= \frac{\mu \Delta z}{2\Delta x} \quad , \quad L'_{zy} = \frac{\mu \Delta y}{2\Delta x} \\
L'_{xz} &= \frac{\mu \Delta z}{2\Delta y} \quad , \quad L'_{zx} = \frac{\mu \Delta x}{2\Delta y} \\
L'_{xy} &= \frac{\mu \Delta y}{2\Delta z} \quad , \quad L'_{yx} = \frac{\mu \Delta x}{2\Delta z}.
\end{aligned}
\tag{5.4}
$$

We denote the total capacitance modeled by the block in Figure 5.1 in the x, y and z directions by C_x, C_y and C_z, respectively. Each of these capacitances is composed of the distributed capacitances on the associated link-lines and the capacitance of the associated open-circuit stub at the node [2]:

$$
\begin{aligned}
C_x &= C'_{yx}\Delta y + C'_{zx}\Delta z + C^s_x = \varepsilon \frac{\Delta y \Delta z}{\Delta x} \\
C_y &= C'_{xy}\Delta x + C'_{zy}\Delta z + C^s_y = \varepsilon \frac{\Delta x \Delta z}{\Delta y} \\
C_z &= C'_{xz}\Delta x + C'_{yz}\Delta y + C^s_z = \varepsilon \frac{\Delta x \Delta y}{\Delta z}
\end{aligned}
\tag{5.5}
$$

where ε is the permittivity of the medium at the node location, and C^s_x, C^s_y and C^s_z are the capacitances of the added open-circuit stubs in the x, y and z directions, respectively. The capacitance per unit length of each transmission-line is related to the speed of propagation, u_{TL}, of a pulse on the line. From transmission-line theory it is well-know that the speed of propagation on a transmission-line of length Δl can be expressed in terms of the capacitance per unit length, C'_d, and the inductance per unit length, L'_d, of the line as

$$
u_{TL} = \frac{\Delta l}{\Delta t} = \frac{1}{\sqrt{C'_d L'_d}} \tag{5.6}
$$

where Δt indicates the propagation time on the transmission-line. From (5.3) and (5.6), it is clear that the capacitance per unit length of each link-line can be expressed as

$$
\begin{aligned}
C'_{yx} &= \frac{2\Delta z\Delta t^2}{\mu\Delta x\Delta y^2} \quad , \quad C'_{zx} = \frac{2\Delta y\Delta t^2}{\mu\Delta x\Delta z^2} \\
C'_{xy} &= \frac{2\Delta z\Delta t^2}{\mu\Delta y\Delta x^2} \quad , \quad C'_{zy} = \frac{2\Delta x\Delta t^2}{\mu\Delta y\Delta z^2} \\
C'_{xz} &= \frac{2\Delta y\Delta t^2}{\mu\Delta z\Delta x^2} \quad , \quad C'_{yz} = \frac{2\Delta x\Delta t^2}{\mu\Delta z\Delta y^2}.
\end{aligned}
\tag{5.7}
$$

Substituting (5.7) in (5.5) and solving for C_x^s, C_y^s and C_z^s, the capacitances of the open-circuit stubs given by:

$$
\begin{aligned}
C_x^s &= \frac{1}{\mu\Delta x\Delta y\Delta z}\left(\mu\varepsilon\Delta y^2\Delta z^2 - 2\Delta y^2\Delta t^2 - 2\Delta z^2\Delta t^2\right) \\
C_y^s &= \frac{1}{\mu\Delta x\Delta y\Delta z}\left(\mu\varepsilon\Delta x^2\Delta z^2 - 2\Delta x^2\Delta t^2 - 2\Delta z^2\Delta t^2\right) \\
C_z^s &= \frac{1}{\mu\Delta x\Delta y\Delta z}\left(\mu\varepsilon\Delta x^2\Delta y^2 - 2\Delta x^2\Delta t^2 - 2\Delta y^2\Delta t^2\right).
\end{aligned}
\tag{5.8}
$$

The expressions in (5.8) impose a set of three constraints on the maximum allowable simulation time step. For the stability of the algorithm, the capacitances of the open-circuit stubs should be non-negative. Solving (5.8) for Δt results

$$
\begin{aligned}
\Delta t &\le \frac{1}{c}\Delta y\Delta z\sqrt{\frac{\mu_r\varepsilon_r}{2\Delta y^2 + 2\Delta z^2}} \\
\Delta t &\le \frac{1}{c}\Delta x\Delta z\sqrt{\frac{\mu_r\varepsilon_r}{2\Delta x^2 + 2\Delta z^2}} \\
\Delta t &\le \frac{1}{c}\Delta x\Delta y\sqrt{\frac{\mu_r\varepsilon_r}{2\Delta x^2 + 2\Delta y^2}}
\end{aligned}
\tag{5.9}
$$

where $c = 1/\sqrt{\mu_0\varepsilon_0}$ is the propagation velocity in the free space. In order to meet the stability requirement of the algorithm, the set of inequalities given in (5.9) should be simultaneously satisfied at every node within the mesh. Depending on the block dimensions, different values for maximum allowable time step may obtain [5]. Using

$\Delta l = \min\{ \Delta x, \Delta y, \Delta z \}$, and recalling that for a uniform mesh with symmetrical condensed nodes of dimension Δl the time step is equal to $\Delta t = c/(2\Delta l)$. Consider the following cases:

case 1: $\Delta x = \Delta y = \Delta z = \Delta l$, the set of inequalities in (5.9) reduces to

$$\Delta t \le \frac{\Delta l}{2c}\sqrt{\mu_r \varepsilon_r}. \tag{5.10}$$

The lower limit of the maximum possible value of Δt is selected when $\mu_r = \varepsilon_r = 1$ which leads to

$$\Delta t_{\max} = \frac{\Delta l}{2c}. \tag{5.11}$$

This indicates that the maximum allowable time step for uniform HSCN and SCN are identical.

case 2: $\Delta x = \Delta y = \Delta l$, $\Delta z = \Delta m > \Delta l$. From the third inequality in (5.9)

$$\Delta t \le \frac{\Delta l}{2c}\sqrt{\mu_r \varepsilon_r}. \tag{5.12}$$

Similar to case 1, the lower limit of the maximum possible value of Δt is selected when $\mu_r = \varepsilon_r = 1$ which leads to

$$\Delta t_{\max} = \frac{\Delta l}{2c}. \tag{5.13}$$

case 3: $\Delta x = \Delta y = \Delta m > \Delta l$, $\Delta z = \Delta l$. In this case the maximum allowable time step is determined by either of the first two inequalities in (5.9) as

$$\Delta t_{\max} = \frac{1}{2c}\sqrt{\frac{2}{\left(\frac{1}{\Delta m^2}\right) + \left(\frac{1}{\Delta l^2}\right)}} > \frac{\Delta l}{2c}. \tag{5.14}$$

case 4: The most general cases arises when all dimensions are different. Assume $\Delta l = \Delta x < \Delta y < \Delta z$. In this case the third equation in (5.9) sets the upper limit on the simulation time step which is obtained as

$$\Delta t_{\max} = \frac{1}{2c}\sqrt{\frac{2}{\left(\frac{1}{\Delta l^2}\right)+\left(\frac{1}{\Delta y^2}\right)}} > \frac{\Delta l}{2c}. \tag{5.15}$$

From (5.14) and (5.15), it is observed that in the case that the dimension Δl is much smaller than the other two dimensions both expressions can then be approximated as

$$\Delta t_{\max} \approx \frac{\Delta l\sqrt{2}}{2c}. \tag{5.16}$$

The above discussion defines the valid range of maximum allowable time step for the hybrid symmetrical condensed node according to

$$\frac{\Delta l}{2c} \le \Delta t_{\max} < \frac{\Delta l\sqrt{2}}{2c}. \tag{5.17}$$

Once the simulation time step is determined, the rest of the mesh parameters can be derived. From (5.4) and (5.7) the normalized admittances of the link-lines are determined as follows [2]:

$$\begin{aligned}
Y_x &= \sqrt{\frac{C'_{yz}}{L'_{yz}}} = \frac{2c\Delta t\Delta x\sqrt{\mu_0\varepsilon_0}}{\mu_r\Delta y\Delta z} \to \hat{Y}_x = \frac{Y_x}{Y_0} = \frac{2c\Delta t\Delta x}{\mu_r\Delta y\Delta z}\\
Y_y &= \sqrt{\frac{C'_{xz}}{L'_{xz}}} = \frac{2c\Delta t\Delta y\sqrt{\mu_0\varepsilon_0}}{\mu_r\Delta x\Delta z} \to \hat{Y}_y = \frac{Y_y}{Y_0} = \frac{2c\Delta t\Delta y}{\mu_r\Delta x\Delta z}\\
Y_z &= \sqrt{\frac{C'_{xy}}{L'_{xy}}} = \frac{2c\Delta t\Delta z\sqrt{\mu_0\varepsilon_0}}{\mu_r\Delta x\Delta y} \to \hat{Y}_z = \frac{Y_z}{Y_0} = \frac{2c\Delta t\Delta z}{\mu_r\Delta x\Delta y}.
\end{aligned} \tag{5.18}$$

Similarly, the normalized admittances of the open-circuit stubs can be obtained from (5.8) as

$$\begin{aligned}
\hat{Y}_x^s &= \frac{2C_x^s}{\Delta t Y_0} = \frac{2\varepsilon_r}{c\Delta t}\frac{\Delta y \Delta z}{\Delta x} - \frac{4c\Delta t}{\mu_r \Delta x \Delta y \Delta z}\left(\Delta y^2 + \Delta z^2\right) \\
\hat{Y}_y^s &= \frac{2C_y^s}{\Delta t Y_0} = \frac{2\varepsilon_r}{c\Delta t}\frac{\Delta x \Delta z}{\Delta y} - \frac{4c\Delta t}{\mu_r \Delta x \Delta y \Delta z}\left(\Delta x^2 + \Delta z^2\right) \\
\hat{Y}_z^s &= \frac{2C_z^s}{\Delta t Y_0} = \frac{2\varepsilon_r}{c\Delta t}\frac{\Delta x \Delta y}{\Delta x} - \frac{4c\Delta t}{\mu_r \Delta x \Delta y \Delta z}\left(\Delta x^2 + \Delta y^2\right).
\end{aligned} \tag{5.19}$$

5.1.2 Field Calculations in HSCN

The derivations of the electromagnetic field components at the center of the HSCN are discussed here. We consider the E_x and H_x components of the electric and magnetic fields. The HSCN ports contributing to E_x are ports 1, 2, 9, 12 and the open-circuit stub 13. We also consider a loss stub in the x-direction to include any possible electric losses in this direction. Figure 5.2a illustrates the link-lines used for calculating the E_x component. The transmission-lines associated with ports 1 and 12 contribute to H_z and their link-lines are assumed to have identical characteristic admittance Y_z. Their total corresponding capacitance is therefore $C'_{yx} = Y_z \Delta t/2$. In the same manner, the characteristic admittance of the link-lines associated with ports 2 and 9 is Y_y with capacitance per unit length $C'_{zx} = Y_y \Delta t/2$. The capacitance associated with the open-circuit stub is equal to $C_x^s = Y_x^s \Delta t/2$. The total incident charge can thus be given as

$$\begin{aligned}
Q_{incident} &= C_{yx}\left(V_1^i + V_{12}^i\right) + C_{zx}\left(V_2^i + V_9^i\right) + C_x^s\left(V_{13}^i\right) \\
&= Y_z \frac{\Delta t}{2}\left(V_1^i + V_{12}^i\right) + Y_y \frac{\Delta t}{2}\left(V_2^i + V_9^i\right) + Y_z \frac{\Delta t}{2}\left(V_{13}^i\right).
\end{aligned} \tag{5.20}$$

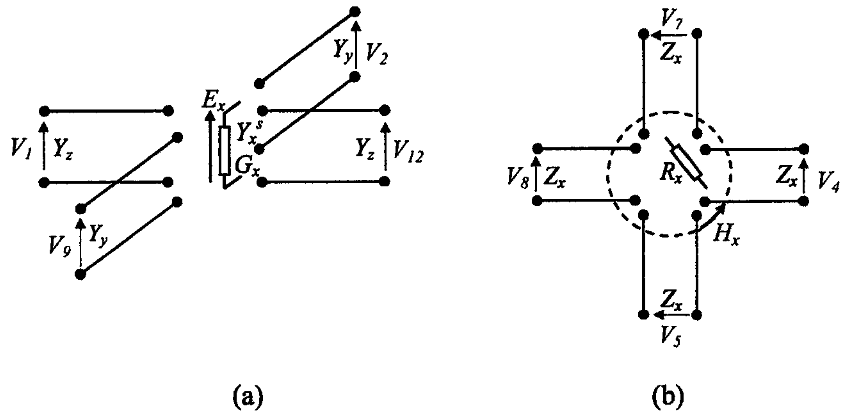

Figure 5.2: Hybrid node link-lines contributing to: (a) electric field component, E_x; (b) magnetic field component, H_x.

As no incident impulse appears on the loss stub, its effect on the calculations of the total incident charge was not considered. The conservation of electric charge implies that the total incident and reflected charges should be equal. It results that the total charge can be expressed as

$$Q_{total} = Q_{incident} + Q_{reflected} = 2Q_{incident}. \tag{5.21}$$

On the other hand the total capacitance in x direction is equal to

$$C_{total} = 2C_{yx} + 2C_{zx} + C_x^s + C_x^{loss} = Y_z\Delta t + Y_y\Delta t + Y_x^s\frac{\Delta t}{2} + G_x\frac{\Delta t}{2} \tag{5.22}$$

where the last term in (5.22) counts for the capacitance of the loss stub. Once the total electric charge and capacitance are known, after normalizing all admittances, the total voltage at the node can be evaluated as

$$V_x = \frac{2\hat{Y}_z\left(V_1^i + V_{12}^i\right) + 2\hat{Y}_y\left(V_2^i + V_9^i\right) + 2\hat{Y}_x^s\left(V_{13}^i\right)}{2\hat{Y}_z + 2\hat{Y}_y + \hat{Y}_x^s + \hat{G}_x}. \tag{5.23}$$

The electric field, E_x at the node center is thus obtained as

$$E_x = -\frac{V_x}{\Delta x} = -\frac{2\hat{Y}_z\left(V_1^i + V_{12}^i\right) + 2\hat{Y}_y\left(V_2^i + V_9^i\right) + 2\hat{Y}_x^s\left(V_{13}^i\right)}{\left(2\hat{Y}_z + 2\hat{Y}_y + \hat{Y}_x^s + \hat{G}_x\right)\Delta x}. \tag{5.24}$$

Now, consider Figure 5.2b to express the magnetic field component H_x in terms of the incident impulses. As can be seen, ports 4, 5, 7 and 8 contribute to I_x. Using the Thevenin's equivalent model of transmission-lines, the total voltage is

$$V = 2\left(V_4^i - V_5^i + V_7^i - V_8^i\right). \tag{5.25}$$

The total impedance is equal to $Z = 4Z_x + R_x$, where R_x counts for the magnetic loss in the x-direction. After normalizing the impedances, the current I_x is given as

$$I_x = \frac{2\left(V_4^i - V_5^i + V_7^i - V_8^i\right)}{Z_0\left(4\hat{Z}_x + \hat{R}_x\right)}. \tag{5.26}$$

Consequently, for the H_x component of the magnetic field

$$H_x = \frac{I_x}{\Delta x} = \frac{2\left(V_4^i - V_5^i + V_7^i - V_8^i\right)}{Z_0\left(4\hat{Z}_x + \hat{R}_x\right)}. \tag{5.27}$$

The derivation of the expressions in (5.24) and (5.27) can be easily extended to calculate the other field components in terms of the incident voltages:

$$\begin{aligned}
E_x &= -\frac{V_x}{\Delta x} = -\frac{2\hat{Y}_z\left(V_1^i + V_{12}^i\right) + 2\hat{Y}_y\left(V_2^i + V_9^i\right) + 2\hat{Y}_x^s\left(V_{13}^i\right)}{\left(2\hat{Y}_z + 2\hat{Y}_y + \hat{Y}_x^s + \hat{G}_x\right)\Delta x} \\
E_y &= -\frac{V_y}{\Delta y} = -\frac{2\hat{Y}_z\left(V_3^i + V_{11}^i\right) + 2\hat{Y}_x\left(V_4^i + V_8^i\right) + 2\hat{Y}_y^s\left(V_{14}^i\right)}{\left(2\hat{Y}_z + 2\hat{Y}_x + \hat{Y}_y^s + \hat{G}_y\right)\Delta y} \\
E_z &= -\frac{V_z}{\Delta z} = -\frac{2\hat{Y}_x\left(V_5^i + V_7^i\right) + 2\hat{Y}_y\left(V_6^i + V_{10}^i\right) + 2\hat{Y}_z^s\left(V_{15}^i\right)}{\left(2\hat{Y}_x + 2\hat{Y}_y + \hat{Y}_z^s + \hat{G}_z\right)\Delta z}.
\end{aligned} \tag{5.28a}$$

$$H_x = \frac{I_x}{\Delta x} = \frac{2\left(V_4^i - V_5^i + V_7^i - V_8^i\right)}{\Delta x Z_0\left(4\hat{Z}_x + \hat{R}_x\right)}$$

$$H_y = \frac{I_y}{\Delta y} = \frac{2\left(-V_2^i + V_6^i + V_9^i - V_{10}^i\right)}{\Delta y Z_0\left(4\hat{Z}_y + \hat{R}_y\right)} \tag{5.28b}$$

$$H_z = \frac{I_z}{\Delta z} = \frac{2\left(V_1^i - V_3^i + V_{11}^i - V_{12}^i\right)}{\Delta z Z_0\left(4\hat{Z}_z + \hat{R}_z\right)}.$$

5.1.3 Field Excitations in HSCN

Similar to exciting the SCN node, the excitation of a particular field in HSCN is carried out by applying particular incident voltages on the appropriate ports. For instance, to excite the $E_x^{excitation}$ at the center of the hybrid node, the following incident impulses can be injected on ports 1, 2, 9, 12 and 13

$$\begin{aligned} V_1^i = V_2^i = V_9^i = V_{12}^i &= -E_x^{excitation}\Delta x \\ V_{13}^i &= -E_x^{excitation}\Delta x - E_x^{excitation}\Delta x\frac{\hat{G}_x}{\hat{Y}_x^s}. \end{aligned} \tag{5.29}$$

Substituting with the above values in the first expression of (5.28a), one can easily verify that the suggested values of incident impulses excite an electric field at the center of the node with x-polarization and with magnitude $E_x^{excitation}$. Similarly, in order to excite the $H_x^{excitation}$, the associated incident impulses can take values as

$$\begin{aligned} V_4^i = V_7^i &= \Delta x Z_0\left(\frac{4\hat{Z}_x + \hat{R}_x}{8}\right)H_x^{excitation} \\ V_5^i = V_8^i &= -\Delta x Z_0\left(\frac{4\hat{Z}_x + \hat{R}_x}{8}\right)H_x^{excitation}. \end{aligned} \tag{5.30}$$

Similar expression can be obtained to excite other field components. However, note that the suggested values are not the only possible values, and other mappings could be considered to map incident voltages into field components.

5.1.4 Scattering Properties of HSCN

The scattering matrix of the hybrid node can be obtained based on the unitary principal [3] or from the fundamental principals of conservation of charge, conservation of magnetic flux, and the continuity of the electric and magnetic fields. Here, the form of the scattering matrix for the general case with the electric and magnetic losses and the terms for the current sources are presented. A comprehensive derivation can be found in [2].

R_l	G_s	Y_l Y_l Y_s	y z x 1	z y x 2	x z y 3	z x y 4	y x z 5	x y z 6	y x z 7	z x y 8	z y x 9	x y z 10	x z y 11	y z x 12	x 13	y 14	z 15	x 16	y 17	z 18
z	x	1	a	b	d						b		-d	c	g			k		
y	x	2	b	a				d			c	-d		b	g			k		
z	y	3	d		a	b				b			c	-d		g			k	
x	y	4			b	a	d		-d	c			b			g			k	
x	z	5				d	a	b	c	-d		b					g			k
y	z	6		d			b	a	b		-d	c					g			k
x	z	7				-d	c	b	a	d		b					g			k
x	y	8			b	c	-d		d	a			b			g			k	
y	x	9	b	c				-d			a	d		b	g			k		
y	z	10		-d			b	c	b		d	a					g			k
z	y	11	-d		c	b				b			a	d		g			k	
z	x	12	c	b	-d						b		d	a	g			k		
	x	13	b	b							b			b	h			k		
	y	14			b	b				b			b			h			k	
	z	15					b	b	b			b					h			k

where the scattering coefficients are given by:

$$
\begin{aligned}
a &= -\frac{\hat{Y}_s + \hat{G}_s + 2(\hat{Y}_l - \hat{Y}_t)}{2\,[\hat{Y}_s + \hat{G}_s + 2(\hat{Y}_l + \hat{Y}_t)]} + \frac{\hat{R}_t \hat{Y}_t}{2(\hat{R}_t \hat{Y}_t + 4)} \\
b &= \frac{2\hat{Y}_t}{\hat{Y}_s + \hat{G}_s + 2(\hat{Y}_l + \hat{Y}_t)} \\
c &= -\frac{\hat{Y}_s + \hat{G}_s + 2(\hat{Y}_l - \hat{Y}_t)}{2\,[\hat{Y}_s + \hat{G}_s + 2(\hat{Y}_l + \hat{Y}_t)]} - \frac{\hat{R}_t \hat{Y}_t}{2(\hat{R}_t \hat{Y}_t + 4)} \\
d &= \frac{2}{\hat{R}_t \hat{Y}_t + 4} \\
g &= b\frac{\hat{Y}_s}{\hat{Y}_t} \\
h &= \frac{\hat{Y}_s - \hat{G}_s - 2(\hat{Y}_l + \hat{Y}_t)}{\hat{Y}_s + \hat{G}_s + 2(\hat{Y}_l + \hat{Y}_t)} \\
k &= \frac{1}{\hat{Y}_s + \hat{G}_s + 2(\hat{Y}_l + \hat{Y}_t)}.
\end{aligned}
\tag{5.31}
$$

The values of the conductance and the resistance associated with the electric and magnetic losses are obtained as

$$
\begin{aligned}
\hat{G}_x &= \sigma_{ex}\frac{\Delta y \Delta z}{\Delta x Y_0} \quad , \quad \hat{G}_y = \sigma_{ey}\frac{\Delta x \Delta z}{\Delta y Y_0} \quad , \quad \hat{G}_z = \sigma_{ez}\frac{\Delta x \Delta y}{\Delta z Y_0} \\
\hat{R}_x &= \sigma_{mx}\frac{\Delta y \Delta z}{\Delta x Z_0} \quad , \quad \hat{R}_y = \sigma_{my}\frac{\Delta x \Delta z}{\Delta y Z_0} \quad , \quad \hat{R}_z = \sigma_{mz}\frac{\Delta x \Delta y}{\Delta z Z_0}.
\end{aligned}
\tag{5.32}
$$

Here, σ_{eq} and σ_{mq} are the electric and magnetic conductivities in the q -direction, respectively.

5.1.5 Connection Properties of HSCN

Unlike the connection procedure in the symmetrical condensed node where the reflected impulses at each time step are simply exchanged between the neighboring nodes, special consideration should be taken into account when implementing the connection

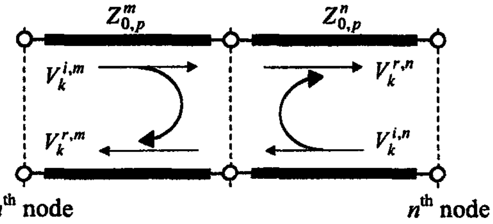

Figure 5.3: The k^{th} time step reflected and transmitted impulses at the interface of two link-lines with p-polarity connecting the m^{th} and n^{th} hybrid symmetrical condensed nodes.

procedure for the hybrid node. Due to impedance mismatch between the link-lines of neighboring nodes, reflections may happen at the midpoint of two adjacent nodes. Also the link-lines associated with each polarization at the arms of the nodes may experience different impedances, hence they should be considered separately. Figure 5.3 illustrates the case where the link-lines with p-polarization of the m^{th} and n^{th} adjacent nodes are connected to each other and have characteristic impedances $Z_{0,p}^{m}$ and $Z_{0,p}^{n}$, respectively. From transmission-line theory the incident impulses at the $(k+1)^{th}$ time step is [6]

$$\begin{aligned} V_{k+1}^{i,m} &= \frac{1-n}{1+n} V_k^{i,m} + \frac{2n}{1+n} V_k^{i,n} \\ V_{k+1}^{i,n} &= \frac{2}{n+1} V_k^{i,m} + \frac{n-1}{n+1} V_k^{i,n}. \end{aligned} \tag{5.33}$$

where $n = Z_{0,p}^{m} / Z_{0,p}^{n}$. This inter-nodal reflection should be incorporated in the connection step.

The previous discussion provides the theoretical background required for formulating the TLM with HSCN. Assume the total number of the associated TLM links are denoted as N_L. We define the system scattering matrix $\boldsymbol{S} \in \Re^{N_L \times N_L}$ as a block diagonal matrix whose p^{th} block, $\boldsymbol{S}^p$ is the hybrid nodal scattering matrix of the p^{th} node. We also consider the symmetrical system connection matrix $\boldsymbol{C} \in \Re^{N_L \times N_L}$ which realizes the connection step of each node within the mesh. The vectors ${}_k\boldsymbol{V}^i \in \Re^{N_L}$, ${}_k\boldsymbol{V}^r \in \Re^{N_L}$ and ${}_k\boldsymbol{V}^s \in \Re^{N_L}$ are taken as the vectors of incident, reflected and excitation impulses of all nodes at the k^{th} time step. A single TLM simulation at the k^{th} iteration can then be expressed as

$$ {}_{k+1}\boldsymbol{V}^i = \boldsymbol{CS}\,{}_k\boldsymbol{V}^i + {}_k\boldsymbol{V}^s + \sum_{k'=0}^{k} \boldsymbol{J}(k-k')\,{}_k\boldsymbol{V}^r \quad , \quad \boldsymbol{V}^i(0) = \boldsymbol{0} \tag{5.33} $$

where the matrix $\boldsymbol{J}(k)$ is the k^{th} time layer of the three-dimensional Johns matrix. Note that a Johns' matrix generated for a TLM problem with SCN can be employed in the hybrid scheme and vice versa.

5.2 The Adjoint-Variable Method for HSCN

The adjoint-sensitivity analysis using the hybrid symmetrical condensed node is similar to the case of the SCN, discussed in chapter 3. The objective function has the form:

$$ F = \int_0^{T_{\max}} \Psi(\boldsymbol{x},\boldsymbol{V})\, dt \tag{5.34} $$

where $T_{\max}$ is the simulation time, and the real valued function $\Psi(\boldsymbol{x},\boldsymbol{V})$ is the objective function kernel. Using the AVM, the derivatives of the objective function with respect to all designable parameters can be efficiently estimated as [7]

$$ \frac{\partial F}{\partial x_i} \approx \frac{\partial^e F}{\partial x_i} - \Delta t \sum_{k=0}^{N_t} {}_k\boldsymbol{\lambda}^T \frac{\Delta \boldsymbol{A}_i}{\Delta x_i}\,{}_k\boldsymbol{V}^i = \frac{\partial^e F}{\partial x_i} - \Delta t \sum_{k=0}^{N_t} {}_k\boldsymbol{\lambda}^T\,{}_k\boldsymbol{\eta}^i \tag{5.35} $$

where the first term $\partial^e F/\partial x_i$ corresponds to the explicit dependency of the function F on the i^{th} designable parameter. The constants Δt and N_t denote the time step and the total number of simulation time steps, respectively. The vector ${}_k\boldsymbol{\eta}^i$ reflects the associated changes in the system matrix $\boldsymbol{A} = (\boldsymbol{C}(\boldsymbol{x})\boldsymbol{S}(\boldsymbol{x}) - \boldsymbol{I})/\Delta t$ due to a perturbation Δx_i and is generally given by:

$$ {}_k\boldsymbol{\eta}^i = \frac{1}{\Delta x_i \Delta t}\left[(\Delta \boldsymbol{C}_i)\boldsymbol{S} + \boldsymbol{C}(\Delta \boldsymbol{S}_i)\right]_k \boldsymbol{V}^i. \tag{5.36} $$

Here, $\Delta \boldsymbol{C}_i$ and $\Delta \boldsymbol{S}_i$ correspond to changes of the system connection and scattering matrices of the hybrid scheme associated with a one cell-size perturbation of x_i. A comparison between the dimensionality of the vector ${}_k\boldsymbol{\eta}^i$ in the SCN and HSCN indicates that storage saving can be achieved when the structure undergoes a perturbation due to dielectric discontinuities. For the case of the SCN, the dimensionality of the ${}_k\boldsymbol{\eta}^i$ for a dielectric perturbation is $18[(n_2 - n_1 + 1)\,(p_2 - p_1 + 1)]$ while it is $15[(n_2 - n_1 + 1)\,(p_2 - p_1 + 1)]$ (n_i and p_i, i=1, 2 are the coordinate intervals of the affected nodes). This results in a storage saving of approximately 17%. However, in the case of metallic discontinuities the dimensionality of ${}_k\boldsymbol{\eta}^i$ for both SCN and HSCN is $2[(n_2 - n_1 + 1)\,(p_2 - p_1 + 1) + 2(p_2 - p_1 + 1) + 2(n_2 - n_1 + 1)]$. This indicates that the hybrid scheme does not have any priority over the traditional SCN in storing the elements of ${}_k\boldsymbol{\eta}^i$.

Similar to the adjoint simulation of the SCN, the vector of the adjoint impulses, ${}_k\boldsymbol{\lambda}$ in (5.35) is obtained from the backward TLM simulation expressed as [10]

$$ {}_{k-1}\boldsymbol{\lambda} = \boldsymbol{S}^T(\boldsymbol{x})\left[\boldsymbol{C}^T(\boldsymbol{x})\,{}_k\boldsymbol{\lambda} + \sum_{k'=k}^{N_t} \boldsymbol{J}^T(k'-k)\,{}_{k'}\boldsymbol{\lambda}\right] - {}_k\boldsymbol{\lambda}^s \;,\; \boldsymbol{\lambda}(T_s) = \boldsymbol{0}. \tag{5.37} $$

5.3 Examples

We illustrate the AVM-HSCN method by estimating the sensitivities of the S-parameters of waveguide structure with respect to physical discontinuities.

5.3.1 Six-Section *H*-Plane Waveguide Filter

The geometry of the six-section H-plane waveguide filter [11] is shown in Figure 5.4. The AVM approach is used to estimate the sensitivities of the reflection $\tilde{S}_{11}$ with respect to the physical dimensions of the metallic discontinuities. The structure is uniformly discretized with hybrid cells of size $\Delta l = 0.6223$ mm. The problem can be reduced to a 2-D TLM problem by simulating a single layer of 3D hybrid nodes in the xz-plane bounded at the top and bottom with perfectly conducting planes. The filter is excited with a Gaussian modulated sinusoid centered at $f_c = 7.5$ GHz with the spectrum range from 5.0 GHz to 10.0 GHz, and with TE_{10} mode spatial profile. Symmetry is employed to simulate only half of the structure. The filter is terminated at the input and output ports by modal Johns matrix boundaries with $N_t = 6000$ time steps. The vector of designable parameters is taken as $\boldsymbol{x} = [\,W_1 \;\; W_2 \;\; W_3 \;\; W_4]^T$. Figures 5.5–5.8 illustrate the sensitivities of the real and imaginary parts of $\tilde{S}_{11}$ obtained using the AVM and the central finite differences over a frequency sweep in the range 5.0 GHz – 10.0 GHz with an interval of 25.0 MHz. The results indicate good match between the two approaches. While the central differences provide the sensitivities using 9 TLM simulations, the AVM extracts the same information using only two simulations.

a	17.4244
b	15.7988
δ	0.6223
W_1	13.0683
W_2	11.8237
W_3	11.2014
W_4	11.2014
L_1	16.1798
L_2	16.1798
L_3	16.8021
all dimensions in mm	

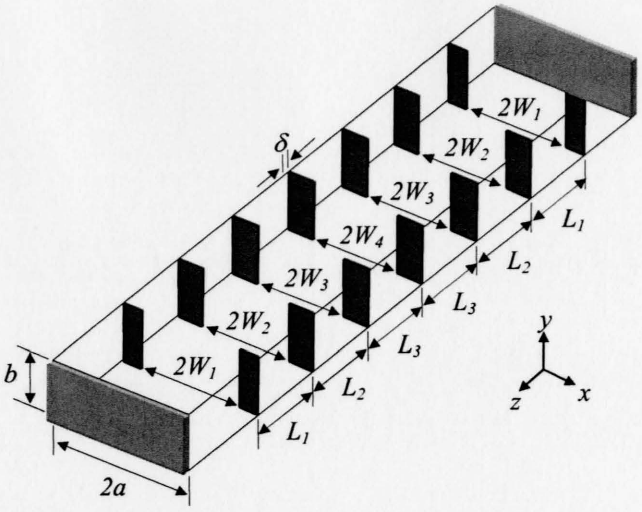

(a)

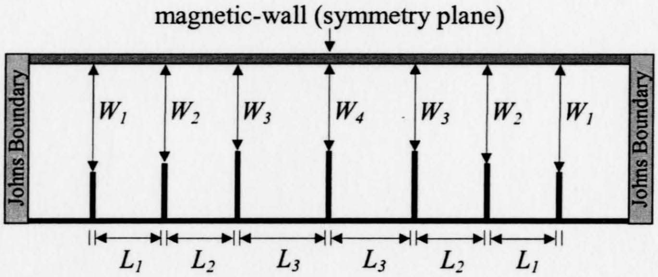

(b)

Figure 5.4: (a) The 3D view of the six section H-plane filter. (b) The cross section of the filter in the xz-plane with employed symmetry and Johns dispersive absorbing boundaries at the input and output ports.

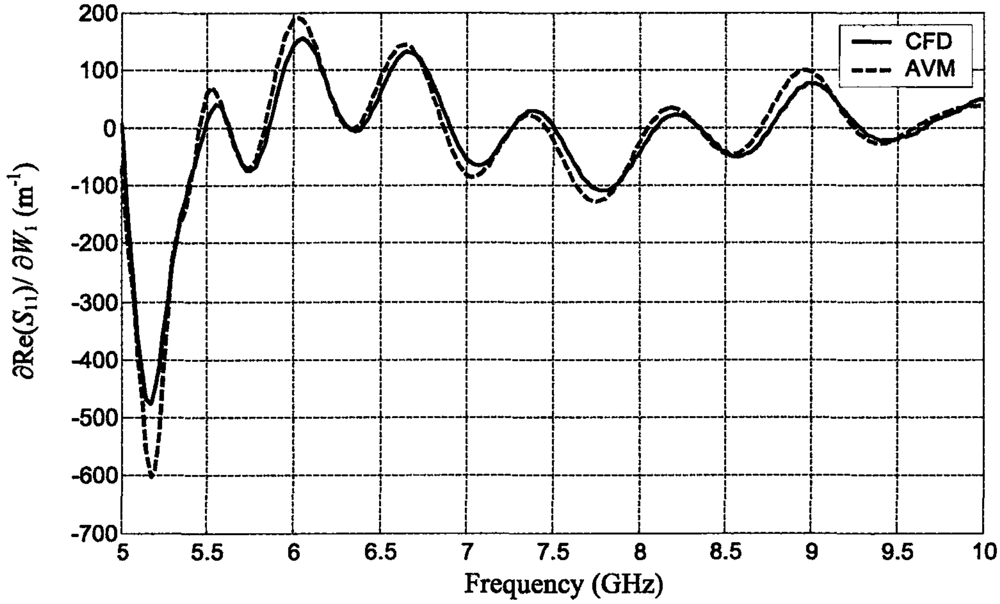

(a)

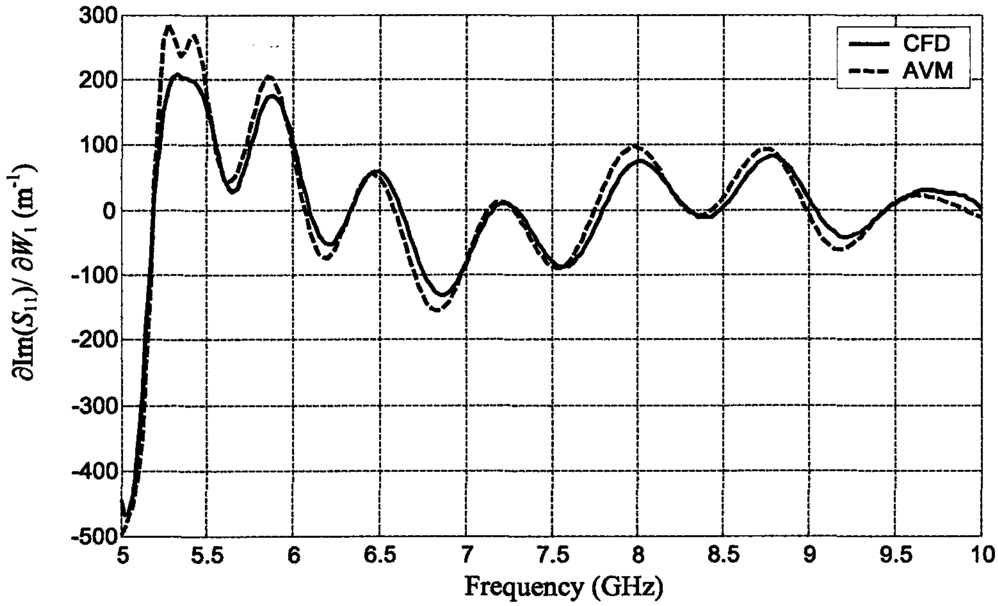

(b)

Figure 5.5: The sensitivities of the real and imaginary parts of $\widetilde{S}_{11}$ with respect to W_1.

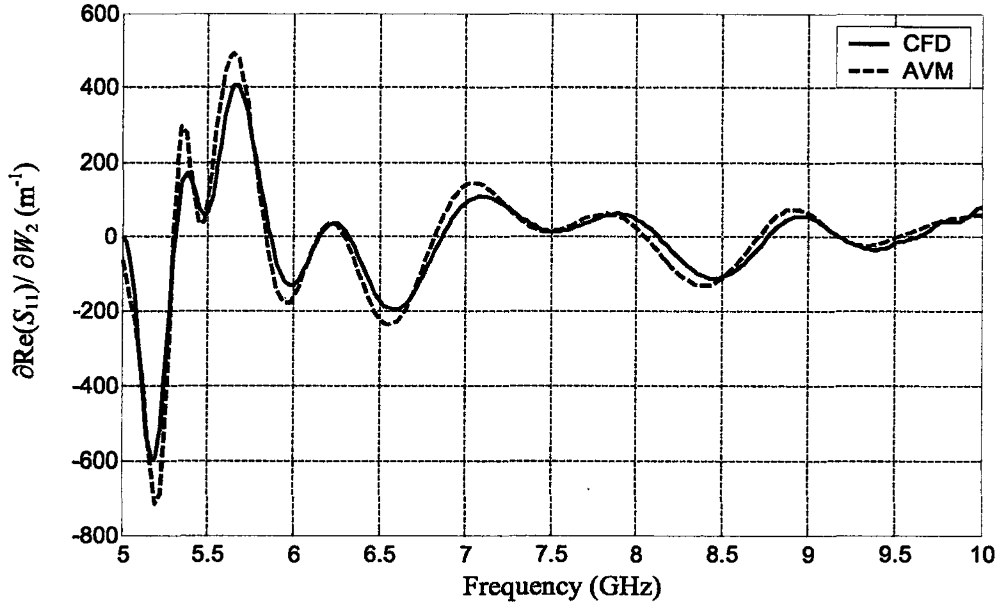

(a)

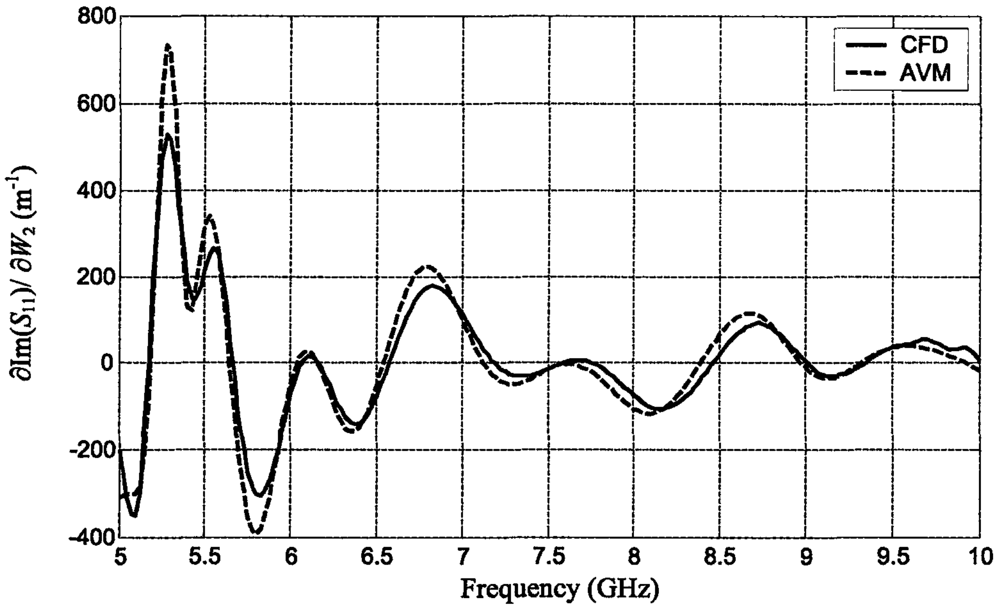

(b)

Figure 5.6: The sensitivities of the real and imaginary parts of $\tilde{S}_{11}$ with respect to W_2.

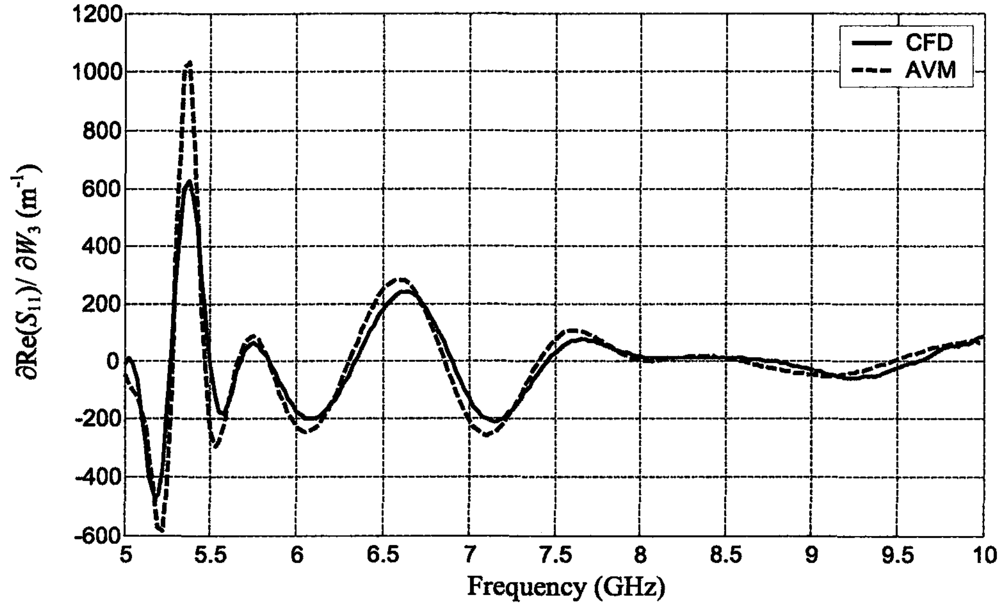

(a)

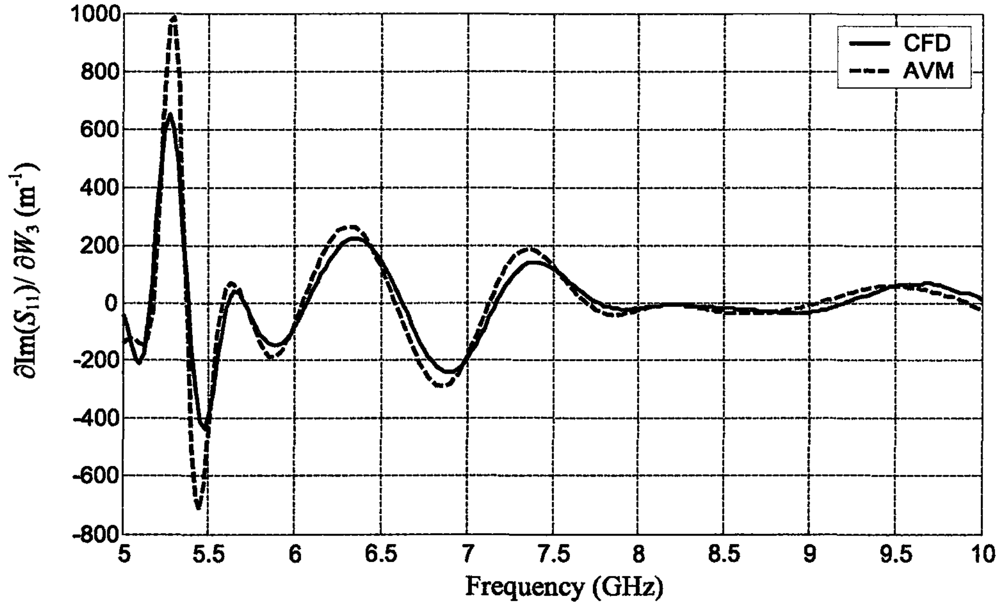

(b)

Figure 5.7: The sensitivities of the real and imaginary parts of $\widetilde{S}_{11}$ with respect to W_3.

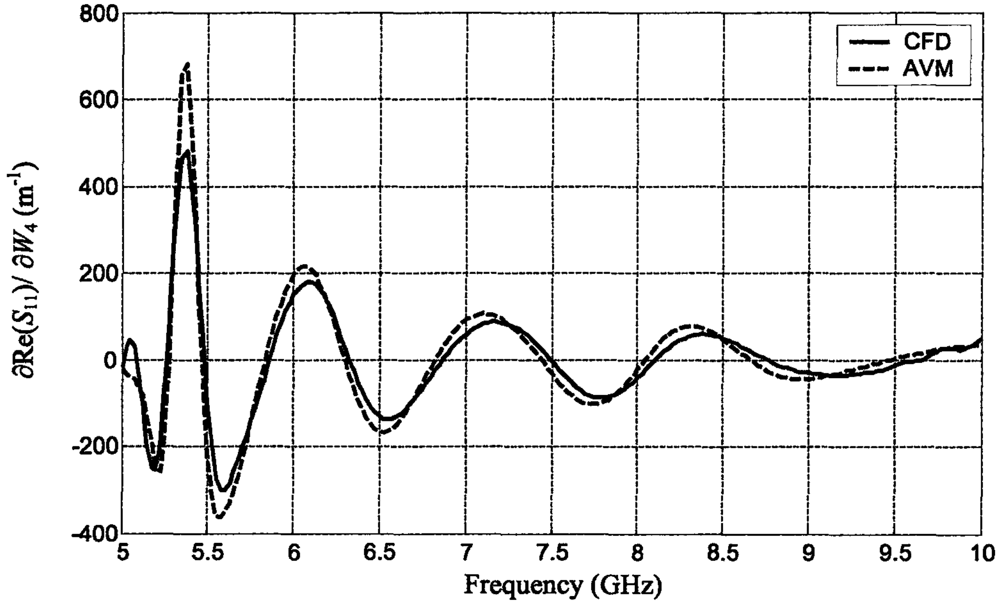

(a)

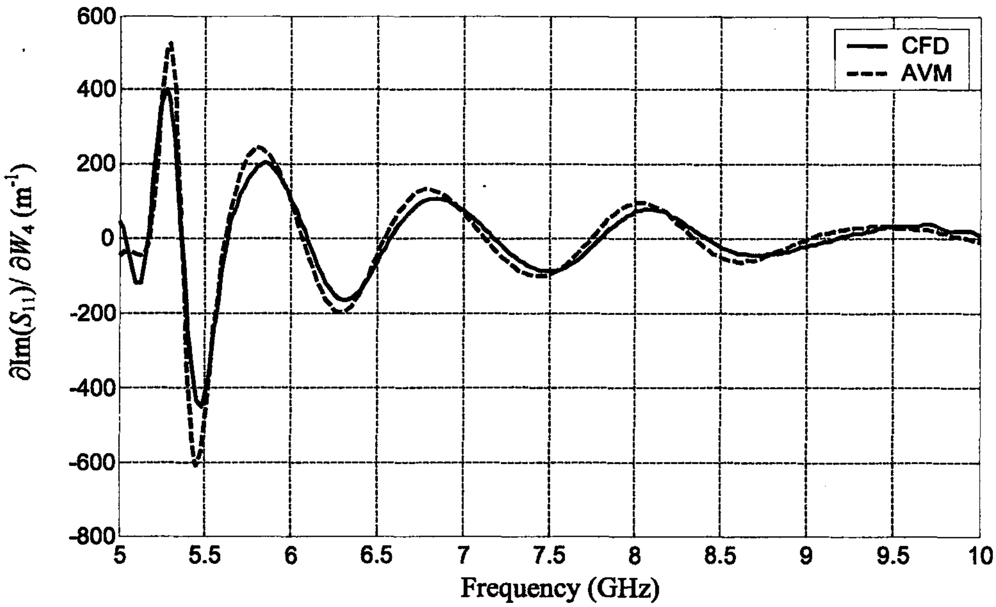

(b)

Figure 5.8: The sensitivities of the real and imaginary parts of $\tilde{S}_{11}$ with respect to W_4.

REFERENCES

[1] P.B. Johns, "A symmetrical condensed node for the TLM method," *IEEE Trans. Microwave Theory Tech.*, vol. MTT-35, no. 4, pp.370-377, April 1987.

[2] C. Christopoulos, *The Transmission-Line Modeling (TLM) Method.* New York, NY: IEEE Press, 1995.

[3] R.A. Scaramuzza and A. J. Lowery. "Hybrid symmetrical condensed node for the TLM method," *Electronics Letters,* vol. 26, no. 23, pp. 1947-1949, November 1990.

[4] P. Berrini and K. Wu, "A pair of hybrid symmetrical condensed TLM nodes," *IEEE Microwave and Guided Wave Letters,* vol. 4, no. 7, pp. 370-377, April 1987.

[5] V. Trenkic, C. Christopoulos, and T.M. Benson, "On the time step in hybrid symmetrical condensed TLM nodes," *IEEE Trans. Microwave Theory Tech.*, vol. 43, no. 9, pp. 2172-2174, September 1995.

[6] W. J. R. Hoefer and P. Sautier, "Characteristics of the general rectangular 2D-TLM network," *Int. J. of Numerical Modelling: Electronic Networks, Devices and Fields*, vol. 7, no. 2, pp. 127-139, March/April 1994.

[7] M.H. Bakr and N.K. Nikolova, "An adjoint variable method for time domain TLM with fixed structured grids," *IEEE Trans. Microwave Theory Tech.*, vol. 52, no. 2, pp. 554-559, February 2004.

[8] P.A.W. Basl, M.H. Bakr, and N.K. Nikolova, "An AVM technique for 3D TLM with symmetric condensed nodes," *IEEE Microwave and Wireless Components Letters*, vol. 15, no. 10, pp. 618-620, October 2005.

[9] M.H. Bakr and N.K. Nikolova, "Efficient estimation of adjoint-variable *S*-parameter sensitivities with time domain TLM," *Int. J. of Numerical Modelling: Electronic Networks, Devices and Fields*, vol. 18, no. 2, pp. 171-187, March 2005.

[10] M.H. Bakr and N.K. Nikolova, "An adjoint variable method for time domain TLM with wideband Johns matrix boundaries," *IEEE Trans. Microwave Theory Tech.*, vol. 52, no. 2, pp. 678-685, February 2004.

[11] G. Matthaei, L. Young, and E.M.T. Jones, *Microwave Filters, Impedance-Matching Networks, and Coupling Structures.* Norwood, MA: Artech House, 1980.

[12] J.L. Herring, "Developments in the Transmission-Line Modelling Method for Electromagnetic Compatibility Studies," Ph.D. Thesis, University of Nottingham, UK, 1993.

Chapter 6

CONCLUSIONS

This thesis has presented recent developments in the sensitivity analysis of high-frequency structures in time-domain transmission-line modeling (TLM) technique using the novel adjoint variable method (AVM) approach. Two major contributions have been achieved as the outcome of the research. The first contribution is a novel formulation for expressing the original and the adjoint systems. In general, the adjoint system for a TLM problem is expressed by a backward-running simulation where the order of the scattering and connection matrices is reversed. The system scattering and the connection matrices are also the transpose of those in the original system. This implies using two different simulators for implementing the AVM technique. Consequently, restrictions are imposed in using commercial solvers with the AVM approach. In Chapter 4, a new formulation is presented which casts the original and adjoint systems into a mathematically identical form with the only difference in the excitation. This is achieved by decomposing the systems scattering matrix, which in general is asymmetric, into a new symmetric matrix and a block diagonal transforming matrix. The new approach is shown to provide comparable results with the accurate central-finite difference approximations. The proposed formulation can be considered as a substitute to the current TLM engines to make them compatible with the AVM algorithm.

The second major achievement is generalization of the AVM for 3-D TLM problems with more advance discretization elements. In all previous AVM-related publications, the stub-loaded symmetrical condensed node was used as the discretization node. In Chapter 5, this is expanded to include the hybrid symmetrical condensed (HSCN) node, where better dispersion properties, longer simulation time step and smaller memory storage are feasible. A detailed discussion about the underlying theory of the hybrid node is discussed to emphasize its advantages over the stub-loaded SCN.

Our recent developments are illustrated using several waveguide examples. In all examples, the sensitivities of time-domain objective functions as well as the scattering parameter sensitivities are estimated and compared to those obtained using the more accurate central finite difference approximations. Very good match is obtained between both approaches.